MARMARA UNIVERSITY

INSTITUTE FOR GRADUATE STUDIES IN

PURE AND APPLIED SCIENCES

ELECTROWEAK PHASE TRANSITIONS IN THE EARLY UNIVERSE

SİNAN GÜYER

Ph.D. THESIS

Department of Physics

Thesis Supervisor

Prof. Dr. MİTHAT KAYA

ISTANBUL, 2023

MARMARA UNIVERSITY

INSTITUTE FOR GRADUATE STUDIES IN

PURE AND APPLIED SCIENCES

ELECTROWEAK PHASE TRANSITIONS IN THE EARLY UNIVERSE

SİNAN GÜYER

721216001

Ph.D. THESIS

Department of Physics

Thesis Supervisor

Prof. Dr. MİTHAT KAYA

ISTANBUL, 2023

ACKNOWLEDGEMENT

I am deeply grateful for the unwavering support and encouragement from my family throughout this journey. My heartfelt thanks go to Serap and Feridun Güyer, whose enduring belief in my capabilities has been a constant source of motivation. Additionally, I extend my gratitude to my partner, Ayşe Melike Bilgin, for her unyielding support and understanding during the demanding phases of this endeavor.

A significant debt of gratitude is owed to my esteemed advisor, Prof. Dr. Mithat Kaya. His insightful guidance, invaluable suggestions, and continuous mentorship have played an instrumental role in shaping both my research work and academic trajectory. I am indebted to him for his unwavering belief in my potential and for fostering an environment of intellectual growth.

My appreciation extends to Prof. Dr. Kari Rummukainen, whose contributions to my work have been invaluable. I am especially grateful for the consistent presence of Oliver GOULD, whose unwavering support during times of struggle has provided me with the strength to persevere through challenging moments. Oliver's guidance and assistance have been indispensable, transforming difficult situations into opportunities for growth and learning.

I wish to express my sincere gratitude to Prof. Dr. Özgür DELİCE for his substantial academic contributions that have enriched the quality of my research. Furthermore, I extend my thanks to Dr. Hüseyin BAHTİYAR for his enduring friendship and valuable insights, which have greatly influenced both my academic and personal life. A special mention goes to Doç. Dr. Bora IŞILDAK for involving me in the TÜBİTAK 1001 project, an experience that has significantly broadened my horizons.

The camaraderie and shared experiences with my friends at the university, Haluk SEÇUK ,Dr. Okan ATAKİŞİ, and Dr. Saba Arife BOZPOLAT have been a constant source of joy and support. Their presence has lightened the load during challenging times and magnified the triumphs we've celebrated together.

I am immensely grateful to Dr. Nurhan Hande SEVGİ and Havva SERİM for their invaluable contributions that have significantly enhanced the quality and impact of my work. Their dedication, guidance, and unwavering support have been instrumental in shaping the development of my project. I am truly fortunate to have had the opportunity to benefit from their expertise and insight. Their willingness to share their knowledge and provide assistance has been a driving force behind the positive outcomes achieved in this endeavor. My heartfelt thanks go out to both Dr. Nurhan Hande SEVGİ and Dr. Havva SERİM for their outstanding and meaningful support. In a different chapter of my life, I express gratitude to my childhood friends, Dr. Semih DANIŞ and Med. Dr. Zafer BİNAL, for their enduring friendship and encouragement. Their unwavering belief in my potential has been a driving force in my pursuit of academic excellence.

Lastly, I extend my gratitude to the Science and Technology Facilities Council (STFC) for their support through the Consolidated grant ST/T000732/1. I also acknowledge the support of the Academy of Finland, with grants 320123, 319066, and 345070, which have significantly contributed to the advancement of my research. Generous computational resources provided by CSC – IT Center for Science, Finland, have been crucial in the realization of my work.

In closing, I wish to convey my heartfelt appreciation to each individual and institution mentioned here. Their collective contributions have shaped this research endeavor in ways beyond measure, and I am profoundly thankful for their unwavering belief in my potential and their enduring support throughout this journey.

TABLE OF CONTENTS

ACKNOWLEDGEMENTS i
TABLE OF CONTENTS iv
ÖZET v
ABSTRACT vi
CLAIM FOR ORIGINALITY vii
ABBREVIATIONS x
SYMBOLS xii
LIST OF FIGURES xiv
LIST OF TABLES xv
1. INTRODUCTION 1
1.1. Early Universe 4
1.2. The Electroweak Phase Transitions 9
1.2.1. First-Order Electroweak Phase Transition 11
1.2.2. Lattice Gauge Theory 13
2. 3D LATTICE MONTE-CARLO SIMULATIONS 15
2.1. Lattice Monte Carlo Method 15
2.2. Dimensional Reduction 18
2.3. Lattice Monte Carlo Simulations for 3D 19
3. EQUILIBRIUM QUANTITIES 25
4. Critical Temperature 27
5. LATENT HEAT 44
6. SURFACE TENSION 48
7. SUMMARY OF EQUILIBRIUM RESULTS 55
8. BUBBLE NUCLEATION 56
9. NUCLEATION RATE 61
10. VISUALISING BUBBLE NUCLEATION 80

11. COSMOLOGICAL EVALUATION 87
12. RESULTS AND DISCUSSION 92
REFERENCES 98
13. APPENDIX 107
13.1. Continuum Extrapolations 107
13.2. Perturbative Results 111
13.3. Lattice Volumes 116

ÖZET

ERKEN EVRENDE ELEKTRO-ZAYIF FAZ GEÇİŞLERİ

Bu çalışmada, SU(2) Higgs 3D Etkin Alan Teorisi'nin (Effective Field Theory - EFT) kapsamlı örgü Monte-Carlo simülasyonlarını ve süreklilik ekstrapolasyonlarını sunmaktadır. İncelenen model, Standart Model'in elektrozayıf sektörünün yüksek sıcaklık termodinamiğinin yanı sıra çeşitli Standart Model Ötesi (Beyond Standard Model - BSM) uzantılarını da tanımlamaktadır. Odak noktası, kütleçekim dalgası deneyleri ve elektrozayıf baryogenez ile ilgili olan EFT'de birinci dereceden faz geçişlerinin olduğu parametre uzayı bölgesidir.

Bu çalışmanın sonuçları önceki çalışmaların ötesine geçmekte ve elektrozayıf sektörün uzantılarında birinci dereceden faz geçişlerinin özelliklerini nicel olarak belirlemek için değerli bir kaynak sağlamaktadır. Verilen bir 4D model için 3D EFT'nin etkin çiftlenimlerini hesaplayarak, 4D modelin pertürbatif olmayan termodinamiği kolayca elde edilebilir. Ek olarak, sonuçlar plazmadaki ses dalgaları tarafından üretilen yerçekimi dalga spektrumunun tahmin edilmesini sağlar.

Bu bulgular, $O(gT)$ veya daha yüksek kütleli yeni serbestlik derecelerinin birinci dereceden Higgs simetri kırıma geçişine neden olduğu BSM senaryolarına uygulanabilir. Daha hafif BSM serbestlik derecelerini veya geçişe doğrudan katılımı içeren senaryolar için, diğer 3D EFT'lerde farklı örgü Monte-Carlo simülasyonları gereklidir.

Higgs modelinin SU(2) parametre uzayı araştırması, kritik kütle ve atlama gibi anahtar termodinamik niceliklerin fonksiyonel formları hakkında bilgi sağlar.

ABSTRACT

ELECTROWEAK PHASE TRANSITION IN THE EARLY UNIVERSE

This study presents comprehensive lattice Monte-Carlo simulations and extrapolations to the continuum of the three-dimensional Effective Field Theory (EFT) based on the SU(2) Higgs model. The model under investigation encompasses the thermodynamics at high temperatures within the electroweak sector of the Standard Model and various Beyond the Standard Model (BSM) extensions. The focus is on the parameter space region with first-order phase transitions (PTs), which is relevant for gravitational wave experiments and electroweak baryogenesis.

The findings of this research go beyond previous studies and offer a valuable resource for quantitatively determining the properties associated with first-order PTs in extensions of the electroweak sector. By computing the effective couplings within the three-dimensional EFT for a given four-dimensional model, one can readily obtain the nonperturbative thermodynamics.These results enable the prediction of the gravitational wave spectrum, utilizing the sound waves within the plasma, making it possible to estimate.

These findings are applicable to scenarios with new degrees of freedom that lead to first-order Higgs symmetry-breaking transitions with masses on the scale of $O(gT)$ or higher. In situations where there are fewer degrees of freedom at play or a more direct engagement in the transition, the need arises for various lattice Monte-Carlo simulations within alternate 3D EFT.

Examining the parameter range of the Higgs model within the SU(2) framework yields valuable insights into key thermodynamic measures, like the critical mass and the abrupt shift in the Higgs condensate.

CLAIM FOR ORIGINALITY

The presented work contributes to the field of theoretical physics through an extensive exploration of the SU(2) Higgs 3D EFT using lattice Monte-Carlo simulations. This effective framework acts as a potent paradigm for comprehending the thermodynamics at high temperatures within the SM's electroweak sector, alongside diverse BSM.

The research emphasizes the region of parameter space linked to first-order PTs, a domain pertinent to planned gravitational wave experiments and potential electroweak baryogenesis. The findings not only expand upon prior studies but also provide essential data for quantitatively characterizing first-order phase transitions in extended electroweak sectors. The approach introduced enables direct extraction of nonperturbative thermodynamic properties in associated 4D models. Moreover, the study contributes insights into the bubble nucleation rate and its implications for gravitational wave spectra.The work's relevance is underscored by its applicability to scenarios involving new degrees of freedom with significant masses. This is particularly relevant during the symmetry-breaking transition. This research augments understanding of key thermodynamic quantities, facilitating rigorous testing of perturbative and nonperturbative methodologies. The exploration of higher-order perturbative expansions enhances the accuracy of approximations, while the potential extension to the U(1) Higgs model presents further opportunities for investigating the Infrared Problem. Lastly, the study highlights the demand for improved algorithms tailored to efficiently simulate bubble nucleation, advocating for continued advancements in computational techniques.

ELECTROWEAK PHASE TRANSITION IN THE EARLY UNIVERSE

September, 2023

Sinan GÜYER

ABBREVIATIONS

L Latent Heat

3D 3-Dimensional

4D 4-Dimensional

BSM Beyond the Standard Model

C Charge

CMBR Cosmic Microwave Background radiation

CP Charge Parity

DECIGO the Japanese space gravitational wave antenna

EFT Effective Field Theory

EWPT Electroweak Phase Transition

FLWR Friedmann-Lemaitre-Robertson-Walker

IR Infrared Problem

LHC Large Hadron Collider

LIGO The Laser Interferometer Gravitational-Wave Observatory

LISA Laser Interferometer Space Antenna

LO leading order

NLO next-to-leading order

NNLO next-to-next-to-leading order

PT Phase Transition

QCD Quantum chromodynamics

SM Standard Model

SU Special Unitary

SU(2) Special Unitary group 2

U(1) Unitary group 1

VIRGO European Gravitational Observatory

SYMBOLS

β parameter is related to the lattice spacing and the gauge coupling constant

η_x rate of change of the coupling y

η_x the rate of change of the coupling x

$\eta_{g_3^2}$ the rate of change of the coupling g_3^2

Γ nucleation rate

$\mathscr{D}\phi$ Operator for $\mathscr{D}\phi$

∇ lattice gradient operator

ρ energy density

g_3 SU(2) gauge coupling constant

k_B Stephan Boltzmann Constant

m_3 the mass of the Higgs boson in a 3D theory

N_t the number of lattice sites

$R_{\mu\nu}$ Ricci tensor

T Temperature

T_c Critical Temperature

x parameter is related to the Higgs mass and the temperature of the system

y parameter is related to the self-coupling of the Higgs field and the gauge coupling constant

σ^a Surface tension

σ^a Pauli matrices

A^a_μ gauge field

D_μ gauge covariant derivative

$g_{\mu\nu}$ the symmetric two rank tensor

L_G Higgs Field Langrangian

L_G Gauge Field Langrangian

m_D Debye Mass Screening

p pressure

$T_{\mu\nu}$ Energy Momentum Tensor

L_{int} interaction term between the gauge field and the Higgs field

G Gravitational Constant

LIST OF FIGURES

Figure 1.1 SM Phase Diagram 10

Figure 1.2 The forms of the potential and order parameter due to the changing temperature. 12

Figure 1.3 Figure shows the two peak structure from Lattice Monte-Carlo simulations. 13

Figure 4.1 The graphs depict the average Higgs quadratic condensate using the $\overline{\text{MS}}$ prescription in the continuum limit, revealing distinct phases and a first-order transition with a double peak pattern, along with reduced inter-phase probability as the system size increases and moderate variation with lattice spacing shown in the upper and lower graphs respectively. 35

Figure 4.2 Comprarasions of lattice results and perturbative approximations . . . 41

Figure 5.1 The Higgs condensate at $x_* = 0.0983(15)$ 47

Figure 5.2 The quartic Higgs condensate exhibits a substantial discontinuity. . . 47

Figure 6.1 The lattice results from the surface tension 53

Figure 9.1 The Probability distribution of phases and critical bubble 63

Figure 9.2 Bubble configuration update steps and crossings 65

Figure 9.3 The nucleation rate's dynamical prefactor. 66

Figure 9.4 Dynamical prefactor behaviour with changing Higgs field updates . . . 71

Figure 9.5 On left, we display data obtained from finite lattices along with the extrapolation to the continuum. On right, we compare the extrapolated rate with two perturbative approximations. 76

Figure 9.6 The bubble nucleation rate for two less pronounced transitions studied is shown, along with two perturbative approximations. 76

Figure 10.1 Bubble nucleation configuration 81

Figure 11.1 The results obtained from the lattice simulations conducted in this study are showcased alongside those from references 89

Figure 11.2 Transition at critical point 90

Figure 13.1 The critical mass y_c for two different values of x. 108

Figure 13.2 The Higgs quadratic condensate for two different values of x. 109

Figure 13.3 Extrapolations for surface tension at specific value of $x = 0.025$ and $x = 0.075$ 110

Figure 13.4 Lattice Monte Carlo Simulation results for Surface Tension 111

Figure 13.5 The nucleation rate is extrapolated to the continuum limit for two different values of x. 112

LIST OF TABLES

Table 7.1 Tle Lattice Monte Carlo Results for equilibrium quantities 55

Table 9.1 Bubble Nucleation results for x values and volumes 77

Table 9.2 Lattice Monte Carlo Results 78

Table 11.1 Analyzed specifically at the percolation threshold. 90

Table 13.1 Equilibrium Thermodynamics and * for $O(a)$ 117

1. INTRODUCTION

Particle physics researchers have been greatly informed by the Standard Model (SM) for a significant period. In 2012, the significant contribution of the Large Hadron Collider (LHC)became evident in the breakthrough related to the Higgs Boson revelation. This particle stands as a crucial element within SM [1]. Although the SM is a powerful tool, there are big failures in certain aspects such as baryon asymmetry, and it does not cover the whole story. Scientists are actively engaged in developing theories aimed at identifying the components that elude the Standard Model. These theories, collectively referred to as Beyond the Standard Model (BSM), serve as avenues of exploration for researchers. An illustration of BSM theories can be observed by examining the first order phase transition that occurred in the early universe. This phenomenon serves as an example highlighting the endeavors of researchers in understanding the fundamental principles beyond the confines of the SM. First order phase transitions (PT) takes an important place in the time history of the early universe. This is not only output of the PTs, also in this epoch, gravitational waves enters the story as an output of the thermodynamical processes of first order electroweak PTs. Theories can be limitless, and they can reach lots of possible scenarios under certain conditions, but scientists need qualitative, observational data to perform early universe PTs in the real world. LHC is a good example to test the theoretical research and to set the limitations and requirements. In the case of gravitational wave observations, LIGO and VIRGO have opened a new era with the first direct detection of Gravitational Waves (GW) in 2015 [2] as earth-based observation. What about space based observations? Will there be a more direct testing of the electroweak phase transition and gravitational waves? There are planned space based laser interferometers namely LISA (Laser Interferometer Space Antenna), the Japanese space gravitational wave antenna (DECIGO), and Taiji a Chinese space based gravitational-wave detector [2–4]. The simulations show that first-order electroweak phase transitions produce a stochastic gravitational wave background in the range up to mHz. These space-

based observations can reach the desired TeV scales, and the shape of the captured signal can give this information about what era the signal came from, and the models limit themselves to the early universe [2]. The electroweak phase transition and possible symmetry breaking presents an intriguing field, as it offers the necessary circumstances for the emergence of an asymmetry between matter and antimatter through Electroweak baryogenesis. The prerequisites for baryogenesis, recognized as the Sakharov criteria, encompass the subsequent elements: the absence of baryon number conservation, breaches in Charge (C) and Charge-Parity (CP) symmetries, and a deviation from thermal balance. These conditions collectively contribute to our understanding of baryogenesis and aid in exploring physics BSM. These conditions can be fulfilled by sufficiently strong first order Electroweak Phase Transition (EWPT) [5, 6].

The study of the EWPT within the SM entails the utilization of a combination of EFT and Lattice Monte Carlo simulations. The findings of this study indicate that the transition manifests as a cross-over occurring around a pseudo-critical temperature of 159.5 ± 1.5 GeV. [7]. On the other hand, new physics, and models applicable to the electroweak scale presents the nature of EWPTs. During strong first-order PTs, the bubbles begin to nucleate, and the nucleated bubbles form a bubble wall in the plasma. Particles scatter off the bubble walls, and this produces asymmetries in front of the bubble walls. This is called C and CP violations. The C and CP violations trigger changes on electroweak sphaleron transitions, thus baryon is produced more than anti-baryons. Expanding bubble and the corresponding bubble shell attempts to break symmetric phase [5, 6, 8]. The properties of the matter at high temperatures contain many important experimental and cosmological applications. Quantum chromadynamics (QCD) can be relevant to heavy ion collisions at high temperature and density, while finite temperature phase transition may play an important role in the evaluation of the universe. Purely analytical perturbative study of gauge theories is impossible because of the problem called Infrared Problem at Yang-Mills field. The direct way of calculation of the static equilibrium properties at high temperatures is 4 dimensional (4D) Lattice Monte Carlo Simulation. However, usage of

the 4D Lattice Monte Carlo is difficult in so many cases. The equivalence between finite temperature equilibrium field theory and zero temperature Euclidean field theory with a compact fourth dimension suggests a natural concept of reducing four-dimensional (4D) systems to three-dimensional (3D) ones. This understanding allows for simplification and analysis of physical phenomena within a lower-dimensional framework. e concept of dimensional reduction stems from specific attributes of a high-temperature plasma in equilibrium. This can be inferred from a 3D effective theory, which offers the benefit of not incorporating the Infrared Problem (IR).

1.1. Early Universe

The fundamental framework of our comprehension regarding the Universe's evolution is rooted in the hot big bang cosmology. This theory was established through pivotal findings like the detection of the Cosmic Microwave Background radiation (CMBR) and the observation of the Hubble expansion. The detection of CMBR and the observation of the Universe's expansion through the Hubble's law provided compelling evidence for a model in which the Universe originated from a hot and dense state, commonly known as the big bang. These breakthroughs have played a crucial role in shaping our understanding of the origin, composition, and evolution of the Universe. This model incorporates the redshift phenomenon observed in galaxies located far away, along with the abundance of light elements found in the cosmos. One of the important output of this model is the observed CMBR shows isotropy.

One may have a look at the modern cosmology to have a better understanding on early universe. Modern cosmology states that the universe is isotropic and homogeneous, meaning that one can say the Earth has no special place in the universe. Observation should be the same in every direction. The homogeneity allows us to study topology of the universe, and homogeneity assumptions made scientist to space-time coordinates simpler. The dynamics of the space times metric is described by the Einstein field equation.

$$R_{\mu\nu} - \frac{1}{2} R g_{\mu\nu} = 8\pi G T_{\mu\nu} \tag{1.1}$$

$R_{\mu\nu}$ is the Ricci tensor, $g_{\mu\nu}$ is the symmetric two rank tensor, G stands for the gravitational constant and lastly $T_{\mu\nu}$ is the energy-momentum tensor.

A simpler form was worked out first by Friedmann, and then Robertson and Walker took isotropy and homogeneity together. Friedmann-Lemaitre-Robertson-Walker (FLWR) metric is the exact solution to Einstein's field equation in terms of the isotropic and homoge-

neous universe.

$$ds^2 = -dt^2 + a(t)^2 \left(\frac{dr^2}{1-kr^2} + r^2 d\Omega^2 \right) \tag{1.2}$$

where $d\Omega = d\Theta^2 + sin^2\Theta d\Phi^2$ and k stands for as constant, representing the curvature of the space. Θ and Φ are azimuthal and polar angels of the spherical coordinates respectively.

In this metric, scale factor $a(t)$ applied to spatial components to track expansion of the universe.

We must establish a connection between time and temperature by utilizing the energy-momentum tensor within Einstein's Field equations and applying it to FLWR metrics. In an isotropic and homogeneous Universe, the energy-momentum assumes the following form; $T_{\mu\nu} = diag(-\rho, p, p, p)$. Here is ρ is the energy density and p is the pressure.

When energy-momentum tensor equals zero, the tensor takes the above form

$$\frac{d\rho}{dt} = -3H(t)(\rho + p) \tag{1.3}$$

It states that, while the boundary is expanding, the work done by pressure is equal to energy loss of a comoving sphere of radius $a(t)$.

When Einstein field equations apply to FLWR metrics, one can reach the Friedmann equations,

$$H^2 = \left(\frac{\dot{a}(t)}{a(t)} \right)^2 = \frac{8\pi G}{3}\rho - \frac{k}{a^2} \tag{1.4}$$

H is the Hubble parameter, $H = \frac{\dot{a}}{a}$.

From the continuity equation (1.3), the Friedmann equation can be written as;

$$\rho - \frac{3H^2}{8\pi G} = \frac{3H^2}{8\pi G}\frac{k}{(aH)^2} \tag{1.5}$$

As we are working in the flat universe, one can take $k = 0$, and thus equation (1.5) becomes

$$\rho = \frac{3H^2}{8\pi G} \tag{1.6}$$

For a radiation dominated universe, equation with a perfect fluid, Friedmann equations can be simplified further;

averaging $(\rho + p) = k\rho$, we can get the relevant proportional as $\rho_r \propto k^{-4}$ for the radiation dominated universe, since $p = \frac{\rho}{3}$. On the other hand, in the matter dominated universe $p = 0$ and the proportion is $\rho_r \propto k^{-3}$. Substituting these relations to the Friedmann equations, the scale factor grows as $a(t) \propto t^{\frac{2}{3}}$, and $a(t) \propto t^{\frac{1}{2}}$ respectively.

To derive the connection between time and temperature within a universe dominated by radiation, we can commence by examining the Friedmann equation:

$$H^2 = \left(\frac{\dot{a}(t)}{a(t)}\right)^2 = \frac{8\pi G}{3}\rho - \frac{k}{a^2} \tag{1.7}$$

In a radiation-dominated universe, the energy density ρ can be written as:

$$\rho = cT^4 \tag{1.8}$$

where c is a constant. We can rewrite the Friedmann equation as:

$$\left(\frac{\dot{a}(t)}{a(t)}\right)^2 = \frac{8\pi G}{3}cT^4 - \frac{k}{a^2} \tag{1.9}$$

Now, let's consider the time derivative of the energy density:

$$\frac{d\rho}{dt} = \frac{d}{dt}\left(cT^4\right) = 4cT^3\frac{dT}{dt} \tag{1.10}$$

Using the continuity equation $\frac{d\rho}{dt} = -3H(\rho + p)$, where p is the pressure, we have:

$$4cT^3\frac{dT}{dt} = -3H\left(cT^4 + p\right) \tag{1.11}$$

Within a universe dominated by radiation, the pressure can be expressed as $p = \frac{\rho}{3}$, allowing us to formulate:

$$4cT^3\frac{dT}{dt} = -3H\left(cT^4 + \frac{\rho}{3}\right) \tag{1.12}$$

Substituting the expression for $\rho = cT^4$, we get:

$$4cT^3\frac{dT}{dt} = -3H\left(cT^4 + \frac{cT^4}{3}\right) \tag{1.13}$$

Simplifying the equation:

$$4cT^3\frac{dT}{dt} = -3H\left(\frac{4cT^4}{3}\right) \tag{1.14}$$

Dividing both sides by $4cT^3$ and rearranging the terms:

$$\frac{dT}{T} = -\frac{3H}{4}dt \tag{1.15}$$

Integrating both sides:

$$\int \frac{1}{T}dT = -\frac{3}{4}\int Hdt \tag{1.16}$$

Integrating gives:

$$\ln(T) = -\frac{3}{4}\int Hdt + \ln(A) \tag{1.17}$$

where A is an integration constant. Taking the exponential of both sides:

$$T = Ae^{-\frac{3}{4}\int Hdt} \tag{1.18}$$

The scale factor $a(t)$ is proportional to $t^{\frac{1}{2}}$. So we can write $H = \frac{\dot{a}}{a} = \frac{1}{2t}$. Substituting this into the expression:

$$T = Ae^{-\frac{3}{4}\int \frac{1}{2t}dt} = Ae^{-\frac{3}{8}\ln(t)} = At^{-\frac{3}{8}} \tag{1.19}$$

Now, to determine the constant A, we can use the temperature at a particular time t_0. Let's say T_0 is the temperature at t_0. Substituting $T = T_0$ and $t = t_0$ into the equation, we have:

$$T_0 = At_0^{-\frac{3}{8}} \tag{1.20}$$

Solving for A, we get:

$$A = T_0 t_0^{\frac{3}{8}} \tag{1.21}$$

Finally, substituting this back into the equation for T, we obtain the relation between time and temperature in a radiation-dominated universe:

$$T = T_0 \left(\frac{t_0}{t}\right)^{\frac{3}{8}} \tag{1.22}$$

where T is the temperature at time t, and T_0 is the temperature at a reference time t_0.

1.2. The Electroweak Phase Transitions

As far as we know, there are two types of cosmological phase transitions in the very early stages of the universe; the first is EW and the second is QCD. The EW and QCD phase transitions can be divided into first order and cross phase transitions, respectively [9].

The early universe was hot and dense in the era of radiation dominated. The universe then gradually became colder and colder, this process led to phase transitions as in the boiling water. Electroweak era covers the 10^{-38} to 10^{-10} seconds time range after the Bing Bang, and takes place in the early universe, when the universe starts to cool down. Symmetry breaking is led by the formation of the Higgs field. There are symmetric and broken phases in the electroweak phase transition, which we will discuss symmetric and broken phases in more detail in the next chapter, whereas the SM has a cross-over, and the pseudo-critical temperature is 159 ± 1.5 GeV to happen phase transition [7], meaning that there is no particular point that separate phases as symmetric and broken. At this point, the order of the phase transition becomes important in order to fulfill the successful baryogenis. As previously indicated, the electroweak phase transition constitutes a crossover within the SM. Nevertheless, introducing supplementary elements like a solitary additional scalar field or adjoint Higgs fields facilitates the potential for a first-order phase transition during

the EWPT [10]. Mainly, the first order electroweak phase transition is a good candidate to find the missing part of the baryogenesis at electroweak scale, and also during the thermal processes, gravitational waves can be produced by the bubble nucleation, expansion, and collision. We will turn back to bubble nucleation.

As mentioned earlier, although the discovery of the Higgs boson at the LHC confirms that scalar field-driven symmetry breaking has been confirmed in the early universe, there is no direct evidence for new physics encompassing the energy scale of the electroweak sector. Within the scope of this information, gravitational waves detection from the first order phase transition offers direct testing opportunity to understand the nature of the electroweak phase transition [9].

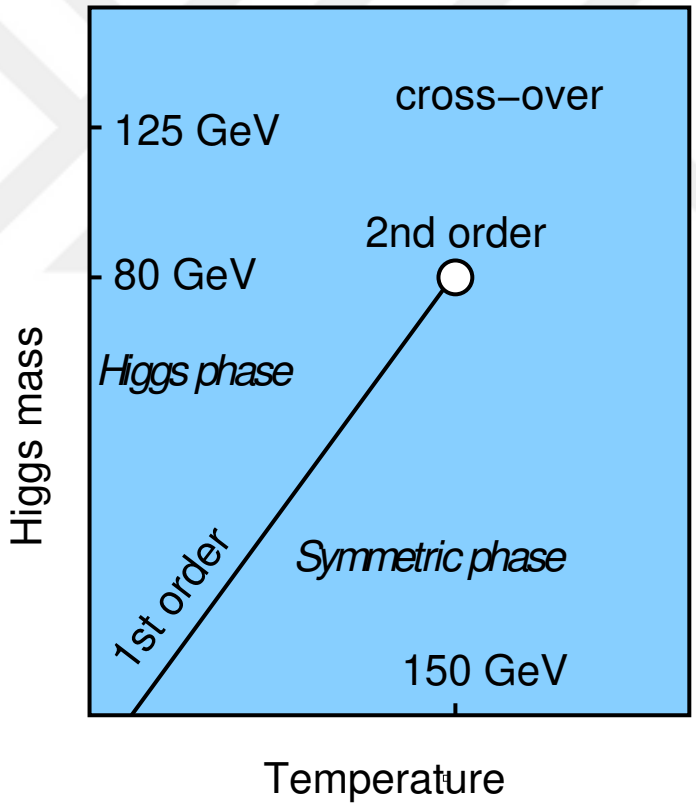


Figure 1.1 SM Phase Diagram, Figure taken from Ref. [11]

.

As a summary of the section, the **Figure 1.1** explains that in the SM, phase transition is fast, and there is no discontinuity for larger Higgs masses. Under $m_H \leq 75$ GeV, SM is becoming a first order phase transition.

1.2.1. First-Order Electroweak Phase Transition

First-order phase transition is explained in the previous chapter, but let's delve into it further. Effective potential is the crucial tool to calculate phase transition, it could be done by two ways, one is perturbative calculation and the other is Monte-Carlo simulations. We will turn back to this subject in the Lattice Calculations method chapter.

Effective potential $V_{eff}(\Phi, T)$, changes its shape with the temperature.The configuration takes shape based on the sequence of the transition, referred to as the order parameter. Furthermore, the classification of the phase transition as first or second order is determined by the characteristics of the transition itself. One can separate the temperatures to three cases, one is while temperature is decreasing, it hits to critical temperature $T = T_c$, $T < T_c$, and $T > T_c$. In the first case, effective potential shows two degenerate minima, and below the T_c the Universe becomes metastable, trapped in a false vacuum which is also called symmetric phase. Quantum tunnelings and thermal fluctuations help to reach true vacuum state, namely broken phase. In the third case, if the temperature is way above the $T >> T_c$, V_{eff} has a minimum at $\Phi = 0$, and if $T > T_c$, V_{eff} forms second but higher Φ minimum. Obviously, T_c is an important feature in EWPT. T_c tells us that, symmetric and broken phases have the same free energy.

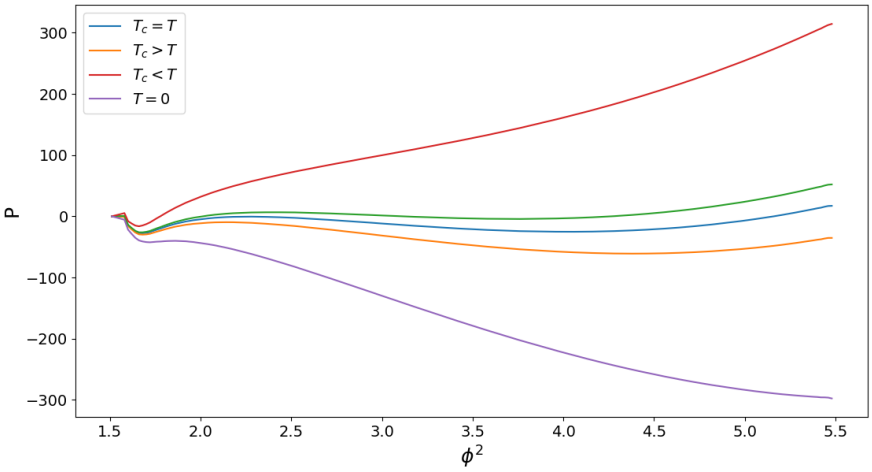


Figure 1.2 The forms of the potential and order parameter due to the changing temperature.

Let's have a closer look when $T_c = T$,

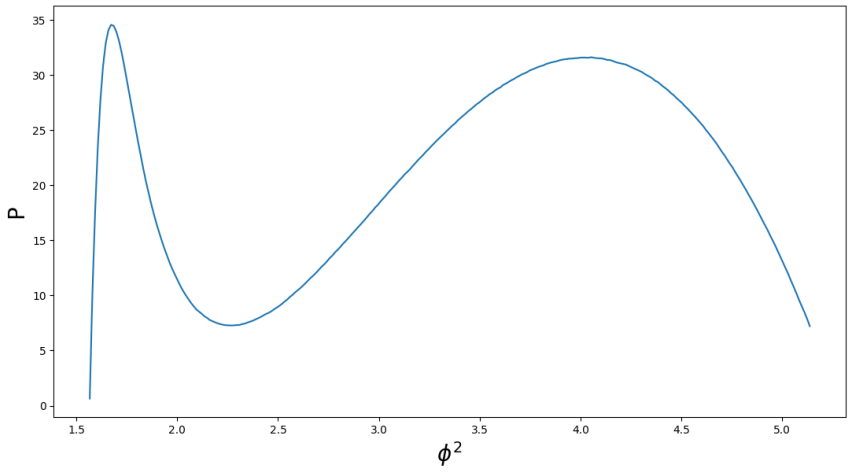


Figure 1.3 Figure shows the two peak structure from Lattice Monte-Carlo simulations.

1.2.2. Lattice Gauge Theory

Lattice gauge theory is a method for numerically simulating gauge theories. Gauge theories are a type of field theory that describes the interactions between elementary particles, such as the strong nuclear force that holds atomic nuclei together. In gauge theories, particles interact through gauge fields, which are fields that are associated with a particular symmetry. Lattice gauge theory discretizes the continuous spacetime of the gauge theory into a lattice of points, and the gauge fields are defined on the links between the lattice points. By discretizing spacetime, lattice gauge theory allows for numerical simulations of gauge theories using powerful computer algorithms, which can provide insights into the behavior of the theory that are difficult to calculate using other methods.

Elitzur's theorem, on the other hand, is a theoretical result that applies to gauge-invariant theories. A gauge theory is a type of theory that is invariant under a local symmetry transformation, which means that the theory remains the same even if the gauge fields are transformed in a particular way at each point in spacetime. Elitzur's theorem states that a gauge-invariant theory cannot have a non-zero vacuum expectation value for a gauge-

invariant operator that violates the gauge symmetry. In other words, if a physical system has a gauge symmetry, then any observable quantity that violates this symmetry cannot have a non-zero expectation value in the vacuum state. Elitzur's theorem has important implications for the study of confinement in gauge theories, and for the understanding of the Higgs mechanism.

Elitzur's theorem applies to gauge-invariant theories and states that a gauge-invariant theory cannot have a non-zero vacuum expectation value for a gauge-invariant operator that violates the gauge symmetry. In other words, if a physical system has a gauge symmetry, then any observable quantity that violates this symmetry cannot have a non-zero expectation value in the vacuum state. Elitzur's theorem implies that the symmetry cannot be spontaneously broken in the sense of producing a non-zero vacuum expectation value of a gauge-invariant operator that breaks the symmetry. This is because such an expectation value would violate the gauge symmetry.

On the other hand, within gauge theories, symmetry breaking pertains to a scenario wherein the ground state or vacuum of the theory exhibits reduced symmetry compared to the Lagrangian of the theory. This phenomenon occurs in certain gauge theories through the utilization of the Higgs mechanism, which results in the spontaneous breaking of gauge symmetry and the acquisition of mass by some of the gauge bosons. In the Higgs mechanism, the gauge symmetry is not violated, but the ground state of the theory has a lower symmetry than the Lagrangian, which leads to a change in the spectrum of the theory and the appearance of massive gauge bosons.

So, to summarize, Elitzur's theorem and gauge theories both involve symmetry breaking, but in different senses. Elitzur's theorem prohibits symmetry breaking in the sense of producing a non-zero vacuum expectation value of a gauge-invariant operator that breaks the symmetry, while symmetry breaking in gauge theories refers to a situation where the ground state of the theory has less symmetry than the Lagrangian of the theory, which can occur through the Higgs mechanism.

2. 3D LATTICE MONTE-CARLO SIMULATIONS

2.1. Lattice Monte Carlo Method

One can define the method in a simple manner with the steps;

- Define the lattice: The initial stage of the lattice Monte Carlo approach involves defining a lattice. A lattice is a regular grid of points in space, and each point on the lattice represents a degree of freedom of the system being simulated. For example, in a lattice simulation of a gas, each point on the lattice might represent the position of a particle.
- Initialize the lattice: Once the lattice is defined, it must be initialized with some initial conditions. For example, in a lattice simulation of a gas, the particles might be initially distributed randomly throughout the lattice.
- Choose a move: The next step is to choose a move to make on the lattice. This could be anything from moving a particle to a neighboring lattice site to flipping a spin on a lattice site.
- Calculate the change in energy: Once a move is chosen, the change in energy associated with that move must be calculated. This encompasses the computation of the system's energy both prior to and subsequent to executing the move.
- Apply the Metropolis algorithm: The Metropolis algorithm is a probabilistic method for accepting or rejecting a proposed move. The probability of accepting a move is given by the Boltzmann factor, which depends on the change in energy associated with the move. If the move is accepted, the lattice is updated to reflect the new configuration. If the move is rejected, the lattice remains unchanged.
- Repeat: Steps 3-5 are repeated many times, with a different move chosen each

time. The goal is to generate a large number of configurations of the lattice that are statistically representative of the behavior of the system being simulated.

- Analyze the results: Once the simulation is complete, the results are analyzed to extract information about the behavior of the system being simulated. This could involve calculating the average value of a quantity of interest, such as the pressure or energy of a gas, or studying the distribution of lattice configurations to look for patterns or phase transitions.

Canonical Monte Carlo:

The probability distribution characterizing the canonical ensemble at temperature T is described by the Boltzmann distribution:

$$P(E) = \frac{1}{Z(T)} e^{-\beta E} \tag{2.1}$$

where E stands for energy of the system, $\beta = \frac{1}{k_B T}$ is the inverse temperature, k_B is the Boltzmann constant, and $Z(T) = \sum_i e^{-\beta E_i}$ is the partition function, which sums over all possible states of the system. In lattice Monte Carlo simulations, the energy of the system is often calculated as a sum over the energy of each lattice site:

$$E = \sum_{i,j,k} \varepsilon_{i,j,k} \tag{2.2}$$

where $\varepsilon_{i,j,k}$ is the energy of the lattice site at position (i, j, k). The Metropolis algorithm is commonly used to generate configurations of the system that are distributed according to the Boltzmann distribution. The basic steps of the algorithm are:

Start with an initial configuration of the system. Choose a random site on the lattice and attempt to change its value. Compute the energy difference, denoted as ΔE, between the newly generated and the previous configurations. Decide to accept the fresh configuration

with a probability denoted as $P_{\text{accept}} = \min(1, e^{-\beta \Delta E})$. Repeat steps 2-4 for a large number of iterations.

Multicanonical Monte Carlo:

The multicanonical ensemble is a modification of the canonical ensemble that introduces a weight function $w(E)$ to help the simulation sample the energy landscape more efficiently. The probability distribution for the multicanonical ensemble is given by:

$$P(E) \propto \frac{1}{w(E)} e^{-\beta E} \tag{2.3}$$

The weight function is commonly selected as the reciprocal of the density of states $g(E)$, representing the count of states possessing the energy level E:

$$w(E) = \frac{1}{g(E)} \tag{2.4}$$

The density of states can be estimated during the simulation using the Wang-Landau algorithm or other similar methods. In practice, the multicanonical algorithm involves updating the weight function and performing the Metropolis algorithm as usual, but with the energy-dependent weight function. The objective is to adjust the weight function in a manner that levels the energy landscape, thereby simplifying the process of sampling states characterized by lower probabilities.

Canonical and multicanonical Monte Carlo simulations can be used to study a wide range of physical phenomena, including phase transitions, critical phenomena, and thermodynamic properties of materials. By providing a way to simulate complex systems in a computationally efficient way, these methods have become an important tool for researchers in many different fields [12–14].

2.2. Dimensional Reduction

Within this section, we will elucidate the overall attributes and merits of dimensional reduction;

First, the process of dimensional reduction involves transforming the high temperature theory in 4D into an effective 3D theory. The resulting theory retains one, or possibly even two, crucial mass scales that are lower than those present in the original 4D theory. At high temperatures, the dimensional reduction of the 4D high-temperature theory leads to an effective 3D theory that incorporates one or possibly two fundamental mass scales less than the underlying 4D theory. In the context of the 4D theory, the temperature T serves as one of the characteristic scales, accompanied by the Debye screening mass denoted as m_D, approximately proportional to g_T, and the infrared scale expressed as $g^2/3 = g^2T$. On the other hand, in the context of the simplified 3D theory, the relevant scales are symbolized by m_D and $g^2/3$ (or only $g^2/3$ if we integrate out the temporal aspect of the gauge field). The resulting 3D theory serves as a highly accurate approximation to the four-dimensional world, especially for realistic Higgs masses. Moreover, this theory exhibits a super-renormalizable nature, making it significantly more amenable to analysis using perturbative or non-perturbative methods. Unlike the 4D theory, which manifests ultraviolet divergences at any perturbation order, the 3D theory only exhibits divergences in 1- and 2-loop graphs. This simpler scaling behavior facilitates the establishment of relationships between lattice and continuum parameters, and enables computations with a high degree of precision.

Second, due to the super-renormalizable nature of the 3D gauge-Higgs system, an exact correlation emerges between the lattice couplings and the couplings within the 3D theory. This relation remains valid in the continuum limit and enables the establishment of connections between lattice observables and their corresponding physical counterparts, given specific Higgs and W masses. The exact relation is a result of the absence of contributions

from 3-loop or higher-order terms to the renormalization process within the 3D theory.

Thirdly, within the framework of the 4D theory, both fermion masses and non-static mode masses of bosons experience concurrent significant increases, thereby posing challenges when attempting to integrate fermions in the proximity of T_c. Thus, the 4D to 3D dimensional reduction is necessary for accuracy. Moreover, it's important to note that a practical electroweak theory incorporates chiral fermions, which currently cannot be represented on a lattice and thus require analytical integration. This circumstance leads to the realization that the 4D bosonic theory, amenable to lattice study, ultimately functions as an effective theory. Consequently, it does not inherently surpass the utility of a dimensionally reduced 3D counterpart.

Lastly, perturbative computations in the 3D effective theory are greatly simplified compared to resummed perturbation theory in 4D, enabling a more comprehensive comprehension of the substantial 2-loop logarithmic corrections within the MS scheme, and facilitating the implementation of a summation technique for these corrections grounded in the principles of the renormalization group.

Overall, these advantages of the 3D effective theory make it more efficient and accurate in studying the high-temperature electroweak phase transition, especially for realistic Higgs masses.

2.3. Lattice Monte Carlo Simulations for 3D

Employing lattice Monte Carlo simulations to analyze the behavior of the EW theory within EWPT in the 3D SU(2) Higgs model constitutes a non-perturbative method. This approach involves studying the theory's dynamics on a discrete lattice. In this approach, space and time are discretized onto a grid or lattice, and the equations of motion for the fields are approximated numerically using Monte Carlo techniques.

The 3D SU(2) Higgs model is a simplified version of the electroweak theory, which de-

scribes the interactions of the electromagnetic and weak forces. It consists of a gauge field, which describes the force between particles, and a scalar field, which gives mass to the particles.

The electroweak phase transition denotes a pivotal juncture in the early universe, characterized by the emergence of a non-zero Higgs field and the subsequent breaking of the electroweak symmetry. This breaking mechanism is responsible for the acquisition of mass by the W and Z bosons. The lattice Monte Carlo simulations for the 3D SU(2) Higgs model can be used to study the properties of the electroweak phase transition, including the critical temperature and the behavior of the scalar field near the critical point.

The Lagrangian density for the 3D SU(2) Higgs model can be written in Equation 2.5 :

$$L = L_G + L_H + L_{int} \tag{2.5}$$

where L_G is the gauge field Lagrangian, L_G is the Higgs field Lagrangian, and L_{int} is the interaction term between the gauge field and the Higgs field. The gauge field Lagrangian is given by Equation 2.6:

$$L_G = -\frac{1}{4} F^a_{\mu\nu} F^{\mu\nu a} \tag{2.6}$$

where $F^a_{\mu\nu}$ is the field strength tensor for the gauge field, and a is a gauge index that runs from 2.1 to 2.3. The Higgs field Lagrangian is given by Equation 2.7 :

$$L_H = (D_\mu \phi)^\dagger (D^\mu \phi) - V(\phi) \tag{2.7}$$

where ϕ is the Higgs field, D_μ is the gauge covariant derivative, and $V(\phi)$ is the scalar potential that gives mass to the W and Z bosons. The interaction term between the gauge field and the Higgs field is given by Equation 2.8:

$$L_{int} = ig(D_\mu \phi)^\dagger \sigma^a (D_\mu \phi) A^a_\mu \tag{2.8}$$

where g is the gauge coupling constant, σ^a are the Pauli matrices, and A^a_μ is the gauge field.

In lattice Monte Carlo simulations, the fields are defined on a 3D lattice, and the derivatives in the Lagrangian equations are replaced with finite differences. The Higgs field and the gauge field undergo updates employing a Markov chain Monte Carlo algorithm. This algorithm generates a series of configurations that effectively sample the probability distribution of these fields.

Through the process of simulating the Higgs field and the gauge field at varying temperatures, researchers can investigate the dynamics of these fields in proximity to the critical temperature associated with the electroweak phase transition. This enables them to compute essential properties like the critical temperature, correlation length, and order parameter.

The effective potential corresponding to the Higgs field encapsulates the energy density linked to various field values of the Higgs. For the scenario of the 3D SU(2) electroweak phase transition excluding U(1) contribution, the specific form of the Higgs effective potential can be expressed as Equation 2.9:

$$V(\phi) = -\mu^2\phi^2 + \lambda\phi^4 \tag{2.9}$$

where ϕ is the Higgs field, μ^2 is a constant parameter, and λ is the self-coupling constant of the Higgs field.

The first term, $-\mu^2\phi^2$, represents the quadratic contribution to the effective potential. This term has a negative coefficient, which means that the potential is minimized at non-zero values of the Higgs field, i.e., the Higgs field acquires a non-zero vacuum expectation value.

The second term, $\lambda\phi^4$, represents the quartic contribution to the effective potential. This

term has a positive coefficient, which means that the potential is minimized at larger values of the Higgs field.

The shape of the effective potential depends on the values of the parameters μ^2 and λ. If μ^2 is positive and λ is small, the potential has a single minimum at $\phi = 0$, and the Higgs field has a zero vacuum expectation value. However, when μ^2 takes a negative value and λ attains sufficient magnitude, the potential reveals two distinct minima. One of these minima corresponds to $\phi = 0$, while the other exists at a nonzero value of the Higgs field. Under these circumstances, the Higgs field undergoes a phase transition when the critical temperature is reached. This transition marks a pivotal point at which the potential transitions from possessing a sole minimum at $\phi = 0$ to featuring dual minima.

Throughout this phase transition, the Higgs field acquires a vacuum expectation value that is non-zero. This particular development leads to the breaking of the electroweak symmetry and consequentially imparts mass to the W and Z bosons. This transition holds significant importance in the context of the universe's evolution, as it is widely hypothesized to have exerted a pivotal influence in shaping the foundational structure of the universe on a large scale [15–17].

The partition function for the 3D SU(2) electroweak theory can be written in Equation 2.10:

$$Z = \int \mathscr{D}\phi \exp\left(-S_{\text{eff}}(\phi)/T\right), \tag{2.10}$$

where $\mathscr{D}\phi$ is the path integral measure, $S_{\text{eff}}(\phi)$ is the effective action, which includes the Higgs effective potential, and T is the temperature.

The lattice spacing a exhibits a correlation with the temperature, expressed by the relationship $T = 1/(aN_t)$, wherein N_t signifies the count of lattice sites in the temporal dimension. The order parameter for the electroweak phase transition is the expectation value of the Higgs field, which can be written as $\langle\phi\rangle = \frac{1}{V}\int d^3x\phi(x)$, where V is the volume of the system.

The Higgs potential is usually parametrized by dimensionless parameters x, y, and β, which are defined by Equation 2.11:

$$x = \frac{m_3^2}{T^2}, \quad y = \frac{\lambda}{g_3^2}, \quad \beta = \frac{4}{a g_3^3} \tag{2.11}$$

where m_3 is the mass of the Higgs boson in a 3D theory, T is the temperature of the system, λ is the Higgs self-coupling constant, g_3 is the SU(2) gauge coupling constant, and a is the lattice spacing.

The parameter x establishes a connection between the Higgs mass and the system's temperature. It characterizes the potency of the quadratic element within the Higgs potential, thereby shaping the potential's form. In cases where x is positive, the potential attains a minimum at the origin, signifying that the Higgs field holds a vacuum expectation value of zero. Conversely, when x is negative, the potential exhibits a minimum at a non-zero Higgs field value. This outcome denotes the breaking of the electroweak symmetry.

The parameter y is related to the self-coupling of the Higgs field and the gauge coupling constant. It signifies the intensity of the quartic component within the Higgs potential, dictating the curvature of the potential in the vicinity of its minimum. If y is small, the potential is almost quadratic, which means that the Higgs field has a small vacuum expectation value. If y is large, the potential is strongly influenced by the quartic term, which means that the Higgs field has a large vacuum expectation value.

The parameter β is related to the lattice spacing and the gauge coupling constant. It sets the scale for the temperature dependence of the potential. During elevated temperatures, the potential's characteristics are primarily influenced by the terms reliant on temperature, whereas lower temperatures grant predominance to terms contingent on mass[18, 19].

$$V(\phi) = -\mu^2 \phi^\dagger \phi + \lambda (\phi^\dagger \phi)^2 \tag{2.12}$$

The dimensionless parameters:

$$x = \frac{\mu^2}{g^2 T^2}\, y \qquad = \frac{\lambda}{g^4}\, \beta = \frac{2g^2}{\widetilde{m}}\, \widetilde{m}^2 \qquad = \frac{1}{3}(m_W^2 + 2m_Z^2) \tag{2.13}$$

The effective action:

$$S_{\text{eff}}[\phi] = \int d^3x \left[\frac{1}{2}(\partial_\mu \phi)^\dagger (\partial^\mu \phi) + V(\phi) + \frac{1}{2}\xi(\phi^\dagger \phi - v^2)^2 \right] \tag{2.14}$$

The partition function:

$$Z = \int [d\phi][d\phi^\dagger] e^{-S_{\text{eff}}[\phi]} \tag{2.15}$$

The order parameter:

$$\langle \phi^\dagger \phi \rangle = \frac{1}{V} \frac{\partial \ln Z}{\partial (g^2/T)} \tag{2.16}$$

The lattice spacing:

$$a = \frac{1}{gT} \tag{2.17}$$

3. EQUILIBRIUM QUANTITIES

In the first order EWPT, equilibrium quantities pertain to those that achieve balance precisely at the critical temperature where the transition takes place. At this critical temperature, the free energy of both coexisting phases—the symmetric phase and the broken phase—is equivalent, establishing a state of equilibrium where the system experiences mechanical, thermal, and chemical balance. The thermodynamic observable $\langle \phi^\dagger \phi \rangle$ holds a fundamental role in elucidating the nature of the electroweak phase transition. It is a gauge-independent quantity that can distinguish the different phases of the theory. At high temperatures, the symmetry-breaking phase is unstable and the system is in the symmetric phase where $\langle \phi^\dagger \phi \rangle$ is close to zero. At low temperatures, the system transitions to the symmetry-breaking phase where $\langle \phi^\dagger \phi \rangle$ acquires a non-zero value. The shift from one phase to another is a first-order transition, distinguished by a discontinuous change in $\langle \phi^\dagger \phi \rangle$ precisely at the critical temperature.

The equilibrium quantities in the first order electroweak phase transition are determined by the interplay between the thermodynamic forces that drive the transition and the dissipative forces that resist it. The dynamics of the transition can be studied using the effective potential of the theory, which is a function of the scalar field and temperature. The effective potential has two minima corresponding to the symmetric and symmetry-breaking phases. By scrutinizing the form of the effective potential and assessing the thermodynamic attributes of the two phases, crucial equilibrium quantities such as the critical temperature, latent heat, and nucleation rate can be computed.

To begin, the critical temperature T_c signifies the specific temperature at which both the symmetric and symmetry-breaking phases coexist, possessing equivalent free energies. At this critical temperature, the barrier that segregates the two minima within the effective potential vanishes, allowing the system to move between the two phases with an equal likelihood.

Secondly, the latent heat L characterizes the energy liberated or taken in for each volume unit throughout the transition. It is related to the difference in the free energy density between the two phases at the critical temperature, and this distinction embodies the energy demand for overcoming the potential obstacle that separates the two lowest points.

Thirdly, the nucleation rate Γ is the rate at which bubbles of the symmetry-breaking phase appear in the symmetric phase. It depends on the temperature and the barrier height, and it is related to the probability of forming a critical bubble that can expand and convert the entire system to the symmetry-breaking phase.

Finally, surface tension σ^a is a property of the interface between the two phases, and it determines the energy cost per unit area to create or expand the interface. Surface tension plays a crucial role in the dynamics of the transition, as it determines the rate of bubble nucleation and growth. The surface tension is related to the difference in free energy density between the two phases at the critical temperature, as well as the curvature of the interface. It can be calculated using methods such as the bag model or lattice simulations, and it provides important information about the dynamics of the transition. A high surface tension implies a slow bubble growth and a long-lived metastable state, while a low surface tension leads to fast bubble growth and a rapid transition.

In summary, the equilibrium quantities in the first order EWPT include the critical temperature, latent heat, nucleation rate, and surface tension. These quantities are determined by the thermodynamic properties of the symmetric and symmetry-breaking phases, and they play a crucial role in characterizing the nature and dynamics of the transition.

4. Critical Temperature

The critical temperature T_c holds paramount significance in the examination of a first-order EWPT. It is precisely defined as the temperature at which the free energies of both the symmetric and symmetry-breaking phases attain equality, ultimately instigating a first-order PT within the system.

When temperatures fall below T_c, the system enters the symmetry-breaking phase, characterized by the acquisition of a non-zero vacuum expectation value by the Higgs field. This event culminates in the breakdown of the electroweak symmetry, consequently endowing the W and Z bosons with their respective masses. At temperatures above T_c, the Higgs field has a zero expectation value, and the electroweak symmetry is unbroken. The critical temperature marks the point at which the two phases coexist with equal probability, and the transition between the two phases is characterized by a jump in the Higgs field expectation value.

The critical temperature is established through the configuration of the effective potential within the theory, which operates as a function of both the Higgs field and temperature. Within this potential, there exist two distinct minima corresponding to the symmetric and symmetry-breaking phases. At the critical temperature, the barrier that separates these minima vanishes. This pivotal temperature is contingent upon various parameters inherent to the theory, including the Higgs boson mass, the mass of the top quark, and the strength of the weak coupling constant.

Calculating the critical temperature in the electroweak theory is a challenging problem,

as it requires taking into account both quantum and thermal effects. One approach is to use the renormalization group equations to evolve the effective potential from high temperatures down to the critical temperature. An alternative methodology involves employing lattice simulations to directly calculate the free energy associated with the two distinct phases, thereby facilitating the determination of the critical temperature. Comprehending the critical temperature and the inherent characteristics of the EWPT holds paramount importance across various applications. These include elucidating the genesis of the matter-antimatter asymmetry within the universe and the creation of primordial gravitational waves.

In lattice simulations, the spacetime is discretized onto a finite grid, and the fields are defined at each lattice site. The partition function of the theory can then be expressed as a sum over all field configurations on the lattice, which can be evaluated numerically using Monte Carlo techniques.

To compute the free energy for both phases, it is imperative to establish an order parameter capable of differentiating between the two distinct states. Within the EW theory, this order parameter typically revolves around the Higgs field or a composite involving both Higgs and gauge fields.

By performing lattice calculations of the order parameter's expectation value at varying temperatures, it becomes possible to construct the effective potential within the theory. This approach allows for the identification of the positions of the minima associated with the two distinct phases. The free energy attributed to both phases can be determined by simulating the lattice while imposing fixed boundary conditions aligned with each respective phase. This simulation process involves measuring the energy density to compute the free energy for each phase. The critical temperature is then determined by the temperature at which the free energy of the two phases are equal. This can be achieved by simulating the lattice at a range of temperatures and fitting the energy density to a polynomial or spline function, and then determining the temperature at which the two functions inter-

sect.

In lattice simulations, the space-time continuum is discretized into a lattice with a finite spacing, which is denoted by the symbol a. The temperature of the system is related to the spacing of the lattice through the relation $T = 1/(aNt)$, where Nt is the number of lattice points in the temporal direction.

The lattice action for the 3D effective theory of the Higgs field is given by:

$$S = \sum_n \left[\frac{1}{2} (\nabla \phi(n))^2 + V(\phi(n)) + \lambda (\phi(n))^4 \right], \tag{4.1}$$

where n is a lattice site, $\phi(n)$ is the value of the Higgs field at that site, ∇ is the lattice gradient operator, $V(\phi(n))$ is the Higgs potential, and λ is the quartic coupling constant.

To perform Monte Carlo simulations, one needs to generate a large number of Higgs field configurations that are distributed according to the Boltzmann factor $e^{(-S/T)}$. This is done using a Markov chain Monte Carlo method, such as the Metropolis algorithm.

The simulations involve updating the field configurations randomly by proposing a new configuration and accepting or rejecting it based on the change in the action. The algorithm is designed to sample the configurations in a way that converges to the Boltzmann distribution.

To ascertain the critical temperature, the focus is directed towards identifying the temperature at which the system embarks on a phase transition, transitioning from the symmetric phase to the broken phase. This is typically characterized by a rapid change in the behavior of the Higgs field, such as a sharp drop in the order parameter or an increase in the correlation length.

The order parameter is a quantity that measures the degree of symmetry breaking in the system. When considering the Higgs field, the order parameter is represented by:

$$\Phi = \langle \phi \rangle \,, \tag{4.2}$$

$< \phi >$ is the thermal average of the Higgs field. At high temperatures, the system is in the symmetric phase and the order parameter is zero. At low temperatures, the system undergoes a phase transition and the order parameter becomes non-zero.

The correlation length is a measure of the spatial extent of fluctuations in the Higgs field. Upon reaching the critical temperature, the correlation length experiences divergence, signifying the emergence of extensive correlations spanning significant distances within the system. The correlation length is given by:

$$\xi = \frac{1}{m}, \tag{4.3}$$

To determine the critical temperature, one performs simulations at different temperatures and measures the behavior of the order parameter and the correlation length. The critical temperature is then determined by extrapolating the results to the thermodynamic limit, where the lattice spacing goes to zero and the system size goes to infinity.

This extrapolation is typically done using scaling relations, which relate the behavior of the order parameter and the correlation length to the lattice spacing and the system size. By fitting the simulation data to these scaling relations, one can extract the critical temperature and the critical exponents that characterize the behavior of the system at the critical point.

The lattice approach to calculating the critical temperature in the 3D effective theory of the Higgs field involves discretizing space-time into a lattice, performing Monte Carlo simulations to sample the Higgs field configurations, and analyzing the behavior of the order parameter and the correlation length to determine the critical temperature. The extrapolation to the thermodynamic limit is done using scaling relations, which relate the

behavior of the system to the lattice spacing and the system size.

Within the framework of this 4D BSM theory, a correspondence can be established between the theory and a particular point in the coupling parameter space of a 3D EFT. The 3D EFT serves as a simplified representation of the system's low-energy dynamics, capturing essential features while disregarding the intricate fundamental degrees of freedom.

The parameter space within the 3D EFT encompasses the couplings that dictate the interactions within the theory. These couplings dictate how the particles and fields within the theory interact with each other. By establishing a correspondence between the 4D BSM theory and a particular point in the space of couplings, a relationship between the two theories is established.

The properties and behavior of the 4D theory undergo transformations as the temperature fluctuates, impacting its thermodynamics. These changes are captured by a trajectory in the domain of connections within the 3D EFT. The temperature T and additional parameters $(x(T), y(T), g_3^2(T))$, which might hinge on the specific particulars of the BSM theory and the corresponding 3D EFT, define the trajectory.

A first-order PT refers to a transition between distinct phases of a system, such as from a liquid to a gas or from a solid to a liquid. Within the realm of coupling parameters in the 3D EFT, it is possible for specific surfaces to emerge that correspond to PTs of the first order. These surfaces can be described by an equation of the form $y = yc(x)$, where $yc(x)$ represents a function that determines the boundary of the surface.

If the trajectory traced by the thermodynamic evolution within the 4D theory intersects the surface of first-order PT, this signifies that at specific parameter values (T, x, y, g_3^2), the system undergoes a phase transition of the first order. In other words, the system transitions from one phase to another, characterized by different physical properties, as it moves along the trajectory.

The intersection of the trajectory with the surface $y = yc(x)$ signifies that the conditions

specified by the values of (T, x, y, g_3^2) correspond to the critical point where the PT occurs. This intersection can have important implications for understanding the behavior of the system at that specific point in the parameter space.

$$\eta_x \equiv \frac{dx}{d\log T}, \qquad \eta_y \equiv \frac{dy}{d\log T}, \qquad \eta_{g_3^2} \equiv \frac{dg_3^2}{d\log T}. \tag{4.4}$$

By examining the evolution of thermodynamics in the 4D theory as it as it advances via the couplings within the 3D EFT, we can assess the rate of movement of this trajectory in the space of 3D couplings. This rate of change can be quantified using the tangent vector, which provides valuable insights into the variations of couplings concerning logarithmic temperature changes ($d\log T$).

To quantify the speed along the trajectory, we can define the components of the tangent vector as η_x, η_x, and $\eta_{g_3^2}$. These components represent the rates of change of the respective couplings x, y, and g_3^2 with respect to the logarithm of temperature.

The quantity η_x represents the rate of change of the coupling x as the logarithm of temperature varies. It tells us how x changes when we move along the trajectory in terms of changes in temperature. Similarly, η_y quantifies the rate of change of the coupling y with respect to logarithmic temperature variations.

Finally, $\eta_{g_3^2}$ represents the rate of change of the coupling g_3^2 as the logarithm of temperature changes. It provides information about how the coupling g_3^2 varies along the trajectory as the temperature parameter evolves.

Considering these components of the tangent vector, we can determine how quickly the path progresses through the parameter domain of 3D couplings in reaction to variations in temperature by considering these components of the tangent vector. These quantities provide insights into the dynamics and behavior of the system, indicating how the var-

ious couplings respond to temperature variations and how the system evolves along the trajectory in the 3D EFT parameter space.

According to the generic structure of dimensional reduction, it is implied that the scaling dimension of coupling x, denoted as η_x, is typically smaller compared to the scaling dimension of coupling y, denoted as η_y. This relationship can be represented as $\eta_x \sim g^2$, while η_y demonstrates an inverse correlation with g and scales as g^{-2}.

In this context, g^2 represents a perturbative coupling, which implies that it is relatively small compared to other couplings in the theory. Perturbative couplings typically arise in theories where interactions can be treated as small corrections to a simpler, non-interacting system.

The relation $\eta_x \sim g^2$ suggests that the scaling dimension of coupling x is influenced by the perturbative coupling g^2, indicating that x may undergo smaller changes under energy scale variations compared to other couplings. On the other hand, the relation $\eta_y \sim g^{-2}$ implies that the scaling dimension of coupling y is inversely proportional to the non-perturbative coupling g raised to the power of -2. This indicates that y is more sensitive to energy scale variations and can undergo larger changes compared to other couplings. Considering these implications, it follows that the trajectory will predominantly move along the y-axis, while the variation of the coupling x will be relatively small. Thus, the trajectory will be almost parallel to the y-axis in the space of 3D couplings for a perturbative 4D model.

To compute the function $yc(x)$, we set a fixed value for x that is less than x, and subsequently adjust the value of y. In this process, we are examining how the coupling y affects the system while keeping the coupling x fixed at a value lower than x.

When examining significantly positive values of y (representative of elevated temperatures), the system manifests a singular phase known as the symmetric phase. In this phase, the system demonstrates specific symmetries, and there is an absence of sponta-

neous symmetry breaking.

For substantially low temperatures, characterized by negative values of y, the system enters a distinct phase known as the broken phase. The symmetry of the system is spontaneously broken, resulting in distinct properties and behavior, in this phase.

In the intermediate range of values for y, there exists a parameter region where both the symmetric and broken phases can coexist simultaneously. This region represents a zone of PT. At the critical temperature, marked by the value $y = yc$, the free energies of the symmetric and broken phases become equal, indicating a phase transition. In other words, both phases are equally probable in the thermal ensemble.

When the two phases coexist, a histogram of a certain observable, such as the quantity $\langle \phi^\dagger \phi \rangle$ (which represents a particular measurement or property of the system), will show two peaks of equal probability. This indicates that the system can exhibit both the characteristics of the symmetric phase and the broken phase simultaneously.

The existence of dual peaks within the histogram serves as an indicator of the simultaneous presence of both phases at the critical temperature. This phenomenon is commonly observed in systems undergoing a phase transition, where the system can transition between two distinct phases depending on the temperature or other parameters.

Within the charts referenced as **Figure 4.1**, the representations portray the mean values of the Higgs quadratic condensate, determined through the employment of the $\overline{\text{MS}}$ methodology within the continuum limit. The double peak pattern indicates different phases and a first-order transition. The upper graph shows how the histogram changes with system size, revealing reduced probability between phases as the system grows. The lower graph demonstrates moderate variation in this quantity with lattice spacing.

To precisely calculate the critical temperature, an effective technique can be employed, utilizing a precise relationship among the probability distributions of $\langle \phi^\dagger \phi \rangle$ at distinct values of y is frequently derived through principles of statistical mechanics or field theory.

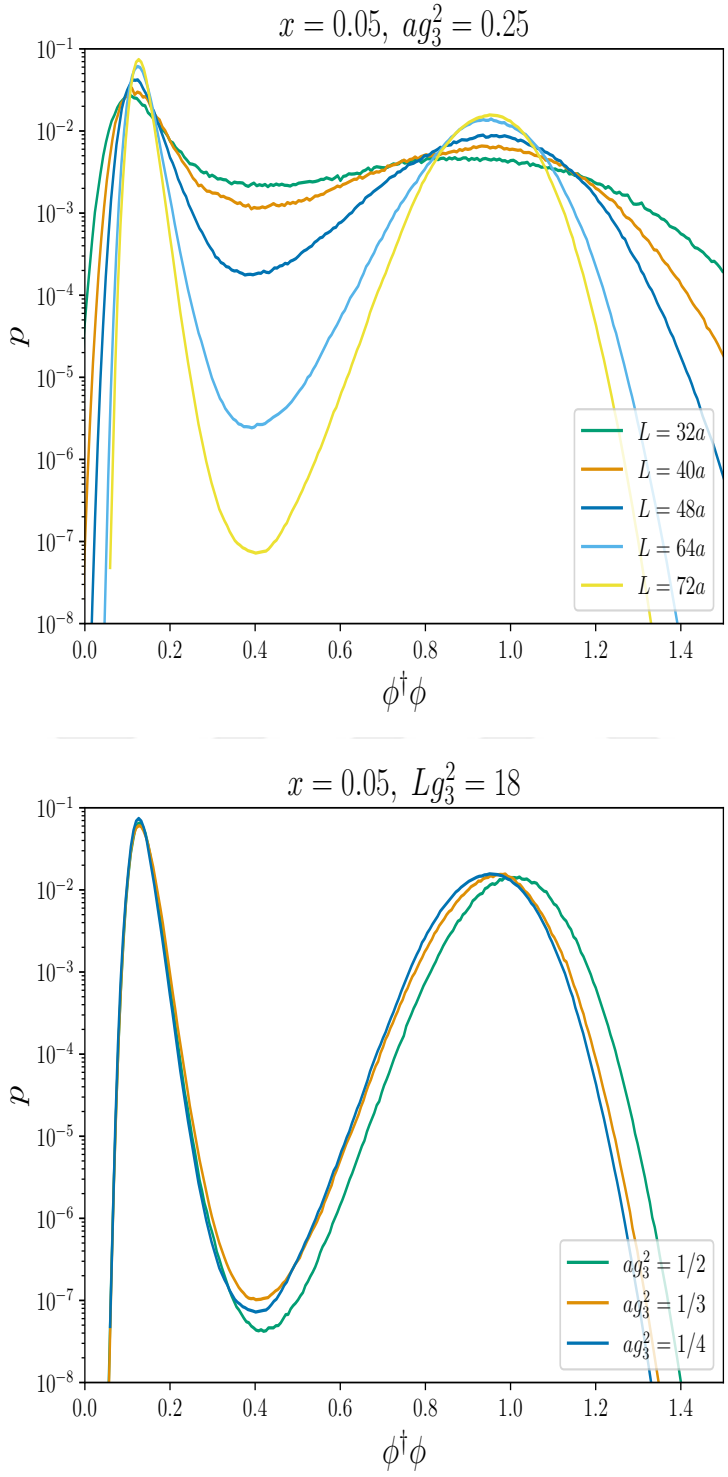


Figure 4.1 The graphs depict the average Higgs quadratic condensate using the $\overline{\text{MS}}$ prescription in the continuum limit, revealing distinct phases and a first-order transition with a double peak pattern, along with reduced inter-phase probability as the system size increases and moderate variation with lattice spacing shown in the upper and lower graphs respectively.

This approach allows for extracting information about the critical temperature from the behavior of the distribution.

Probability distributions of $\langle \phi^\dagger \phi \rangle$ at distinct y values are frequently derived through principles of statistical mechanics or field theory. This relation relates the probability distribution of $\langle \phi^\dagger \phi \rangle$ in the symmetric phase (large positive y), the broken phase (large negative y), and the coexistence region (around the critical temperature, $y = yc$).

By studying this relation and the behavior of the probability distribution, it is possible to identify characteristic features that indicate the critical temperature. One such feature is the presence of two peaks of equal probability in the distribution, which indicates the coexistence of the symmetric and broken phases at the critical temperature.

Efficient calculation methods can be developed to ascertain the temperature that leads to the emergence of the two peaks in the probability distribution and demonstrates equal probabilities. This allows for the determination of the critical temperature without extensive computations or simulations.

By exploiting the exact relation between the probability distributions, this approach provides a more efficient way to estimate the critical temperature and gain insight into the phase transition behavior of the system.

The probability distribution, evaluated at a specific value of $\langle \phi^\dagger \phi \rangle$ can be denoted in Equation 4.5:

$$p_y(\varphi^2) \propto \int \mathscr{D}\phi \mathscr{D}A \; \delta\left(\varphi^2 V - \int_{\mathbf{x}} \phi^\dagger \phi\right) e^{-\int_{\mathbf{x}} L_3}, \tag{4.5}$$

In this expression, $\mathscr{D}\phi$ and $\mathscr{D}A$ represent integration over all possible field configurations ϕ and A, respectively. The symbol δ denotes the Dirac delta function, which enforces the constraint that the integral of $\langle \phi^\dagger \phi \rangle$ over space must equal $\varphi^2 V$. The term V represents

the volume of space, and the integral $\int_{\mathbf{x}}$ denotes integration over space. The Lagrangian density L_3 describes the dynamics of the 3D EFT and determines the behavior of the system. The probability distribution $p_y(\varphi^2)$ gives the likelihood of observing a particular value of φ^2 in the system, considering the statistical ensemble associated with the 3D EFT. It takes into account the field configurations ϕ and A that satisfy the constraint and are consistent with the given value of φ^2. By integrating over all possible field configurations and including the appropriate weight factors, determined by the Lagrangian density, the probability distribution captures the relative likelihood of different values of φ^2. This distribution plays a crucial role in studying the system's behavior, including the characterization of phase transitions, as it provides information about the statistical properties of the field ϕ and its corresponding observable $\phi^\dagger\phi$ at different values of y.

$$p_{y'}(\varphi^2) = e^{-(y'-y)\varphi^2 V} p_y(\varphi^2). \tag{4.6}$$

Equation 4.6 is known as reweighting and allows for the determination of $p_{y'}(\varphi^2)$ at a different value of y', given $p_y(\varphi^2)$ at a reference value of y. By reweighting the results, one can obtain insights into the probability distribution at various values of y without having to perform separate simulations for each y. The idea behind reweighting is to introduce a weight factor, $e^{-(y'-y)\varphi^2 V}$, that accounts for the change in the parameter y. This factor exponentially suppresses or enhances different configurations of $\phi^\dagger\phi$ based on the difference between y' and y, effectively rescaling the probability distribution at the reference value of y. While reweighting offers a powerful approach to explore the probability distribution across varying y values, there are practical limitations. When attempting to reweight the outcomes significantly distant from the reference value, the possibility of encountering an overlap issue emerges. This means that the statistical errors become larger, and the accuracy of the reweighted results diminishes. The overlap problem arises because the importance sampling becomes less efficient as the difference between y' and y increases,

leading to increased uncertainties in the reweighted distribution. In practice, it is important to carefully choose the range of values for y' that can be reliably reweighted from the available simulation data. By considering the extent of overlap and the associated statistical errors, one can determine a suitable range for successful reweighting and obtain meaningful results for various values of y. The histograms presented in **Figure 4.1** have undergone a reweighting process to the critical point. Reweighting involves adjusting the probabilities of various configurations by scaling them based on the difference between the current value of y and the critical value. This rescaling ensures that the probabilities in each phase (represented by the area under each peak) become equal. The reweighting technique enables a more precise estimation of the probability distribution at the critical point.

The boundary between phases can be determined by pinpointing the point of lowest probability in the distribution. While the precise selection of the boundary is not significantly influential, for larger lattices, the value of y_c (the critical point) demonstrates exponential insensitivity to this choice. Therefore, the specific location of the boundary does not significantly impact the determination of the critical point. The behavior of the system is studied on a range of cubic lattices with different volumes and lattice spacings. As the theory is gapped, meaning it has an energy gap separating different energy levels, the volume dependence is exponentially suppressed for sufficiently large volumes. This implies that the system's properties become less sensitive to changes in volume as the volume increases. To investigate the behavior in an infinitely large volume, extrapolations are conducted by averaging the outcomes obtained from the largest lattices utilized in the study. This ensures that the values obtained from different lattice sizes agree within the statistical error. The extrapolation process provides an estimate of the system's properties in the thermodynamic limit, where the volume tends to infinity. After extrapolating to infinite volume, further extrapolations are carried out to zero lattice spacing. Polynomial fits are employed, starting with the lowest-degree polynomial that satisfies a reasonable goodness-of-fit criterion, such as ensuring that the reduced chi-squared value

(χ^2/d.o.f. ~ 1) is close to 1. These extrapolations offer approximations of the system's characteristics within the continuum limit, as the lattice spacing approaches infinitesimal values. The Appendix 1. contains additional details and examples of the continuum extrapolations performed for y_c (the critical point). By employing reweighting, analyzing volume and lattice-spacing dependencies, and performing extrapolations, the study aims to determine the properties of the system at the critical point and in the continuum limit, providing insights into the behavior of the theory. To estimate errors for individual lattices, a jackknife resampling technique was employed. The data was divided into ten blocks, and the jackknife method was utilized to calculate error estimates.

This resampling method helps assess the statistical uncertainties associated with the lattice data. Regarding continuum extrapolations, the errors on the fit parameters are quoted. During the process of applying polynomial fits to extrapolate towards a lattice spacing of zero, the uncertainties linked to the fitting parameters are established. These errors provide an indication of the reliability and accuracy of the extrapolated results in the continuum limit. In the study, a distinct method was employed to calculate the critical temperature. Cylindrical lattices, distinguished by significant dimensional variations, are the central subject of examination in this approach. The lowest point in the probability distribution experiences an increase in width and a decrease in its distinctness as the ratio between the length of the longer and shorter sides of the lattice grows.

The probability distribution exhibits a broad and flattened region primarily characterized by configurations where both phases coexist. The presence of alternative arrangements with increased free energy causes a tension that aligns the boundary perpendicular to the longer axis, as these configurations are energetically less favorable.

At the temperature of utmost significance, the free energy of these arrangements reaches a stage where it ceases to rely on the specific proportion of the fractured phase compared to the symmetrical phase within the lattice. Consequently, the probability associated with these configurations also becomes decoupled from the specific ratio of the broken to sym-

metric phase. This independence arises from the equilibrium state, where identical free energy densities are observed for both phases, and configurations display equal areas of phase boundaries.

Slight deviations from the critical temperature, resulting in changes in the fraction of the broken phase, lead to variations in the free energy. This leads to a non-uniform probability distribution of the order parameter, deviating from a flat distribution.

By employing probability distribution reweighting and adjusting the parameter y until achieving a uniform flatness within the region between phases, the critical temperature can be ascertained through this alternative approach. This approach takes advantage of the unique behavior of cylindrical lattices and the flatness of the probability distribution in the coexistence region, providing an additional means of calculating the critical temperature. A related method, described in Ref. [20], was also employed in the study. This method offers the advantage of not requiring the observation of slow tunnellings between phases, as it solely relies on the knowledge of the probability distribution for mixed configurations.

Nevertheless, one drawback of this method is the necessity to determine the appropriate range where the probability distribution exhibits a plateau, which is not known in advance and must be identified during the analysis process. Despite this difference, the two methods used for calculating the critical temperature, including the one mentioned earlier, yield consistent results within the associated error estimates. Further details and comparisons between the methods can be found in Appendix 13.1.

In **Figure 4.2** illustrates the boundary line indicating first-order PTs and includes the point where the line terminates. The lattice results obtained from this study, as well as references Refs.[21, 22], are plotted alongside two perturbative approximations are plotted. To go beyond using "yc" alone, we represent the renormalization group invariant quantity as $\tilde{y}_c \equiv y_c - \beta_y \log(\mu_3/g_3^2)$. The perturbative results are denoted by green and

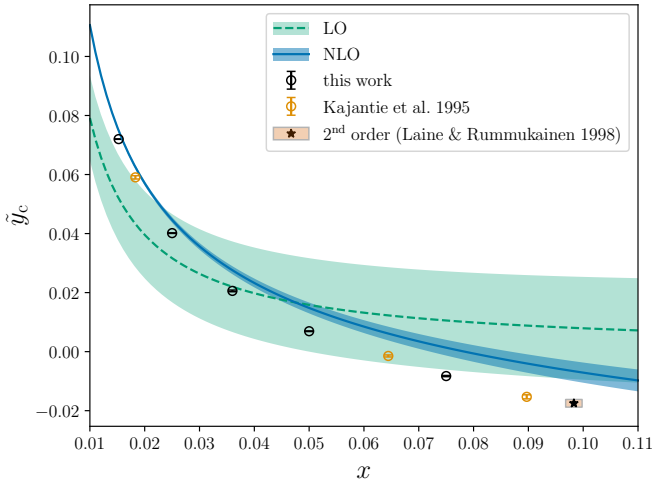


Figure 4.2 Comprarasions of lattice results and perturbative approximations

blue bands, which indicate the variation in the renormalization scale within the range $\mu_3/g_3^2 \in [\frac{1}{2}, 2]$.

The results for the critical point y_c, obtained through continuum extrapolation, are showcased in **Figure 4.2**. The figure also includes relevant findings from earlier studies available in the literature. The data points in the figure are densely distributed in x, allowing for the observation of the smooth behavior of the function $y_c(x)$. This comprehensive dataset provides valuable insights into the relationship between x and y_c.

For specific numerical values of y_c corresponding to different values of x, please refer to **Table 7.1**. The table compiles the collected numerical results for y_c obtained through the continuum extrapolation process. These numerical values offer quantitative information regarding the critical temperature as a function of x.

The combination of the figure and the table provides a clear representation of the continuum-extrapolated results for y_c and their dependence on the parameter x. Despite the presence of Linde's Infrared Problem, it is still possible to calculate the initial terms of an expansion in x. By carrying out a two-loop computation, it becomes feasible to determine the LO and NLO behavior in terms of x.

The two-loop computation involves considering higher-order corrections to the theory,

which can provide insights into the system's behavior beyond the leading order. By incorporating these corrections, a more accurate and refined description of the theory can be obtained, allowing for a better understanding of its properties.

By calculating the LO and NLO terms in the expansion, one can gain valuable information about the system's behavior in different regimes and assess the validity and limitations of the perturbative approach. It is important to note that this expansion provides a partial understanding of the theory and does not fully capture the complete non-perturbative regime affected by Linde's Infrared Problem. The details of the perturbative results can be found in Appendix 13.2. The study does not consider the analysis of a specific type of diagrams that play an essential role in calculating certain advanced aspects within the 3D EFT framework. These infinite diagram sets are significant for calculating higher-order terms in calculations. For more information on higher-order calculations, please refer to Refs. [23, 24].

However, by employing scaling arguments, it is possible to determine the behavior of different types of diagrams in the expansion. Pure gauge diagrams contribute to an expansion in powers of x, while pure Higgs diagrams contribute to an expansion in powers of $x^{3/2}$. As a result, the expansion for the full theory becomes a dual expansion in powers of x and $x^{3/2}$, up to logarithmic terms.

Motivated by these considerations, a fit function based on the expansion in powers of x and $x^{3/2}$, with the inclusion of logarithmic terms, is proposed [25]. This fit function aims to capture the behavior of the theory beyond the available perturbative orders and provides a useful tool for describing the system's properties across a wider range of parameters.

$$yc^{\text{fit}}(x) = \frac{1}{128\pi^2 x}\left[1 + x\left(\frac{63}{2}\log\frac{3}{2} - \frac{33}{4} - \frac{51}{2}\log 8\pi x\right) + c_{3/2}x^{3/2} + c_2 x^2 + c_{5/3}x^{5/2}\right]. \tag{4.7}$$

The fit function for y_c given by Equation 4.7 is used to describe the behavior of the critical temperature as a function of x. By performing a least-squares fit using the lattice data, the coefficients of the expansion are determined:

$$c_{3/2} = 16(6),\ c_2 = -490(60),\ c_{5/2} = 980(150). \tag{4.8}$$

The fit results in a χ^2 per degree of freedom value of 6, indicating a reasonable agreement between the fit function and the lattice data. It is important to acknowledge that the relatively significant expansion coefficients indicate that perturbation theory in x becomes unreliable when x approaches the vicinity of 0.05. This breakdown highlights the limitations of the perturbative approach in this regime.

It's essential to note that while perturbation theory becomes unreliable for higher powers of x, the coefficients $c_{3/2}$, c_2, and $c_{5/2}$ can still be more accurately computed using perturbation theory, in contrast to the coefficients of higher powers of x. This can be achieved through a resummed 3-loop computation. If such a computation is undertaken, there arises a need to revise the way the lattice data is fit. This could involve the inclusion of higher powers of x or the exploration of alternative functional forms that better capture the data's behavior at larger values of x.

5. LATENT HEAT

The critical temperature signifies the juncture where a PT takes place, while the latent heat, quantifies the shift in enthalpy density across the phases involved in this transition. It gauges the energy released or absorbed per unit volume during this transition. The latent heat assumes a pivotal role in grasping the energetic characteristics of PTs.

In cosmological evolution, during a PT, there may be a degree of supercooling that occurs when the temperature drops below the critical temperature before the actual phase transition takes place. This phenomenon is a result of the slow process of bubble nucleation in comparison to the rapid expansion of the universe (Hubble expansion). Consequently, the system has more time to cool down below the critical temperature, resulting in supercooling.

The phenomenon of supercooling can bear notable implications for the dynamics of the phase transition, notably influencing the formation and expansion of bubbles comprising the new phase. The amount of supercooling and the subsequent dynamics depend on various factors, including the nucleation rate, the temperature profile, and the energy barriers involved in the phase transition. Understanding the effects of supercooling is essential for accurately modeling and describing the cosmological evolution during phase transitions. While the latent heat, sets a minimum threshold for the energy released during a phase transition, it does not encompass the extra energy released as a result of the disparity in free energy density, represented by Δf, between the participating phases. The total energy released during the transition is expected to be greater than the latent heat. The dynamic relationship between how rapidly the free energy difference between phases changes and the latent heat becomes particularly significant when evaluating these factors precisely at the critical temperature. It quantifies the energy released per unit volume during the phase transition. The precise value of the latent heat depends on the specific details of the phase transition, such as the nature of the fields involved, the potential energy landscape,

and the underlying dynamics. During cosmological phase transitions, the occurrence of supercooling is possible. In such cases, the latent heat serves as a dependable approximation for minor degrees of supercooling. However, when the supercooling is more pronounced, there is an additional release of energy caused by the liberation of excess free energy accumulated within the system. Precise determination of the latent heat and careful consideration of the effects of supercooling are crucial when investigating cosmological phase transitions. These factors play a crucial role in shaping the formation of structures and the emergence of cosmological perturbations within the universe.

$$\frac{L}{Tc^4} \equiv \frac{d}{d\log T}\left(\frac{\Delta f}{T^4}\right)\Bigg|_{Tc}. \tag{5.1}$$

The application of the chain rule, along with the recognition that $\Delta f = 0$ at the critical temperature, allows for the expression of this relationship in the following way:

$$\frac{L}{Tc^4} = \frac{g_3^6}{T^3}\left(\eta_y \Delta\langle\phi^\dagger\phi\rangle_{\rm c} + \eta_x \Delta\langle(\phi^\dagger\phi)^2\rangle_{\rm c}\right), \tag{5.2}$$

The condensates are expressed in units of g_3^2, where g_3 represents the renormalized coupling constant. The determination of the condensates' descriptions hinges on assessing how the free energy density changes in response to adjustments in the renormalized couplings. The precise expressions and definitions of these condensates in relation to these derivatives can be found in the provided reference [26].

$$\Delta\langle\phi^\dagger\phi\rangle \equiv \frac{1}{g_3^6}\frac{\partial}{\partial y}\left(\frac{\Delta f}{T}\right), \tag{5.3}$$

$$\Delta\langle(\phi^\dagger\phi)^2\rangle \equiv \frac{1}{g_3^6}\frac{\partial}{\partial x}\left(\frac{\Delta f}{T}\right). \tag{5.4}$$

In our analysis, we have rescaled the condensates to be dimensionless by dividing them by appropriate powers of g_3^2. This rescaling allows the condensates to be more directly comparable to measurements obtained from lattice simulations. In the lattice calculations, we adopt units where the coupling constant g_3^2 is set to 1, simplifying the interpretation and analysis of the results. The inclusion of counterterms in the definitions of the condensates ensures their finiteness by accounting for the finite values of the couplings involved. This renormalization process allows for meaningful and well-defined condensate quantities.

In a more detailed perspective, the renormalized quartic condensate comes into existence through a intricate fusion, intricately weaving together the characteristics of both the unrenormalized quartic and quadratic condensates. This complex interplay is underscored by the introduction of a mass counterterm that exhibits a reliance on the parameter x. This integration notably plays a pivotal role in fostering the emergence and development of the quadratic condensate, bringing forth a nuanced interaction within the system.

Notably, it is crucial to highlight that the condensate linked to the partial derivative concerning g_3^2 (with x and y held constant) reaches zero precisely at the critical temperature. This particular condensate is proportional to the difference in free energy densities between the phases, reflecting the equal probabilities of the symmetric and broken phases at the critical point. The significant hierarchy observed between η_y and η_x indicates that the second term in Equation (5.2) can be disregarded. This assumption holds true for relatively weak phase transitions. Nevertheless, in situations where transitions are exceptionally strong, the quartic condensate may surpass the quadratic condensate. Thus, to accommodate such scenarios, our subsequent analysis will encompass both terms to ensure a comprehensive understanding of the system.

In **Figure 5.1** the Higgs condensate undergoes a sudden change at a specific point. However, it is important to mention that this change becomes insignificant at $x_* = 0.0983(15)$, indicated by the vertical band. The outputs from the lattice in this study and from Ref. [21] are displayed.

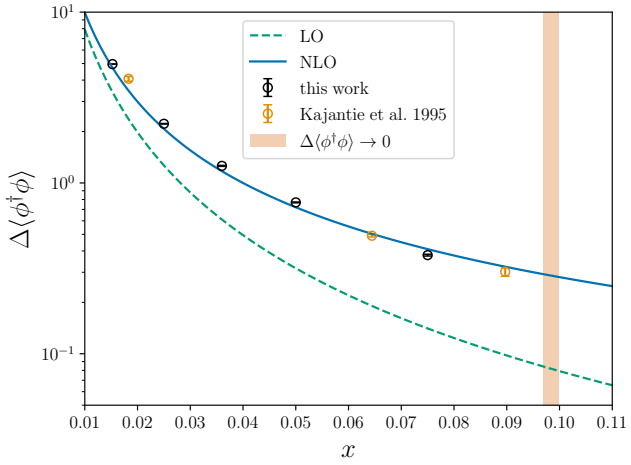


Figure 5.1 The Higgs condensate at $x_* = 0.0983(15)$

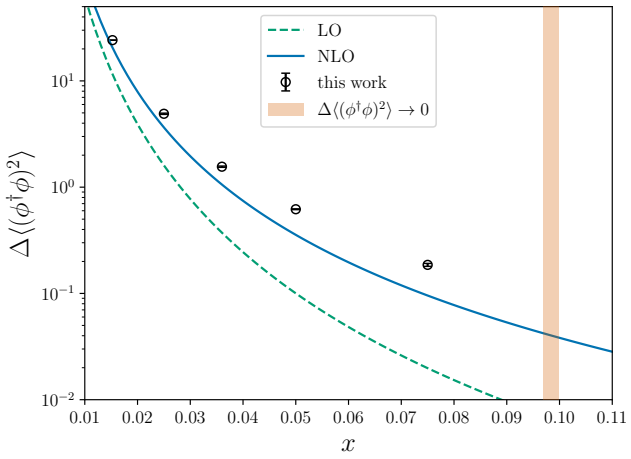


Figure 5.2 The quartic Higgs condensate exhibits a substantial discontinuity.

The continuum-extrapolated results for the quadratic Higgs condensate are shown in **Figure 5.1**, while the extrapolated findings for the quartic Higgs condensate are presented in **Figure 5.2**.

These results are accompanied by previous outcomes reported in the literature. In order to achieve extrapolations to an infinite volume, we employed the identical methodology used for y_c. When considering extrapolations to a vanishing lattice spacing, it is crucial to acknowledge that when incorporating $O(a)$ enhancement in the data, the linear component in the polynomial regression is excluded, as documented in references [27, 28].

In order to eliminate the $O(a)$ corrections, the measurements of the condensates were performed at $y_c(a)$ instead of $y_c(a=0)$. This approach ensures the cancellation of such corrections. Appendix 13.1. contains several examples of our continuum extrapolations, illustrating the evident $O(a)$ improvement achieved in our analysis.

Figure 5.1 and **Figure 5.2** display the LO and NLO representations of the Higgs condensates, respectively, in conjunction with the corresponding lattice data. The perturbative expressions can be found in Appendix 13.2. It is evident that the NLO corrections is clearly observable, as they substantially narrow the gap between the perturbative outcomes and the lattice data. Notably, enhanced consistency is noted between the outcomes derived from lattice simulations and the forecasts originating from perturbation theory in the quadratic condensate. This observation aligns with the fact that the perturbative expansion parameter is smaller for the quadratic condensate.

6. SURFACE TENSION

The surface tension is a fundamental property that characterizes the strength of a phase transition. It quantifies the energy required to create or sustain a boundary between different phases of a substance. At the critical temperature, the surface tension provides valuable insight into the behavior of the system.

When considering PTs, the importance of surface tension becomes evident in comprehending thenucleation of bubbles. The thin wall approximation, often employed in bubble nucleation studies, assumes that the bubble wall thickness is negligible compared to the bubble radius. In this approximation, the energy associated with bubble formation, denoted as E, can be expressed using

$$E = -\frac{4}{3}\pi R^3 p + 4\pi R^2 \sigma. \tag{6.1}$$

In Equation 6.1 the initial expression, $-\frac{4}{3}\pi R^3 p$, denotes the energy linked to the pressure contrast between the bubble's inside and outside. On the other hand, the subsequent expression, $4\pi R^2\sigma$, pertains to the influence originating from the surface tension. When the bubble reaches this critical size, the balance between the pressure and surface energy determines whether it will continue to expand or collapse. Nucleation is the process by which small regions of a different phase (e.g., bubbles in a liquid) form within a parent phase. The rate at which these new regions appear is known as the nucleation rate. The thin wall approximation helps in estimating how frequently these new bubbles are likely to form. The surface tension plays a significant role in determining the stability and dynamics of bubble formation during phase transitions.

Furthermore, the relationship between temperature and surface tension characteristics furnishes valuable insights into the underlying characteristics of the PT. As the critical point of a first-order PT is approached, the surface tension decreases, indicating an increasing tendency for the phases to mix and become miscible. The surface tension can be regarded as a measure of the strength of the transition, with a higher surface tension indicating a more distinct separation between the phases. Surface tension offers insights into the formation of structures, the evolution of the universe, and the generation of cosmological perturbations. In Equation (6.1), the variable p symbolizes the pressure difference or the disparity in free energy density between the homogeneous phases located inside and outside the bubble. The thin wall approximation, which assumes a negligible wall thickness compared to the bubble radius, is applicable in the vicinity of the critical temperature.

The basis for this approximation originates when the bubble size significantly surpasses all additional characteristic scales within the system. Under these conditions, Equation (6.1) accurately describes the energy associated with bubble formation, neglecting corrections of order $O(R)$.

By neglecting these $O(R)$ corrections, the thin wall approximation simplifies the analysis of bubble nucleation, providing a reasonable estimate of the energy involved in the pro-

cess. This approximation holds especially true in the vicinity of the critical temperature, where the size of the bubble emerges as the predominant scale, and other microscopic details of the system can be effectively ignored.

It's essential to recognize that although the thin wall approximation serves as a helpful method for investigating bubble nucleation, it represents a simplification that might overlook certain complexities within the system. For improved precision in scenarios where these intricacies hold importance, it's possible to incorporate higher-order adjustments that account for the finite wall thickness into calculations.

When investigating the system using the 3D EFT approach, it is frequently beneficial to use quantities that have been adjusted based on temperature. This practice simplifies the analysis by eliminating the direct impact of temperature, allowing researchers to focus on the system's fundamental behavior. In this context, the energy of the nucleating bubble per unit temperature, denoted as S_3, becomes a natural quantity of interest. Similarly, The disparity in free energy density between the phases, normalized by temperature and represented as Δf_3, constitutes another pertinent scaled parameter.

By using these temperature-scaled quantities, we can effectively eliminate the explicit dependence on temperature, allowing for a more concise and consistent analysis of the system. This scaling also facilitates comparisons between different temperatures and makes it easier to identify universal features of the phase transition.

Furthermore, when performing calculations on the lattice, it is common practice to scale out powers of the 3D gauge coupling g_3^2. This choice allows for a convenient normalization where the lattice calculations are performed in units where $g_3^2 = 1$. This normalization simplifies the interpretation of lattice results and brings them into closer correspondence with the continuum EFT framework.

By employing these temperature scaling and lattice normalization conventions, one can express physical quantities, such as the energy and free energy density difference, in

dimensionless units that are consistent with the chosen scaling scheme. This approach facilitates the comparison of results obtained from different approaches, such as lattice simulations and EFT calculations, providing a unified framework for analyzing the system in a self-consistent manner the convention where temperature-scaled quantities and units with $g_3^2 = 1$ are used, the dimensionless surface tension is defined as:

$$\sigma_3 \equiv \frac{\sigma}{T g_3^6}. \tag{6.2}$$

This definition allows us to express the surface tension in a dimensionless form that takes into account the temperature scaling and the chosen normalization of the gauge coupling.

By dividing the surface tension σ by the product of the temperature T and the sixth power of the 3D gauge coupling g_3^6, we obtain the dimensionless quantity σ_3. This scaling ensures that σ_3 carries the appropriate dimensions and is consistent with the chosen units for temperature and the gauge coupling.

The use of σ_3 as the dimensionless surface tension facilitates the comparison of results obtained from different calculations, such as lattice simulations and EFT calculations, within a unified framework. It allows us to analyze the strength of the PT in a dimensionless manner, taking into account the interplay between temperature, gauge coupling, and the surface tension.

By expressing the surface tension in terms of σ_3, we can investigate universal properties of the phase transition, independent of specific units or parameter choices, and gain insights into the behavior of the system at different temperatures and gauge couplings. We determine the surface tension through the standard histogram method, as outlined in Binder's work [29]. To obtain accurate results in the infinite volume limit, we take into account the contributions of capillary waves. This is achieved by applying a fitting procedure that has been established and refined in previous studies [30–32].

The histogram method involves constructing probability distributions of the order parameter, which capture the phase transition behavior. These distributions are obtained from Monte Carlo simulations or other numerical techniques. To extract the surface tension, we analyze the shape of these distributions and fit them to appropriate theoretical models. The fitting procedure allows us to disentangle the effects of capillary waves from other contributions, enabling a more accurate determination of the surface tension in the thermodynamic limit.

The inclusion of capillary wave corrections is crucial for obtaining reliable results, as they account for the fluctuations of the interface between phases. By incorporating these corrections, we obtain a more precise estimation of the surface tension, which is essential for studying the strength of the phase transition and its implications for the system's behavior.

By employing the histogram method and considering capillary wave effects through fitting techniques, we are able to determine the surface tension with improved accuracy, enabling a comprehensive understanding of the phase transition dynamics in the system under investigation. The dimensionless surface tension, denoted as σ_3 and scaled by g_3^6, can be determined using the 6.3:

$$\begin{aligned}\sigma_3 \cdot g_3^6 = &\frac{1}{2L_1^2}\log\frac{p_{\max}}{p_{\min}} \\ &+\frac{1}{2L_1^2}\left[\frac{3}{2}\log L_3 - \log L_1 + \text{const}\right].\end{aligned} \tag{6.3}$$

In this equation, $p_{\max}$ denotes the highest value of the order parameter histogram, signifying the probability density associated with the presence of the homogeneous phases. Conversely, $p_{\min}$ pertains to the minimum recorded value in the histogram of the order parameter, which is noticeable in the intermediate zone between phases. This numerical representation signifies the likelihood of coexistence within a hybrid phase characterized by dual interfaces.

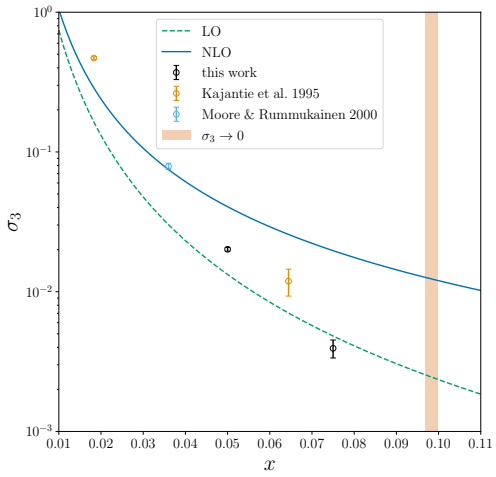


Figure 6.1 The lattice results from the surface tension

The symbols L_1 and L_2 denote the actual dimensions of the lattice in the three spatial axes, with the stipulation that L_1 is equivalent to L_2. Furthermore, L_3 signifies the physical extent of the lattice along the third spatial dimension.

By evaluating the logarithmic ratio of $p_{\max}$ to $p_{\min}$ and incorporating the contributions related to the lattice lengths, the equation allows us to calculate the scaled surface tension σ_3 in units of g_3^6.

This formula provides a practical method for extracting the surface tension from the order parameter histogram, taking into account the lattice dimensions and the probability densities associated with the different phases and interfaces.

Another approach to calculate the surface tension involves examining the Fourier spectrum of transverse fluctuations that transpire at the interface between phases. This technique, initially introduced in Ref.[27] and subsequently utilized in Ref.[32], has been demonstrated to yield more precise outcomes while demanding fewer computational resources. However, since our study primarily focuses on other aspects and not on the precise computation of surface tension, we have not extensively explored this alternative approach.

In **Figure 6.1** the surface tension is plotted as a function of x. It should be noted that the lattice point with the smallest x has not yet undergone the continuum limit. The results from the lattice in this study and from Refs. [21, 32] are displayed.

When measuring the surface tension, it is common to use lattices with one dimension significantly larger than the other two, denoted by $L_3 \gg L_1, L_2$. This choice reduces the interactions between interfaces and facilitates more accurate measurements. Although we have not conducted dedicated simulations on elongated lattices, we have attempted to adapt and utilize the results obtained from our simulations on cubic lattices in Sections 4 and 5.

Due to the limitations of our simulations, which were not conducted in the infinite volume limit, we observed significant deviations from the expected volume dependence described by equation (6.3). This deviation was particularly noticeable for stronger PT for smaller values of x. Consequently, in our results only for $x \geq 0.05$, where the extrapolations to infinite volume appeared to be more reliable. To obtain results at zero lattice spacing, we employed the same extrapolation procedure described in Section 5.

In **Figure 6.1**, we show our results for surface tension, compared with what's known in the literature. Considering both LO and NLO perturbative approximations in our analysis of surface tension, as explained in Appendix 13.2. The difference between lattice and perturbative outcomes for surface tension is clear in **Figure 6.1**.

7. SUMMARY OF EQUILIBRIUM RESULTS

x	y_c	$\Delta\langle\phi^\dagger\phi\rangle_c$	$\Delta\langle(\phi^\dagger\phi)^2\rangle_c$	σ_3
0.0152473	0.071998(79)	4.9635(54)	24.184(44)	—
0.0183	0.05904(56)	4.07(13)	—	[0.47(1)]
0.025	0.04015(10)	2.2207(81)	4.906(64)	—
0.036	0.02058(29)	1.2588(86)	1.558(21)	0.079(4)
0.05	0.00692(11)	0.7692(44)	0.6198(52)	0.02011(62)
0.06444	-0.00146(35)	0.491(8)	—	0.0119(26)
0.075	-0.00827(20)	0.3780(47)	0.1857(59)	0.00393(58)
0.08970	-0.01531(69)	0.302(18)	—	—

Table 7.1 Tle Lattice Monte Carlo Results for equilibrium quantities

In **Table 7.1**, we present lattice Monte Carlo findings for equilibrium properties that describe the first-order EWPT. Furthermore, we incorporate results obtained from relevant references Refs. [21, 32]. It is important to highlight that the result enclosed in square brackets pertains to a single, non-zero lattice spacing and has not undergone extrapolation to the continuum limit.

Perturbation theory, which is based on a systematic expansion in small parameters, generally shows better agreement with lattice results for smaller values of x in our study. As x increases, the deviations between perturbation theory and the lattice become more pronounced. It is important to note that the level of agreement between the two approaches can vary depending on the specific observable being considered.

Surprisingly, the surface tension, a metric indicating the magnitude of the transformation between phases, showcases notable inconsistencies between the predictions derived from lattice calculations and those obtained through perturbation theory. This discrepancy could stem from the intricate interplay of microscopic interactions within the lattice framework, which might not be fully captured by the simplifications inherent in perturbation theory. Consequently, the contrasting results emphasize the complexity of accurately describing the surface tension and its underlying dynamics across different analytical approaches.

This suggests that the surface tension is particularly sensitive to non-perturbative effects and higher-order corrections that are not adequately captured within perturbation theory.

The observed deviations between lattice and perturbation theory results highlight the limitations of perturbative calculations in strongly interacting systems and emphasize the need for non-perturbative techniques to accurately describe and understand the behavior of these systems, especially at larger values of x.

8. BUBBLE NUCLEATION

The formation of bubbles is a crucial factor in the dynamic progression of a PT of the first order. It is the initial step where small regions of the new phase, called bubbles, form and grow within the background phase. The pressure difference between the two phases drives the rapid expansion of these bubbles, leading to their accelerated growth.

While the bubbles persist in their expansion, they ultimately reach a consistent velocity wherein the counteracting frictional influences exerted by the encompassing plasma balance the surrounding bubble pressure. At this point, the bubble growth rate decreases, and they persist in traveling with a constant velocity within the surrounding environment.

The collision of growing bubbles is a significant process during the PT. When bubbles meet, they collide and merge, creating shockwaves and releasing energy in the form of sound waves. These sound waves can play a role in generating gravitational waves, which are distortions in the fabric of spacetime. The generation of gravitational waves in cosmological PTs has undergone thorough investigation [33–35]. Detecting these waves offers a distinct chance to explore the underlying physics of these transitions.

The average distance between nucleated bubbles determines the characteristic scale of the resulting gravitational wave spectrum. Hence, a comprehensive grasp and precise explication of the bubble nucleation process play a pivotal role in generating numerical

predictions concerning the gravitational wave signatures linked with cosmological PTs. By developing a comprehensive understanding of bubble nucleation rates, we can establish a direct connection between observed gravitational waves and the underlying physics of the PT, enabling us to extract valuable information about the early universe.

The estimation of bubble nucleation rate on the lattice involves employing the Langevin dynamics technique. This computational method provides a structured avenue for investigating the characteristics of IR modes within non-Abelian gauge theories under elevated temperature conditions.[36–46]. Specifically, this equations are employed for SU(2) [32, 46]:

$$\sigma_{\rm el}(D_t A_i)^a = -\frac{\delta H}{\delta A_i^a} + \xi_i^a, \tag{8.1}$$

$$\sigma_{\rm el} D_t \phi = -\eta \frac{\delta H}{\delta \phi^\dagger} + \xi_\phi \tag{8.2}$$

$H = \int_{\mathbf{x}} \mathscr{L}3$ establishes the Hamiltonian, and represents the Euclidean Lagrangian. The value of $\sigma_{\rm el} \sim T/\log(1/g)$ corresponds to the color conductivity within the SU(2) context. Furthermore, the noise components ξ_i^a and ξ_ϕ follow the subsequent correlation characteristics:

$$\langle \xi_i^a(t,\mathbf{x}) \xi_j^b(u,\mathbf{y}) \rangle = 2\sigma_{\rm el}\delta_{ij}\delta^{ab}\delta(\mathbf{x}-\mathbf{y})\delta(t-u), \tag{8.3}$$

$$\langle \xi_\phi(t,\mathbf{x}) \xi_\phi^\dagger(u,\mathbf{y}) \rangle = 2\eta\sigma_{\rm el}1\delta(\mathbf{x}-\mathbf{y})\delta(t-u), \tag{8.4}$$

the parameter $\eta \sim 1/g^2$ assumes significance as it characterizes the relative rate at which the evolution of the Higgs field contrasts with that of the gauge bosons. This parameter is instrumental in discerning the dynamic relationship between these fundamental

components within the theoretical framework. Moreover, the notation 1 holds importance as it denotes the identity matrix linked with the foundational SU(2) indices. This identity matrix plays a central role in comprehending the transformations and intricate interconnections that unfold within the realm of SU(2). The Langevin description we employ captures the non-perturbative dynamics of the infrared gauge fields in the symmetric phase, including corrections of order $O(1/\log 1/g)$. Although the initial formulations of the Langevin equations did not explicitly incorporate the critical bubble regime, we hypothesize that the characterization remains applicable in its surrounding region [47]

To provide a more accurate dynamical description, the hard-thermal loop effective theory has been developed [48–55]. This theory incorporates $O(g)$ corrections and numerical schemes have been developed for its implementation [56–60]. Nevertheless, it is important to recognize that the hard-thermal loop effective theory approaches lack a clearly defined continuum limit for this reason it is not chosen to work in this framework.

In terms of cosmological relevance, the nucleation rate holds significance when it is on the order of e^{-100} [61, 62]. In this instance, a deviation of approximately $\pm e^{\pm 1}$ translates to merely a 1% discrepancy in the logarithmic representation of the rate. This underlines the crucial significance of attaining precise outcomes for the bubble nucleation rate. The smallness of the deviation showcases how seemingly minor errors in measurements can wield substantial consequences, particularly when dealing with logarithmic quantities.[47].

Theoretically, one could potentially approximate the rate of bubble nucleation by commencing a lattice within the metastable phase and modeling its progression via the utilization of Langevin equations. By observing the time it takes for the system to transition to the stable phase, one can potentially calculate the nucleation rate [63–67]. it is important to note that bubble nucleation is a process that is exponentially suppressed, with an exponent typically on the order of $O(100)$ for cosmologically relevant scenarios. Calculating the bubble nucleation rate through direct simulations faces a significant challenge

due to the exponential suppression of the process. In a cosmologically relevant scenario, the exponent of the nucleation rate is typically on the order of $O(100)$, indicating an extremely small probability for bubble formation. To understand why direct simulations are unfeasible, consider that the transition from the metastable phase to the stable phase occurs through the formation and growth of critical bubbles. These critical bubbles are rare events and require a significant amount of time to spontaneously form in the system. Since the transition is exponentially suppressed, it would take an unreasonably long simulation time to observe a sufficient number of critical bubbles to accurately determine the nucleation rate.

For example, if the nucleation rate is on the order of e^{-100}, it means that the probability of bubble formation is incredibly small. Running a simulation for a reasonable amount of time would not be sufficient to observe a significant number of bubble nucleation events.

To overcome this challenge, alternative methods and techniques are employed to calculate the bubble nucleation rate indirectly. These methods involve utilizing theoretical frameworks, such as field theory or effective theories, to derive expressions or approximations for the nucleation rate. These approaches take into account the relevant physics and dynamics of the system while avoiding the need for prohibitively long simulations.

By combining theoretical calculations, numerical simulations, and approximations, researchers can obtain reliable estimates for the bubble nucleation rate in cosmological phase transitions, enabling a deeper understanding of the associated physics and its implications for cosmology.

This exponential suppression poses a significant challenge as it would require extremely long simulation times to directly observe bubble nucleation. The timescales involved in the transition are prohibitively large, making such simulations unfeasible for practical purposes. Therefore, alternative methods and techniques are necessary to accurately determine the bubble nucleation rate. In our study, we employ the method introduced in the

papers by Moore and collaborators [32, 68] to calculate the bubble nucleation rate. This method builds upon the pioneering work by Langer [69] but goes beyond the saddlepoint approximation commonly used in earlier approaches.

The key idea is to consider the path integral formulation of the transition rate, which involves summing over all possible field configurations. Instead of relying on the dominant saddlepoint contribution, the method proposed by Moore and colleagues extends the calculation to include fluctuations around the saddlepoint.

Through the inclusion of these fluctuations, this approach offers a heightened precision and dependability in estimating the rate of bubble nucleation. It encompasses crucial non-perturbative influences that can notably affect transition dynamics, particularly when the transition is highly suppressed.

This approach has proven to be successful in various contexts, including the computation of the broken-phase sphaleron rate [70, 71]. It offers a valuable tool for studying cosmological phase transitions and understanding the underlying physics beyond the saddlepoint approximation.

Applying this methodology within our study, our aim is to achieve a more precise determination of the bubble nucleation rate and to gain valuable insights into the nature of the phase transition under investigation. When the process of bubble nucleation proceeds at a significantly sluggish pace, the metastable phase is afforded sufficient duration to attain equilibrium well in advance of nucleation. Consequently, the comparative likelihoods of various field configurations, encompassing bubble arrangements, on the metastable side, can be ascertained based on their corresponding Boltzmann weights. The statistical quandary of determining the likelihood of bubble configurations can be effectively tackled through the application of conventional Monte Carlo techniques.

To obtain the nucleation rate from this probability, additional dynamical information is needed. This encompasses comprehending the frequency with which the dynamic end-

point of a bubble arrangement aligns with the stable phase and delving into the pace at which these bubbles expand. These dynamical quantities can be determined through relatively short Langevin simulations.

Breaking down the simulation of a process that experiences exponential suppression into a statistical component and a dynamical component allows for the tackling of two more manageable problems. The statistical part focuses on determining the probability distribution of bubble configurations, while the dynamical part provides the necessary information about the final state and growth of bubbles.

This factorization allows us to tackle the bubble nucleation problem efficiently and accurately. It combines statistical Monte Carlo techniques with short Langevin simulations to overcome the computational challenges associated with simulating rare events. By addressing the statistical and dynamical aspects separately, we can obtain reliable estimates of the nucleation rate and gain insights into the dynamics of the phase transition.

9. NUCLEATION RATE

The methodology outlined in previous references serves as a fundamental guide for our determination of the nucleation rate [32, 68], where more detailed explanations can be found. A fundamental requirement of this approach is the utilization of a phase-sensitive observable. In our specific context, we choose to utilize the average value of the squared Higgs field, represented as $\langle \phi^\dagger \phi \rangle$, to characterize the situation. The rationale behind adopting this approach lies in the advantageous simplification it provides for reweighting along the y dimension. Reweighting refers to a technique used in statistical analysis to balance or adjust the contribution of different data points based on their relative importance or relevance. By utilizing the $\phi^\dagger \phi$ quantity, we are able to effectively adjust and balance contributions in the y dimension, enhancing the accuracy and meaningfulness of our analysis or calculations.

$p(\phi^\dagger\phi)$, exhibits a distinctive two-peak pattern. The crest observed at lower values of $\phi^\dagger\phi$ corresponds to the symmetric phase, whereas the crest at higher values aligns with the broken phase. This distinction is evident in **Figure 4.1**, where histograms of $\phi^\dagger\phi$ are graphically depicted.

It is important to note that a classical real-time trajectory between the phases must traverse intermediate values of $\phi^\dagger\phi$. The probability of these intermediate values occurring in the equilibrium distribution is exponentially small. Therefore, by studying the distribution of $\phi^\dagger\phi$ and the rare events associated with transitions between the two phases, we can extract valuable information about the nucleation rate.

The phase-sensitive observable, $\phi^\dagger\phi$, serves as a key ingredient in our analysis. By examining the distribution of this observable and considering the dynamics of its evolution, we can gain insights into the nucleation process and accurately compute the nucleation rate. On a lattice of appropriate size, as demonstrated in Refs. [32, 68], the probability distribution $p(\phi^\dagger\phi)$ exhibits a minimum between the two phases. This minimum corresponds to spatially localized structures known as "critical bubbles." These critical bubbles play a crucial role as gatekeepers between the symmetric and broken phases.

The critical bubbles represent the most probable configuration that bridges the two phases. They are localized in space and serve as the key transition states during the nucleation process. By identifying and studying these critical bubbles, we can gain insights into the underlying physics of the phase transition and extract information about the nucleation rate.

It is worth noting that the lattice size must be chosen appropriately to ensure accurate characterization of the critical bubbles. The lattice should be large enough that the volume fraction occupied by the bubble is less than approximately $4\pi/81 \approx 15$. This criterion ensures that the critical bubble is properly resolved on the lattice. Furthermore, it is imperative that the lattice dimensions remain appreciably reduced compared to the typical

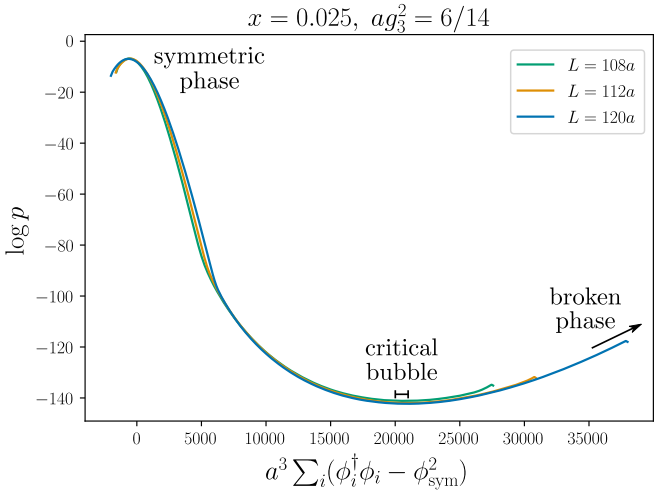


Figure 9.1 The Probability distribution of phases and critical bubble

gap between nucleating bubbles within an infinite volume. Nevertheless, in practical terms, given the exponential suppression of bubble configurations, this criterion carries limited importance, as it leads to an exponentially significant average gap between the emerging bubbles.

By carefully analyzing the properties and dynamics of these critical bubbles, we can gain valuable insights into the nucleation process and accurately determine the nucleation rate for the phase transition under investigation.

The presence of critical bubbles significantly affects the nucleation process, as they are associated with the point in the probability distribution $p(\phi^\dagger\phi)$ where the value reaches its lowest point. This crucial position is denoted as φ_C^2. The minimum value functions as a threshold that distinguishes the two phases and establishes the vital surface or separating boundary, which represents a co-dimension one surface within the configuration space.

In **Figure 9.1**, the graphs display the likelihood of various values for the quadratic Higgs condensate integrated over the entire volume. These values are contrasted with their equivalents in the symmetric phase. We chose to use this representation rather than the quadratic Higgs condensate averaged across the volume due to the consistent size of the critical bubble. [47]. Consequently, the position of the critical bubble on the graph re-

mains unchanged, irrespective of shifts in lattice sizes. As long as the critical bubble occupies a volume fraction of roughly $\lesssim 4\pi/81$, the likelihood of the critical bubble compared to the symmetric phase remains consistent. This stability governs the statistical aspect of the nucleation rate, holding true even when the lattice size denoted by L varies [32].

$$P\left(|\phi^\dagger\phi - \varphi_C^2| < \varepsilon/2\right) = \int_{\varphi_C^2-\varepsilon/2}^{\varphi_C^2+\varepsilon/2} p(\phi^\dagger\phi)d(\phi^\dagger\phi), \tag{9.1}$$

$$\approx p(\varphi_C^2)\varepsilon. \tag{9.2}$$

To quantify the probability of being in the vicinity of the critical surface, we consider a small interval ε around φ_C^2. The probability P of being within this interval can be expressed as an integral of the probability distribution $p(\phi^\dagger\phi)$ over the interval. Approximating this integral, we find that P is approximately equal to $p(\varphi_C^2)$ multiplied by the width of the interval ε. to the probability of the metastable phase

Figure 9.1 provides example of histograms illustrating the probability distribution. $|\phi^\dagger\phi - \varphi_C^2| < \varepsilon/2$ is defined in the plot and referred to as the "critical bubble" region. Analysis is conducted to explore the temporal development of the scalar condensate in near the critical bubble. Two scenarios of the time evolution, denoted by light and dark blue lines, are depicted. Both occurrences start with the exact same initial bubble arrangement during the update step 0. The green shaded region visually highlights the portion of the graph where the condition $|\phi^\dagger\phi - \varphi_C^2| < \varepsilon/2$ is met, indicating a state of being near the critical bubble. The horizontal black lines signify the termination points of the simulation, marking the bubble's expansion or contraction towards the homogeneous phases.To access a visual representation of a trajectory similar to the one described, please refer to the provided reference for a 3D video demonstration Ref. [72].

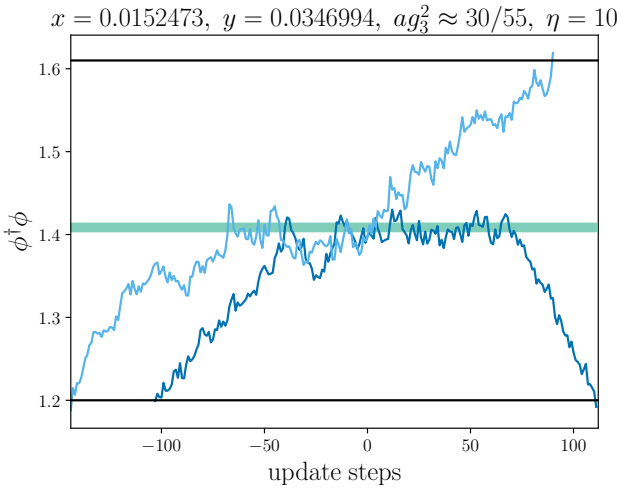


Figure 9.2 Bubble configuration update steps and crossings

To compute the flow of probability across the critical surface in configuration space, it's necessary to multiply the probability density at the critical bubble, represented as $p(\varphi_C^2)$, with the perpendicular vector's magnitude. This vector is denoted as $\left|\Delta(\phi^\dagger\phi)/\Delta t\right| \varphi C^2$. This quantity captures the rate of change of the field configuration near the critical surface.

To accurately calculate the nucleation rate, it is crucial to acknowledge that trajectories can intersect the critical surface multiple times, and not all of these intersections correspond to actual tunneling events. Some trajectories may cross an even number of times, indicating no tunneling. This effect is taken into account by introducing a dynamical prefactor denoted as **d**.

The dynamical prefactor is given by Equation 9.3:

$$\mathbf{d} = \frac{\delta_{\text{tunnel}}}{N_{\text{crossings}}}, \tag{9.3}$$

where δ_{tunnel} takes a value of 1 if tunneling occurs and 0 otherwise, and $N_{\text{crossings}}$ represents the number of crossings of the critical surface.

The prefactor **d** ranges between 0 and 1, with $\mathbf{d} = 1$ indicating that tunneling occurs and $\mathbf{d} = 0$ indicating no tunneling. Assuming equal probabilities for the expansion or con-

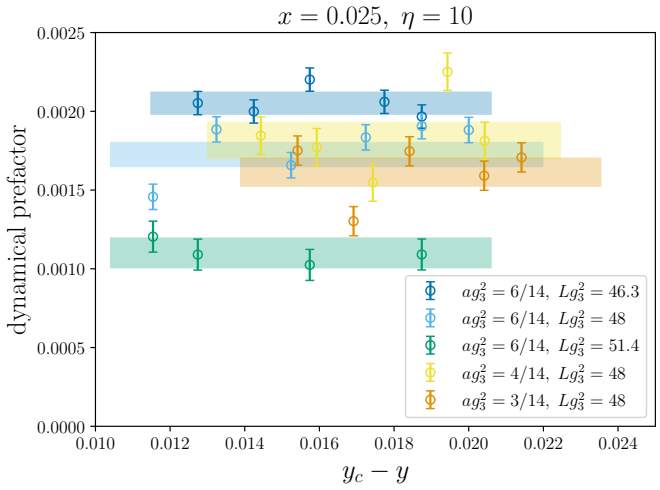


Figure 9.3 The nucleation rate's dynamical prefactor.

traction of all critical bubbles between the broken and symmetric phases, and considering that they only intersect the critical surface once or twice, the average value of the vector **d** would be $\langle \mathbf{d} \rangle = 1/2$. Owing to the erratic and fluctuating nature of the Langevin evolution, which can exhibit abrupt variations, it is anticipated that the average value of the vector **d**, denoted as $\langle \mathbf{d} \rangle$, would be less than 1/2. This behavior is illustrated in **Figure 9.2**, which shows example trajectories exhibiting multiple crossings of the separatrix.

The value of **d** increases as the trajectory is downsampled, meaning that smaller time intervals between samples result in a higher probability of tunneling. The decrease in the magnitude of $\left|\Delta(\phi^\dagger\phi)/\Delta t\right| \varphi^2 \mathrm{C}$ counterbalances the increase observed in **d**, which represents the rate of change of the field variable $\phi^\dagger\phi$ at the critical bubble location. The outcome of multiplying **d** with $\left|\Delta(\phi^\dagger\phi)/\Delta t\right| \varphi^2 \mathrm{C}$ remains constant, irrespective of the chosen sampling rate. This safeguards the accuracy of the nucleation rate calculation from being influenced by the specific intervals at which samples are taken. This compensation between **d** and the rate of change term is discussed in Ref. [32].

In summary, the rate at which nucleation occurs within a given volume is influenced by two fundamental components when calculated on the lattice; the dynamical factor and the statistical factor. The expression for the nucleation rate, as given in Refs. [32, 68], is:

$$\tilde{\Gamma} = \underbrace{\left\langle \frac{\mathbf{d}}{2} \left| \frac{\Delta(\phi^\dagger \phi)}{\Delta t} \right|_{\varphi_C^2} \right\rangle}_{\text{dynamical}} \underbrace{\frac{P\left(|\phi^\dagger \phi - \varphi_C^2| < \varepsilon/2\right)}{\varepsilon V P\left(\phi^\dagger \phi < \varphi_C^2\right)}}_{\text{statistical}}. \tag{9.4}$$

The dynamical factor involves the average of $\frac{\mathbf{d}}{2}\left|\frac{\Delta(\phi^\dagger\phi)}{\Delta t}\right|\varphi^2\mathrm{C}$, where $\mathbf{d}$ accounts for the effect of multiple crossings of the separatrix and $\left|\frac{\Delta(\phi^\dagger\phi)}{\Delta t}\right|\varphi^2\mathrm{C}$ represents the rate of change of the field variable at the critical bubble location.

The statistical factor captures the relative probabilities associated with the critical bubble and the metastable phase. The definition involves calculating the proportion of the probability within a close range of the critical surface, denoted as $P\left(|\phi^\dagger\phi - \varphi_C^2| < \varepsilon/2\right)$, relative to the product of ε, the volume V, and the probability of being in the metastable phase, expressed as $P\left(\phi^\dagger\phi < \varphi_C^2\right)$.

By combining these factors, the expression in Equation 9.4 furnishes a numerical assessment of the rate at which nucleation occurs within a given volume on the lattice.

The calculation of the nucleation rate involves both statistical and dynamical aspects. The statistical part can be determined using standard Monte Carlo simulations, particularly multicanonical Monte Carlo simulations, which can efficiently sample the probability distribution and provide the necessary information for the statistical factor in Equation 9.4.

On the other hand, the dynamical part of the nucleation rate requires real-time Langevin simulations. By evolving the system according to Langevin dynamics, one can extract the relevant dynamical quantities, such as the rate of change of the field variable at the critical bubble location. This information is crucial for calculating the dynamical factor in Equation 9.4.

The factor of 1/2 in the dynamical part accounts for overcounting in the nucleation pro-

cess. The source of this can be attributed to the fact that roughly half of the changes between the phases take place in the opposite direction and do not contribute to the rate at which nucleation occurs. Therefore, to avoid double-counting, the factor of 1/2 is introduced in the expression.

By combining the statistical and dynamical factors, the nucleation rate per unit volume can be accurately estimated, providing insights into the dynamics of phase transitions and the probability of bubble nucleation in the system of interest. Compared to a ”wait-and-see” approach, where one directly observes the decay of the metastable phase, the method described in Refs [63–67], Equation 9.4 provides a more efficient and tractable way to estimate the nucleation rate. By factorizing the rate and utilizing equilibrium and Langevin simulations, it allows for a systematic calculation of the nucleation rate even in systems where direct observation of nucleation events is computationally impractical due to their exponentially suppressed nature. Certainly, breaking down the nucleation rate into its dynamic and statistical aspects assumes that time-based connections can be ignored during most of the nucleation process, except for a short period near the critical bubble, as the transition occurs between the symmetric phase and the critical bubble.

Explicit demonstration of the factorization can be achieved by employing a saddle-point approximation of the path integral, as shown in the work of Langer [69] and more recent studies [73, 74]. However, it’s important to note that the lattice simulations used in the present approach go beyond the saddlepoint approximation.

Lattice simulations provide a non-perturbative and numerical method to study the dynamics of the system, including the nucleation process. By simulating the system on a lattice and using Langevin dynamics, one can capture the effects of fluctuations and interactions that are not accounted for in the saddlepoint approximation. This allows for a more accurate description of the nucleation process and a quantitative determination of the nucleation rate.

While the factorization assumption is crucial for the approach described in Equation 9.4, it is important to recognize that lattice simulations provide a more comprehensive treatment that incorporates the full dynamics of the system, beyond the saddlepoint approximation. In the numerical simulation of the Langevin equations, such as Equations (8.1) and (8.2), there are considerations regarding the discretization of the time derivative and the choice of update algorithm to ensure accurate and reliable results.

One potential strategy involves discretizing the time derivative and simulating the system as a stochastic initial value problem. However, it is of utmost importance to acknowledge that this method introduces errors due to finite time steps, which may result in deviations from the true thermodynamics of the system. These deviations become particularly pronounced in the presence of finely balanced critical bubbles. Consequently, they can impact the overall accuracy of the simulation and influence the dynamics of the nucleation process.

An alternative approach is to use a different dissipative update algorithm that is known to be equivalent to Langevin evolution. In the case described in Ref. [32], heatbath updates are chosen for the gauge fields. Heatbath updates are a type of Monte Carlo algorithm that ensures the correct equilibrium distribution of the gauge fields.The decision to employ this update algorithm is intended to mimic the behavior of Langevin dynamics. In this imitation, the duration of each time step, denoted as Δt, is determined by the number of iterations involving heatbath updates for each link, represented as n_{hb} in accordance with the equation provided.

$$\Delta t = \frac{1}{4} n_{\mathrm{hb}} \sigma_{\mathrm{el}} a^2. \tag{9.5}$$

By using heatbath updates, the simulation can achieve the desired Langevin dynamics while avoiding some of the issues associated with finite time step errors. It provides a reliable and efficient way to evolve the system and capture the relevant physics, including the nucleation process and the statistical and dynamical factors that determine the nucle-

ation rate. In the simulation of lattice systems using heatbath updates, the order in which lattice sites are updated can affect the dynamics and properties of the system. While a random order of updates has been proven [45] to ensure the correct equilibrium distribution, in your case, you have chosen a checkerboard order for simplicity and parallelization.

The use of a checkerboard order means that the lattice sites are updated in a sequential and alternating fashion, where odd and even sites are updated separately. This choice simplifies the implementation and allows for efficient parallelization of the simulation. While deviating from a fully random order, this departure introduces limited correlations between neighboring sites. However, this choice is partially justified by the uncorrelated nature of updates within each group of odd or even sites.

By employing a randomized selection process, alternating between updating odd and even sites during each sweep of the lattice, one can introduce some element of randomness into the update process. This random selection helps mitigate any potential biases or artifacts that may arise from using a fixed order for the updates.

Overall, while the checkerboard order deviates from a fully random order, it is a practical choice that balances simplicity, efficiency, and parallelization capabilities. It allows for the simulation to capture the essential physics of the system and provide reliable results for the nucleation process and the determination of the nucleation rate.

It is important to ensure that the evolution of the Higgs field reaches equilibrium with the gauge fields. To achieve equilibrium, selecting the right update parameters becomes crucial as the advancement of the Higgs field outpaces that of the gauge fields in a parametric manner.

To address this issue, a considerable number of heatbath and overrelaxation updates, typically denoted by $\eta \gg 1$, are carried out on the Higgs field for each individual update. This ensures that, especially when examining the dominant interactions, the gauge field registers the Higgs field as being in a state of balance or stability. In other words, the equi-

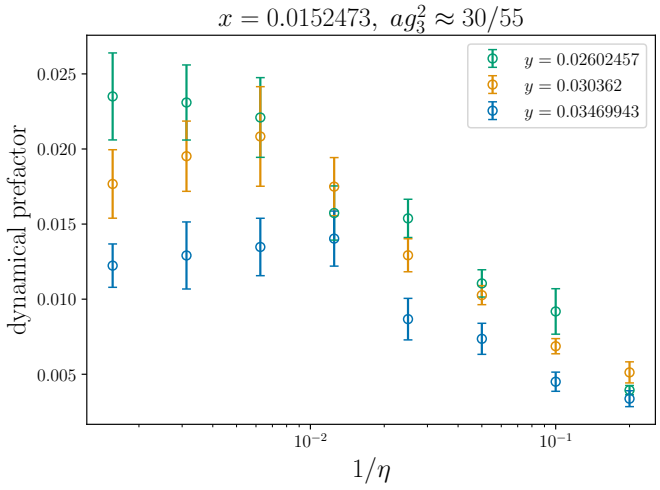


Figure 9.4 Dynamical prefactor behaviour with changing Higgs field updates

librium between the two fields is established, particularly when considering their most significant couplings or interactions.

In **Figure 9.4**, we present the variation of the dynamical prefactor as a function of η for a specific value of x. The plotted data illustrates that the prefactor shows an initial increase as the values of η rise, followed by a plateau indicating a gradual convergence towards a limit as η approaches infinity. This observation indicates that a sufficiently large value of η can capture the leading-order behavior, as shown in previous studies [45].

In practice, two specific values of η are used in the simulations, namely $\eta = 10$ or $\eta = 40$, as mentioned in the paper [75]. This decision is driven by the observation that the discrepancy arising from the use of these values is similar in magnitude to the uncertainty linked with the statistical component of the nucleation rate. Therefore, these values provide a reasonable compromise between computational efficiency and accuracy.

By using either $\eta = 10$ or $\eta = 40$, the simulations capture the essential dynamics and allow for the calculation of the nucleation rate. The error introduced by this choice is considered to be within an acceptable range, considering the uncertainties associated with other factors in the calculation.

By employing the reweighting method described in Equation 4.6, the influence of the

variable y on the statistical element of the rate at which nucleation occurs can be effectively ascertained. This approach facilitates a notable reduction in the effort needed for the simulation. By conducting a single simulation for a particular y value, the complete functional relationship with respect to y can be acquired.

However, the nucleation rate's dynamic nature currently lacks an equivalent approach. Therefore, to investigate the y dependence of the dynamical portion, simulations are carried out. As shown in Figure **Figure 9.3**, several instances of these simulations illustrate the dynamic prefactor's behavior concerning y. It is observed that the y dependence is quite mild, showing consistency with being constant within the given error bars.

This result indicates that the dynamical prefactor does not exhibit significant variations as y is varied. Consequently, the y dependence of the nucleation rate is primarily governed by the statistical part, which can be accurately determined through reweighting techniques. The mild y dependence of the dynamical part further simplifies the calculation and allows for more efficient computations. The variability of the dynamic component of the nucleation rate with respect to the variable y has been investigated using direct simulations, which have demonstrated its gentle nature and alignment with being approximately constant within the margins of error. This finding confirms that the dominance of the statistical component in influencing the variation of the nucleation rate with respect to the variable y. Consequently, reweighting techniques can be effectively employed to accurately determine this dependence. The analysis of **Figure 9.3** indicates that there is some volume dependence in the dynamical part of the nucleation rate. However, once the volume dependence is integrated into the complete nucleation rate, the overall influence of volume becomes less pronounced, exhibiting a gentle trend and aligning with the assumption of volume independence within the provided error margins.

The volume dependence of the dynamical part can be attributed to the finite size of ε used in the calculation. As the system's volume expands, the probability distribution for $\phi^\dagger\phi$ reveals a more pronounced curvature at its lowest point. This leads to the outcome

that bubbles positioned at the edges of the defined range, where the condition $|\phi^\dagger\phi - \varphi_C^2| < \varepsilon/2$ is satisfied, hold greater significance in the process of computing the dynamical prefactor. In other words, the contribution of these bubbles becomes more prominent in influencing the determination of the dynamical factor in the overall calculation.

Nonetheless, bubbles located at the boundaries of this designated range are comparatively less prone to experience tunneling, which involves the passage of quantum particles through energy barriers. This reduced tendency to tunnel leads to a lower value of the parameter **d** for these particular bubbles. In essence, these bubbles contribute less to the overall parameter due to their decreased likelihood of undergoing the tunneling process. Conversely, the cumulative probability $P\left(|\phi^\dagger\phi - \varphi_C^2| < \varepsilon/2\right)$ increases due to the elevated probability density at the boundaries of the range. Consequently, the statistical component of the nucleation rate experiences an augmentation.

These two effects, the decrease in the dynamical part and the increase in the statistical part, tend to cancel each other out, as explained in the appendix of Ref. [32]. As a result, the total volume dependence of the nucleation rate becomes milder and consistent with being independent of volume within the given errors.

Therefore, while there is some volume dependence in the dynamical part of the nucleation rate due to the finite size of ε, it is counteracted by the corresponding volume dependence in the statistical part. This cancellation of effects ensures that the overall volume dependence of the nucleation rate is reduced and remains within the expected range of statistical uncertainties. The connection between the physical nucleation rate Γ and its counterpart $\tilde{\Gamma}$ computed on the lattice can be established through the following equation:

$$\Gamma = \frac{g_3^4}{\sigma_{\mathrm{el}}} \cdot (g_3^2)^3 \cdot \tilde{\Gamma}(x,y). \tag{9.6}$$

The coefficients found on the right side of Equation (9.6) carry significant physical meanings and arise from the alignment between the units used in the simulation on the lattice

and the corresponding physical units. This correspondence between the lattice units and physical units provides a meaningful context for the coefficients' emergence. These coefficients encapsulate fundamental characteristics of the low-frequency gauge configurations that are pertinent to the phenomenon of bubble nucleation.

$\frac{g_3^4}{\sigma_{\text{el}}}$, corresponds to the converse time scale associated with the development of the infrared gauge configurations. It incorporates the coupling constant g_3, raised to the power of 4, which determines the strength of the interactions. The denominator σ_{el} corresponds to the elastic string tension, which is related to the energy cost of creating a localized region of broken symmetry. This factor captures the dynamical aspects of the nucleation process.

The second factor, $(g_3^2)^3$, represents the inverse volume scale of the infrared gauge configurations. It incorporates the coupling constant g_3, raised to the power of 2, which determines the strength of the interactions. This factor reflects the spatial extent of the gauge configurations and their contribution to the nucleation process.

Together, these prefactors in Equation (9.6) relate the lattice calculations of the nucleation rate to the physical nucleation rate by accounting for the relevant time and volume scales in the system.

The prefactors given by Equation (9.6) emerge from the correspondence between physical units and the units employed in lattice calculations [45]. The first prefactor, $\frac{g_3^4}{\sigma_{\text{el}}}$, corresponds to the inverse time scale of the gauge field evolution and is determined by the coupling constant g_3 and the elastic string tension σ_{el}. The second prefactor, $(g_3^2)^3$, captures the inverse volume scale and signifies the characteristics of typical infrared gauge configurations that are pertinent to bubble nucleation.

Finite volume effects become exponentially small as the lattice size increases. This is a consequence of the model being gapped, meaning there is a finite energy barrier separating the two phases. To avoid interactions with itself through periodic boundary conditions, the bubble must fit inside the lattice with sufficient empty space around it. In

Refs. [32, 68], it is shown that this condition is approximately satisfied when the volume occupied by the bubble is less than approximately $\pi^2/81$ of the total lattice volume. This ensures that the finite size of the lattice does not significantly affect the nucleation process and allows for accurate calculations of the nucleation rate.

In smaller lattices, the lowest energy configuration for the bubble may deviate from a perfect spherical shape and exhibit distortions such as cylindrical or slab-like geometries. These alternative configurations arise due to the finite size of the lattice and the presence of discrete lattice sites. The histograms of relevant observables may exhibit kinks as a consequence of transitioning between these diverse geometrical configurations.

Moreover, there exists another discernible kink in the histograms that corresponds to the shift from bulk fluctuations to localized bubble fluctuations. This transition occurs when the system undergoes a significant change in its behavior, transitioning from a regime dominated by bulk fluctuations to one where localized bubble-like structures become energetically favorable.

These kinks and transitions have been studied in the context of lattice simulations of bubble nucleation and are discussed in references such as [32, 68, 76–78]. They provide insights into the behavior of the system at different length scales and the influence of finite size effects on the nucleation process.

Figure 9.5 displays the nucleation rate for a particular value of x across a variety of lattices, accompanied by the continuum extrapolation. The results for other values of x and their continuum extrapolations are presented in Appendix 13.1. The selection of lattice sizes was deliberate to ensure that they were sufficiently large to accommodate spherical bubbles, thereby minimizing the impact of finite volume effects. In the case of the smallest lattice spacings, multiple lattice volumes are shown, and their results are consistent within the given error bars, further confirming the absence of significant volume dependence.

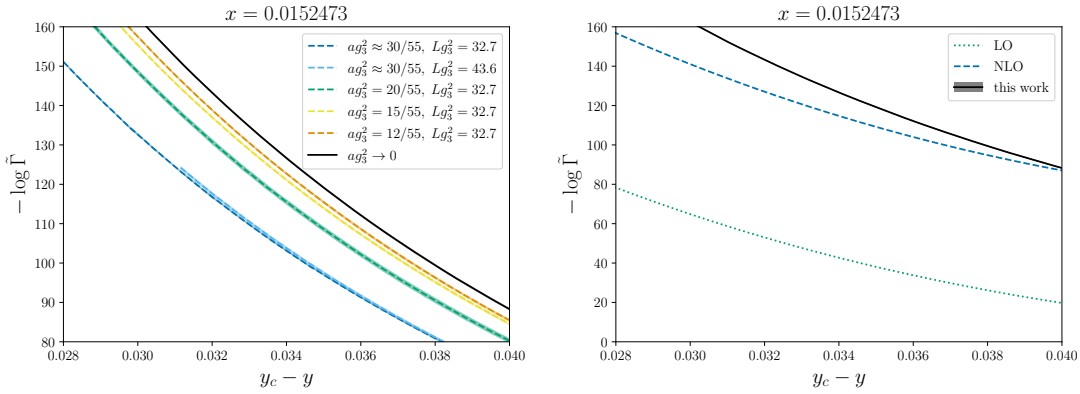


Figure 9.5 On left, we display data obtained from finite lattices along with the extrapolation to the continuum. On right, we compare the extrapolated rate with two perturbative approximations.

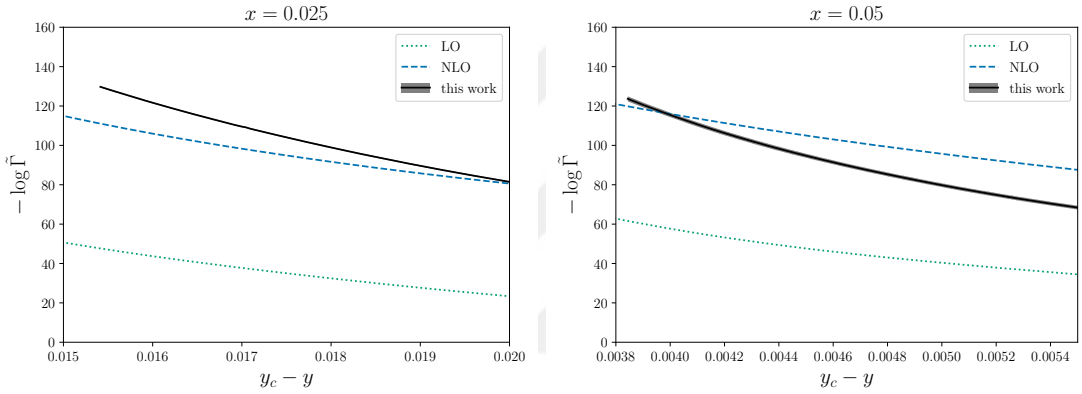


Figure 9.6 The bubble nucleation rate for two less pronounced transitions studied is shown, along with two perturbative approximations.

To provide a comprehensive overview of the nucleation calculations, **Table 9.1** presents a comprehensive collection of parameters and lattice volumes employed in the computation of the nucleation rate. This information helps to establish the range of lattice spacings and volumes considered in the study.

Diverse lattice simulations were conducted to study bubble nucleation, with a comprehensive list of runs available at [75]. Notably, larger lattices were used for higher x values due to the importance of critical bubbles for cosmological concerns where $-\log\tilde{\Gamma} \sim 100$, as they approach the thin-wall limit due to low surface tension. All simulation volumes were sufficiently large to ensure the bubble occupies a small volume fraction, $(\varphi_C^2 - \varphi_S^2)/(\varphi_B^2 - \varphi_S^2) \lesssim 4\pi/81$, preventing bubble self-interaction [32], where φ_S^2 and φ_B^2

x	ag_3^2	volumesa^3
0.0152473	0.5455087	60^3, 80^3
	0.3636364	90^3
	0.2727273	120^3
	0.2181818	150^3
0.025	0.4285714	108^3, 112^3, 120^3
	0.2857143	168^3
	0.2142857	224^3
0.05	0.5	168^3
	0.3333333	224^3

Table 9.1 Bubble Nucleation results for x values and volumes

mark peaks of the phases respectively.

To conveniently analyze and interpret the numerical results, a fitting procedure is applied using the following function:

$$\mathscr{A}(x,y) = \frac{s_{-2}}{(yc-y)^2} + \frac{s_{-1}}{yc-y} + s_0. \tag{9.7}$$

The fitting procedure is carried out for each specific value of x that falls into the interval of $yc-y$, as illustrated in **Figure 9.5** and **Figure 9.6**.

The motivation behind this function arises from the anticipated behavior in the thin-wall limit, where $(yc-y)$ approaches zero from the positive side. In the thin-wall limit where $(yc-y)$ approaches zero, the action exhibits the following growth behavior:

$$\mathscr{A}(x,y) \to \frac{16\pi\sigma_3^3}{3(\Delta\langle\phi^\dagger\phi\rangle_c)^2(yc-y)^2}, \tag{9.8}$$

Here, σ_3 represents the surface tension and $\Delta\langle\phi^\dagger\phi\rangle_c$ denotes the increase in the squared condensate, at $y = yc$.

x_c	s_{-2}	s_{-1}	s_0
0.0152473	0.0506(66)	5.93(40)	-91.9(6.0)
0.025	0.01419(48)	1.612(56)	-35.0(1.6)
0.036^*	0.0061(30)	0.15(64)	-1(34)
0.05^*	0.001410(99)	0.081(40)	7.2(4.5)

Table 9.2 Lattice Monte Carlo Results

It should be noted that the fitting process is conducted within a specific range of nonzero values for $yc - y$, instead of being limited to the $y \to yc$ scenario. As a result, the obtained fit results s_i should not be interpreted as coefficients for an expansion centered around $y = yc$, but rather as parameters that capture the observed behavior across the studied range of y.

The obtained fit results, namely the values of s_i, are summarized in **Table 9.2**. Here lwe showcase lattice Monte Carlo outcomes employed for fitting the bubble nucleation rate. These results are juxtaposed with data obtained from Ref. [32]. Notably, the reported errors for $x = 0.036$ are relatively large due to the assumption of ± 1 errors on the rate. It is important to bear in mind the asterisks $(^*)$, which indicate that the extrapolation to $a \to 0$ has only been conducted using two lattice spacings for these specific values of x.

For the nucleation rate, constructing a perturbative expansion demands careful consideration. In our investigation, we embrace the Effective Field Theory (EFT) approach for bubble nucleation [73], ensuring both gauge and renormalization-scale invariance by methodically expanding in x [73, 79, 80]. More detailed information can be found in Appendix 13.2. When progressing beyond the LO to higher orders, the variations in the yc values among consecutive subsequent levels of approximation create complexities for a direct expansion. This is attributed to the non-analytic nature of the rate at yc, resulting in singularities in the logarithmic behavior of the rate value. To tackle this, we calculate the rate by using a constant $\delta y \equiv yc - y$ instead of a set y. This approach helps overcome the difficulties associated with non-analyticity and singularity at yc.

In order to maintain the validity of perturbation theory, a particular treatment is required at

the NLO. This procedure entails representing y as the combination of LO and NLO contributions to yc, specifically as $y = yc^{\mathrm{LO}} + yc^{\mathrm{NLO}} - \delta y$. Subsequently, the task involves appropriately allocating the LO and NLO segments of yc to the corresponding components within the action. This approach allows for a consistent expansion and prevents the breakdown of perturbation theory. It is worth noting that without this adjustment, the logarithm of the NLO rate, $log\tilde{\Gamma}_{\mathrm{NLO}}$, would be greater than zero for all studied values of x.

Although not performed in this specific study, it is possible to construct the next-next-leading-order (NNLO) perturbative results using the numerical results presented in references [81, 82]. The procedure for obtaining scale-shifters, as outlined in reference [73], can be employed to derive the NNLO contributions from the available numerical data.

The parallel pattern observed in equilibrium quantities between lattice results and perturbation theory is also evident in the comparison of nucleation rates. The NLO corrections play a crucial role in achieving quantitative agreement, but notable discrepancies still persist.

At LO in powers of x and for a fixed value of $yc - y$, perturbation theory tends to overestimate the nucleation rate significantly. This can be quantified by the ratio $(-\log\tilde{\Gamma}_{\mathrm{LO}})/(-\log\tilde{\Gamma})$, which is approximately $1/2$. In other words, the LO perturbative rate is roughly e^{60} times larger than the actual rate obtained from lattice simulations. Additionally, the dependence of the perturbative rate on $y_{\mathrm{c}} - y$ is found to be shallower compared to the lattice results within the studied range.

Conversely, when attempting to determine the extent of supercooling for a given nucleation rate value, LO perturbation theory tends to consistently underestimate this degree. The ratio $(yc-y)_{\mathrm{LO}}/(yc-y)$ is approximately $1/2$, indicating that the LO approximation predicts a supercooling value that is only half of the actual value obtained from the lattice simulations.

These observations highlight the importance of including NLO corrections to achieve better agreement between perturbation theory and lattice results for both the nucleation rate and the degree of supercooling. When extending perturbation theory to NLO in powers of x, a significant improvement in the agreement with lattice results for the nucleation rate is observed. In the analyzed range, a strong similarity can be observed, with an approximate variance of 20%, between the logarithm of the NLO nucleation rate when considering $y_c - y$ consistently, and the results obtained from the lattice experiments.

However, despite the improved agreement in the overall magnitude of the rate, there is a notable discrepancy in the slope of the rate between perturbation theory and lattice results. This implies a disagreement in the duration of the phase transition, as well as discrepancies in the rates at both larger and smaller supercooling.

These discrepancies have implications for cosmological scenarios where the duration of the phase transition and the rates at different levels of supercooling play important roles. It suggests that beyond NLO, higher-order perturbative calculations or nonperturbative techniques may be necessary to achieve a more accurate description of the nucleation rate and its dependence on the supercooling.

10. VISUALISING BUBBLE NUCLEATION

In **Figure 10.1**, we depict $\phi^\dagger\phi$, illustrating a configuration extracted from a separate boundary region using the values $x = 0.02602457$, $y = 0.0152473$, and $g_3^2 a = 4/7.332605$ and the lattice size is 60^3. For clarity in visualization, the center has been repositioned to the midpoint of the box. To mitigate some of the variations at the lattice scale, the Higgs field was subjected to smoothing using the procedure described in Equation (10.1).

In lattice field theory, the discretization of spacetime introduces a finite lattice spacing a, which leads to lattice artifacts and ultraviolet divergences. These divergences arise from fluctuations on the lattice scale and can be understood as a manifestation of the Ultraviolet

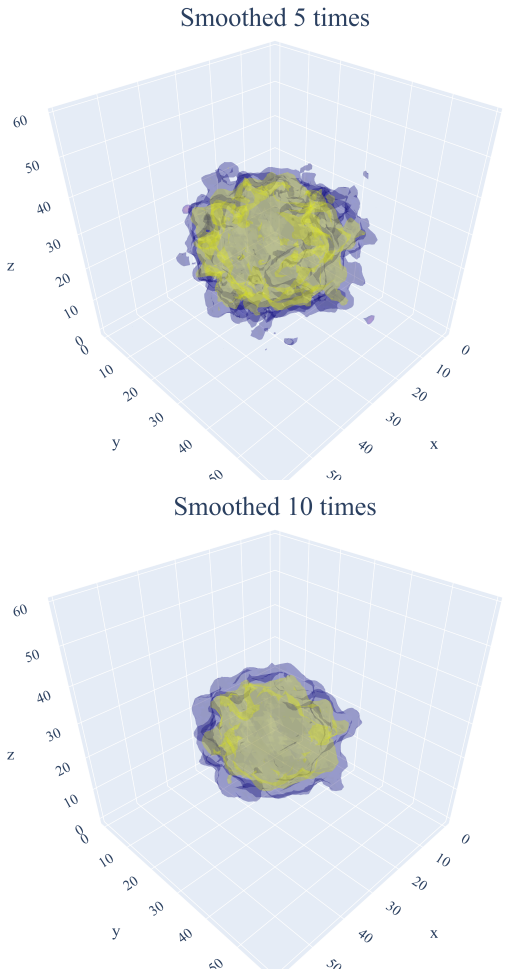


Figure 10.1 Bubble nucleation configuration

Catastrophe.

In the continuum limit, where the lattice spacing a goes to zero ($a \to 0$), these lattice artifacts and divergences become infinite contributions to physical quantities. However, these infinities can be canceled by introducing counterterms in the theory.

The counterterms are additional terms in the action that are introduced to absorb the divergent contributions from the lattice artifacts. The coefficients of these counterterms are chosen such that they precisely cancel the divergent terms, ensuring that physical observables are finite in the continuum limit.

The counterterms typically grow as $1/a$ and $\log a$ as $a \to 0$ to precisely cancel the corresponding lattice artifacts. The specific form of the counterterms depends on the regular-

ization scheme and the specific field theory being considered.

By including the appropriate counterterms, lattice field theory calculations can provide finite and well-defined results in the continuum limit, allowing for reliable predictions and comparisons with experimental data.

In superrenormalizable theories, such as the theory you mentioned, the ultraviolet behavior is relatively simple, which simplifies the computation of counterterms. These counterterms can be computed exactly and are designed to cancel the divergences in physical observables, ensuring their finiteness in the continuum limit.

Nevertheless, it is crucial to acknowledge that although the counterterms address the divergences present in measurable physical quantities, they do not eradicate the fluctuations at the lattice scale within the original lattice field configurations. These fluctuations at the lattice scale are an inherent result of the discretization of spacetime and remain unaffected by the process of renormalization.

Deciphering the intricate task of interpreting the predominant arrangements between the two phases poses significant challenges when it comes to understanding the physical critical bubbles in the continuum limit. The lattice configurations retain lattice artifacts and fluctuations that do not have a clear correspondence to physical observables in the continuum theory. Therefore, additional analysis and extrapolation techniques are required to extract meaningful information about the physical properties and critical behavior of the system from the lattice simulations.

These techniques may involve studying the scaling properties of certain observables, performing extrapolations to the continuum limit, or employing effective field theories to capture the relevant physics. These approaches help bridge the gap between the lattice results and the continuum theory, allowing for a deeper understanding of the system and its critical behavior. Coarse-graining over the lattice scale is a technique that can be employed to construct field configurations with a good continuum limit. This approach

is motivated by the need to capture the relevant physics at larger scales and is particularly important in perturbative approaches to bubble nucleation. The concept of coarse-graining has been examined in the existing literature, as evidenced by the works of [83] and Gould et al. [73]. These studies acknowledge that in the presence of multiple scales, the process of coarse-graining becomes essential for accurately characterizing the critical bubble, particularly at the leading order.

When dealing with scenarios that involve transitions induced by radiation and are affected by quantum fluctuations to a significant extent, the utilization of coarse-graining becomes essential to ensure the survival of the critical bubble within the perturbation theory framework. The lattice-scale fluctuations are effectively integrated out or taken into account through the process of renormalization, which involves computing counterterms to cancel divergences and ensure a well-defined continuum limit.

By performing coarse-graining, one effectively averages or integrates out the lattice-scale fluctuations, leading to a coarse-grained field configuration that captures the relevant long-wavelength physics. This approach allows for a systematic treatment of fluctuations and the hierarchy of scales, bridging the gap between the microscopic lattice description and the macroscopic continuum theory. It provides a framework for analyzing critical phenomena and nucleation processes in a controlled manner.

In our coarse-graining procedure, we employ a smoothing operation to average the Higgs field over neighboring lattice points. The process of achieving the smoothing transformation involves appropriately transporting the field values at every location in conjunction with the values of its neighboring locations. Mathematically, this process can be expressed using the following equation:

$$\phi(x) \to \frac{1}{4}\phi(x) + \frac{1}{8}\sum_i U_i(x)\phi(x+i) + \frac{1}{8}\sum_i U_i^\dagger(x-i)\phi(x-i), \tag{10.1}$$

where $\phi(x)$ represents the Higgs field at lattice site x, $U_i(x)$ is a parallel transporter associated with the link connecting lattice sites x and $x+i$, and $U_i^\dagger(x-i)$ is the hermitian conjugate of $U_i(x-i)$ associated with the link connecting lattice sites $x-i$ and x. The indices i run over the spatial directions.

This smoothing operation helps to incorporate information from neighboring lattice sites and effectively averages out the lattice-scale fluctuations in the field configuration. It is a common technique used in lattice field theory simulations to extract the long-wavelength physics and approximate the continuum limit.

The specific form of the smoothing transformation given in Equation (10.1) represents a weighted average of the Higgs field at the lattice site and its neighboring sites, with the weights determined by the parallel transporters. The choice of parallel transporters ensures that the smoothing respects the gauge symmetries of the theory and properly takes into account the connections between lattice points.

By iteratively applying this smoothing transformation, one can progressively coarse-grain the field configuration and obtain a smoothed version that captures the physics at larger scales, providing a suitable starting point for further analysis or simulations. In the described smoothing procedure, In the described smoothing procedure, the index i traverses the three positive links that connect to close lattice sites, while $U_i(x)$ represents the lattice gauge link variables associated with those links. The precise nature of the parallel transporters relies on the specific gauge theory being considered.

By repeatedly applying the smoothing transformation, the field configuration becomes

progressively coarse-grained. Each iteration of the smoothing operation removes fluctuations on scales smaller than na, where n is the number of smoothing steps and a is the lattice spacing. Consequently, structures with physical sizes smaller than na become less pronounced in the smoothed field.

On the other hand, larger-scale structures are less affected by the smoothing procedure. This implies that if one intends to investigate the field configuration at physical length scales around $\sim l$, it is advantageous to choose a value of n such that $1 \ll n \ll l/a$. In this regime, the field configuration will exhibit the desired features on the chosen physical length scales, while the fine lattice-scale details are smoothed out.

By appropriately selecting the number of smoothing steps, one can effectively separate the relevant physics at different length scales. This approach is particularly useful when studying phenomena that involve a hierarchy of scales, such as the critical bubble in bubble nucleation, where it is crucial to capture both the large-scale structure of the bubble and the small-scale fluctuations in the surrounding medium. In **Figure 10.1**, we can observe two plots displaying the isosurface of $\phi^\dagger\phi$. These plots exhibit the Higgs field after applying a smoothing technique to remove noise at the lattice scale. The specific configurations were obtained from the Boltzmann distribution and recorded when the Markov chain reached a critical threshold characterized by the equation $\phi^\dagger\phi = \varphi_C^2$. To ensure the bubble is positioned at the center, the coordinate origin has been shifted accordingly. Moreover, there is a video accessible at [72] that demonstrates a series of isosurface plots, illustrating the dynamic progression of bubble growth in real-time.

For weaker phase transitions characterized by larger values of x, the critical bubble configurations pertinent to transitions with an action of approximately 100 tend to be relatively larger. This observation can be understood by considering the thin-wall approximation and the behavior of surface tension.

In the thin-wall approximation, the critical bubble is assumed to have a very thin wall

separating the two phases. The surface tension plays a crucial role in determining the energetics of the bubble and its size. For weaker transitions, the surface tension tends to decrease.

When the surface tension decreases, it becomes energetically favorable for larger bubbles to nucleate. This is because, for a fixed value of the action (e.g., ~ 100), decreasing the surface tension leads to an increased nucleation rate. In order to compensate for the increased rate and maintain the same action, the size of the bubble needs to be increased.

Therefore, in the case of weaker transitions where the surface tension is lower, the critical bubbles that contribute significantly to the nucleation rate are expected to be larger in size compared to transitions with higher surface tension.

It is important to note that this argument is based on the thin-wall approximation and assumes that the system obeys the conditions necessary for its validity. Additionally, the relationship between surface tension, bubble size, and nucleation rate can be influenced by various factors, such as the specific dynamics of the phase transition and the underlying field theory.

11. COSMOLOGICAL EVALUATION

The initiation of the phase transition, characterized by the nucleation of approximately one bubble within a Hubble volume, can be determined by examining the equilibrium between the nucleation rate Γ and the Hubble expansion rate H [61, 62, 84]. This balance is described by the equation 11.1

$$-\log\frac{\Gamma}{H^4}+\log\frac{\beta}{H}=0, \tag{11.1}$$

where H is the Hubble rate and where β is the reverse of the characteristic time scale of the PT and described as follows[1]

The term $-\log\left(\frac{\Gamma}{H^4}\right)$ represents the logarithm of the ratio between the nucleation rate and the Hubble expansion rate. When this term is approximately equal to zero, it means that the nucleation rate is comparable to the expansion rate, indicating the onset of bubble nucleation within a Hubble volume.

The term $\log\left(\frac{\beta}{H}\right)$ represents the logarithm of the ratio between the characteristic time scale of the PT and the Hubble time scale. This term accounts for the dynamics of the phase transition and how it compares to the expansion of the Universe.

By solving the equation $-\log\left(\frac{\Gamma}{H^4}\right)+\log\left(\frac{\beta}{H}\right)=0$ for a given nucleation rate Γ, insights into the bulk evolution of the transition can be gained by determining the onset of the phase transition.

[1] In the approximation of semiclassical analysis, the rate is amenable to an approximation: $\Gamma = Ae^{-S}$. Alongside this, β is established as $\beta \equiv -dS/dt$. However, as we advance beyond the limits of the semi-classical approximation, there arises a certain adaptability in expanding this methodology. This introduces a nuanced ambiguity in the definition of β, expressed as $d\log(A/T^4)/d\log T$.

$$\beta \equiv \frac{d}{dt}\log\frac{\Gamma}{T^4} = -HT\frac{d}{dT}\log\frac{\Gamma}{T^4}, \tag{11.2}$$

Equation (11.2) defines the parameter β, which is the inverse of the time scale over which the quantity $\frac{\Gamma}{T^4}$ changes significantly. It represents the rate of change of the nucleation rate relative to the temperature T.

In the context of the evolving phase transition, we can approximate the proportion of space occupied by the symmetric phase as f_{sym} using

$$-\log\Gamma + \log\beta^4 - \log\frac{8\pi}{3}v_{\text{w}}^3 + \log(-\log f_{\text{sym}}) = 0, \tag{11.3}$$

v_{w} is the bubble wall speed.

This equation captures the balance between the nucleation rate ($-\log\Gamma$), the rate of change of the nucleation rate ($\log\beta^4$), the volume factor associated with the bubble wall ($\log\frac{8\pi}{3}v_{\text{w}}^3$), and the logarithm of the fraction of space in the symmetric phase ($\log(-\log f_{\text{sym}})$).

The exponential increase in the nucleation rate over time results in a clearly defined temperature at which the phase transition takes place. Importantly, this holds true irrespective of the specific selection of $f_{\text{sym}} \sim 1$.

By using the adjusted lattice nucleation rate, the equation in Equation (11.3) can be rearranged to establish a practical criterion for percolation. This can be formulated as follows:

$$-\log\tilde{\Gamma} + 4\log\tilde{\beta} \approx 137, \tag{11.4}$$

Equation (11.4) expresses the approximate condition for percolation, determined by the rescaled lattice nucleation rate, where $\tilde{\beta} \equiv -\partial_y \log\tilde{\Gamma}$.

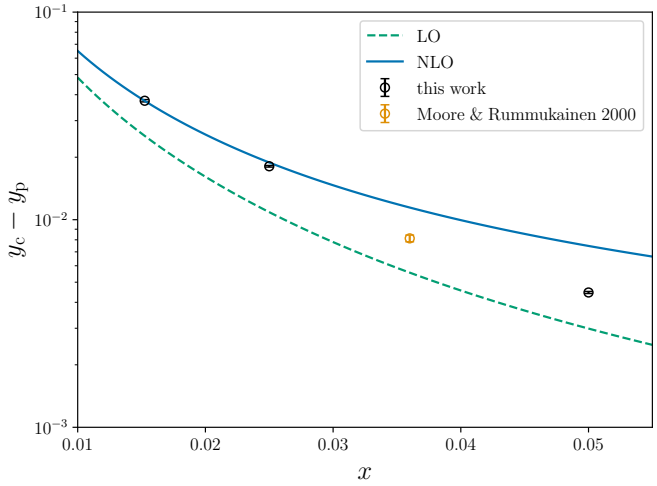


Figure 11.1 The results obtained from the lattice simulations conducted in this study are showcased alongside those from references

To arrive at the value of 137 on the right-hand side, several assumptions and substitutions were made. The transition temperature was assumed to be around 140 GeV [85, 86], and SM-like parameters were used to determine the numerical values [32, 87]. The specific value of 137 may vary by $O(1)$ depending on the particular 4D model under consideration.

$$\beta \approx H\eta_y \cdot \tilde{\beta}, \tag{11.5}$$

The factor β in Equation (11.5) is approximated as $\beta \approx H\eta_y \cdot \tilde{\beta}$, where H is the Hubble parameter and η_y is a characteristic length scale associated with the variation of the nucleation rate with respect to the field variable y. In Equation (11.5), the comparatively slower temperature dependence of variables x and g_3^2/T is disregarded when compared to that of variable y. This is discussed around Euation (4.4).

Furthermore, Equation (11.5) exhibits a factorization of ultraviolet and infrared contributions. This factorization allows for the separation of the effects of short-distance physics (ultraviolet) and long-distance physics (infrared) in the determination of the factor β.

In **Figure 11.1**, the degree of supercooling at percolation, $y_c - y_p$, is presented. This quantity represents the difference between the critical temperature y_c and the percolation

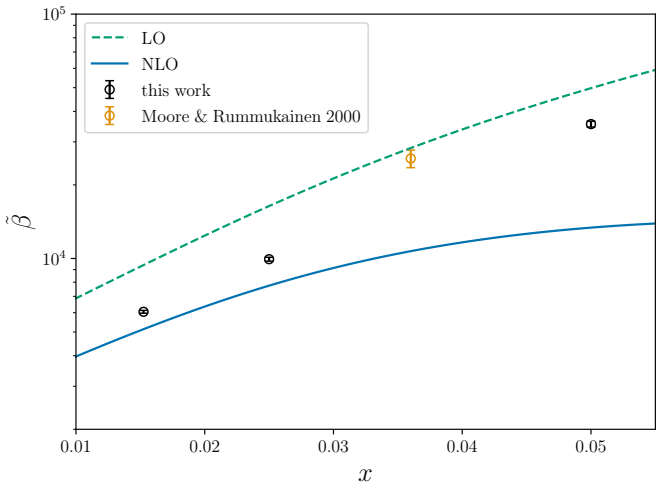


Figure 11.2 Transition at critical point

x	$y_c - y_p$	$\tilde{\beta}_p$
0.0152473	0.03741(47)	$6.052(80) \times 10^3$
0.025	0.01809(16)	$9.93(18) \times 10^3$
0.036*	0.00865(30)	$2.06(21) \times 10^4$
0.05*	0.004461(51)	$3.547(98) \times 10^4$

Table 11.1 Analyzed specifically at the percolation threshold.

temperature y_p, indicating the amount of supercooling achieved during the phase transition.

In **Figure 11.2**, the inverse duration of the transition, $\tilde{\beta}_p$, is shown. This quantity provides a measure of the speed at which the transition occurs.The amount of supercooling reached at the point of percolation, as determined by utilizing Eq.(11.4), is depicted. The results obtained from the lattice simulations conducted in this paper are showcased alongside those from Ref.[32].

In **Table 11.1** The presented data showcases the inverse duration scaling of the transition, analyzed specifically at the percolation threshold. These results are obtained both from study and from other referenced sources. [32]. Noting that the asterisks $(^*)$ indicate that the extrapolation to $a \to 0$ was conducted using only two lattice spacings for these particular values of x.

Both figures include the lattice data as well as the LO and NLO perturbative results.The NLO perturbative results were obtained by employing a rigorous expansion in x to maintain gauge invariance at each order. For the smallest value of x, NLO findings exhibit a robust concurrence with the lattice data. Nonetheless, at $x = 0.05$, no noticeable enhancement is apparent when contrasted with the LO outcomes.

12. RESULTS AND DISCUSSION

This study encompasses an extensive exploration where we employed lattice Monte-Carlo simulations, delving into a comprehensive investigation of the subject matter. Additionally, Our research encompassed the implementation of continuum limit for the SU(2) Higgs 3D EFT, ensuring a comprehensive analysis of the topic at hand. This effective field theory describes the thermodynamics of the electroweak sector of the Standard Model at high temperatures, with small corrections considered. Additionally, it provides insights into the thermodynamics of various BSM extensions.

The study analyzed the parameter space of first-order PTs in this EFT. The motivation behind this investigation stemmed from the relevance of such PTs to planned experiments aimed at detecting gravitational waves. Moreover, the potential for accomplishing EW baryogenesis effectively added to the impetus behind this research.

By conducting extensive simulations and extrapolations, the authors aimed to provide valuable insights into the thermodynamic properties of the SU(2) Higgs 3D EFT and its implications for cosmological phenomena and baryogenesis within the EW sector. The results obtained in this study significantly expand upon the findings of previous works, such as [21] and [32], by providing a comprehensive and reliable data resource. This data can be effectively employed to precisely and quantifiably ascertain diverse characteristics linked to fisrt order PTs in expanded version of the EW sector.

Equations (5.2), (6.2), (9.6), and (11.5) exhibit the demonstration of the separation between infrared and ultraviolet contributions, which constitutes a crucial aspect of our analysis. The factorization facilitates the straightforward extraction of nonperturbative thermodynamic properties for a given 4D model by computing the effective couplings of the corresponding 3D EFT.

In addition to the aforementioned points, it is worth noting that the results obtained from

the analysis of the bubble nucleation rate possess significant implications. These findings offer a valuable opportunity to make estimations and predictions regarding the gravitational wave spectrum that emerges as a consequence of sound waves propagating through the fluid plasma. By examining the rate at which bubbles form within the medium, researchers gain insights into the underlying mechanisms and dynamics of the system, allowing them to better understand the generation and propagation of gravitational waves. This methodology, as exemplified in [85], utilizes the lattice-based bubble nucleation rate obtained from [32] to make predictions regarding the gravitational wave signals associated with phase transitions.

In summary, the extensive and accurate data presented in this study provides valuable resources for studying first-order PTs in extensions of the electroweak sector, including their nonperturbative thermodynamic properties and implications for gravitational wave production.

The outcomes of this research carry direct implications for scenarios that extend BSM, particularly in cases where new degrees of freedom influence the initiation of a first-order PT in the context of Higgs symmetry-breaking. This concept holds significant importance when considering situations in which the degrees of freedom connected to BSM phenomena exhibit effective masses approximately equal to or greater than $O(gT)$. In such cases, the results obtained from the lattice Monte Carlo simulations in the 3D EFT presented in this paper can be directly applied.

In specific scenarios, it is plausible for there to be BSM particles with masses lower than the customary $O(gT)$ magnitude, or for those particles to play an active role in the PT, as seen in instances like biphasic phase shifts. Under such circumstances, conducting fresh Monte Carlo simulations on alternative 3D EFTs becomes imperative. Several references, such as [88–93], explore such scenarios and provide insights into the relevant 3D EFTs to study.

In addition, there are other studies, such as [94, 95], that investigate related contexts where lattice Monte Carlo simulations are employed to study various aspects of phase transitions.

Therefore, while the results presented in this study are directly applicable to BSM scenarios involving heavier degrees of freedom inducing first-order phase transitions, additional lattice simulations and alternative 3D EFTs are necessary for scenarios with lighter or directly participating degrees of freedom.

Within this research, a comprehensive investigation was carried out. During this investigation, significant findings have come to light regarding fundamental thermodynamic measures, including the critical threshold and the extent of disruption in the squared Higgs condensate. These findings have illuminated the distinct functional attributes associated with each. These findings not only hold intrinsic value but also serve as rigorous benchmarks for various perturbative and nonperturbative approaches.

By comparing the results obtained from lattice Monte Carlo simulations to those predicted by perturbative approaches [82, 96–98] and alternative nonperturbative approaches [99, 100], we can quantitatively assess the of these various methods can be quantitatively evaluated in relation to the perturbative expansion parameter. This provides a systematic and rigorous framework for testing the accuracy and applicability of perturbative and nonperturbative approaches in describing non-Abelian gauge theories. Notable references such as [93, 101, 102] provide extensive discussions on these alternative methodologies, emphasizing their importance in comprehending the vast parameter spaces of physical models across various dimensions.

While perturbative methods can be used to analyze the thermodynamics of non-Abelian gauge theories, it comes with limitations [103], the considerable resource needs of lattice Monte Carlo simulations, it becomes crucial to incorporate supplementary approaches to explore the extensive range of parameters within potential physical models. Therefore,

establishing robust benchmarks and evaluating the confidence level in these complementary methods are crucial for advancing our understanding of the thermodynamics of non-Abelian gauge theories.

The precision of predicting various quantities has been assessed by examining the first two terms of the perturbative expansion with respect to the parameter x. Based on our analysis, the NLO approximation yields satisfactory predictions for most of the investigated quantities, particularly when considering values of x up to approximately 0.05. However, it is important to note that there is a significant disparity between the LO and NLO results. To ascertain the convergence of the perturbative expansion and its agreement with lattice results, further investigations at higher orders are required.

Recent developments in the field have addressed the extension to the NNLO in the perturbative expansion. Contemporary works such as [82, 98] present the NNLO calculations, which offer improved precision and allow for a more comprehensive comparison with lattice results. These higher-order calculations provide valuable insights into the convergence properties of the perturbative expansion and facilitate a more accurate determination of the thermodynamic quantities in the considered parameter regime.

The investigation of higher orders in the perturbative expansion is currently a dynamic and vibrant research field. Ongoing endeavors are dedicated to evaluating the convergence and dependability of the perturbative approach when employed to describe the thermodynamic aspects of the non-Abelian gauge theories examined in our study.

In simpler terms, researchers are actively studying how well the perturbative method works when they consider more complex interactions and calculations beyond the basic approximation. They're particularly interested in understanding if the results obtained from this approach accurately match the real behavior of the non-Abelian gauge theories we focused on in our study. An avenue of further exploration that holds interest involves conducting a lattice Monte Carlo analysis of the 3D U(1) Higgs model, present-

ing captivating prospects for study. Unlike the SU(2) case, the U(1) does not encounter the Infrared Problem due to its infrared sector being non-interacting. By building upon the works of Refs. [104, 105], one could simulate varying PT intensities within the U(1) Higgs model and explore the numerical significance of the Infrared Problem.

The Infrared Problem, a fundamental concern in perturbative methodologies for studying the non-Abelian gauge theories, is particularly relevant to the investigation of the SU(2) Higgs model conducted in this study. It arises from the presence of non-perturbative phenomena and complicates the accurate determination of thermodynamic quantities. By contrast, the U(1) Higgs model allows for a more straightforward perturbative treatment, as its infrared sector is free and lacks the complications associated with non-perturbative effects.

By comparing the results of the U(1) Higgs model simulations with those of the SU(2) case, one can quantify the impact of the Infrared Problem on the numerical results. This investigation would provide valuable insights into the significance of non-perturbative effects in the thermodynamics of gauge theories and shed light on the reliability and convergence of perturbative approaches in different models.

Performing such a study would contribute to our understanding of the interplay between non-perturbative phenomena and perturbative calculations, and could potentially guide the development of improved theoretical techniques for analyzing the non-Abelian gauge theories. The simulations employed in this research utilized established and effective algorithms for investigating the 3D bosonic theories [21, 106]. However, this study has highlighted the need for the development of more efficient algorithms tailored precisely to calculate the rate of bubble nucleation.

To ensure an accurate calculation of the bubble nucleation rate, it is imperative to employ large lattices that can adequately accommodate critical bubbles. In the instance of the multicanonical algorithm discussed in the reference mentioned as Ref. [21], it becomes

essential to employ considerably long Markov chains to adequately sample the complete phase space. However, a challenge emerges because the order parameter $\phi^\dagger\phi$ averaged across the lattice volume lacks the capacity to distinguish between emerging, confined bubbles and the pervasive fluctuations dispersed throughout the lattice. Consequently, the multicanonical algorithm may not be able to efficiently explore the entire phase space of a system, especially if there are large barriers between different phases.

More efficient algorithms for simulating bubble nucleation are needed to overcome the limitations of current methods. Such algorithms should be designed to address the specific challenges associated with sampling the phase space of systems undergoing phase transitions and the formation of critical bubbles. By improving the efficiency of the algorithms, it would be possible to reduce the computational resources and time required to accurately calculate the bubble nucleation rate.

Advancements in algorithm development for bubble nucleation simulations would not only enhance the accuracy and reliability of calculations in the field but also enable more extensive investigations of phase transitions and critical phenomena in various physical models. Consequently, the advancement of effective algorithms specifically designed to calculate bubble nucleation constitutes a crucial subsequent stage in this area of study.

REFERENCES

1. S. Chatrchyan *et al.*, "Observation of a New Boson at a Mass of 125 GeV with the CMS Experiment at the LHC," *Phys. Lett. B*, vol. 716, pp. 30–61, 2012.

2. B. P. Abbott *et al.*, "Observation of Gravitational Waves from a Binary Black Hole Merger," *Phys. Rev. Lett.*, vol. 116, no. 6, p. 061102, 2016.

3. S. Kawamura *et al.*, "The Japanese space gravitational wave antenna: DECIGO," *Class. Quant. Grav.*, vol. 28, p. 094011, 2011.

4. W.-H. Ruan, Z.-K. Guo, R.-G. Cai, and Y.-Z. Zhang, "Taiji program: Gravitational-wave sources," *International Journal of Modern Physics A*, vol. 35, p. 2050075, jun 2020.

5. D. J. Weir, "Gravitational waves from a first order electroweak phase transition: a brief review," *Phil. Trans. Roy. Soc. Lond. A*, vol. 376, no. 2114, p. 20170126, 2018.

6. D. E. Morrissey and M. J. Ramsey-Musolf, "Electroweak baryogenesis," *New J. Phys.*, vol. 14, p. 125003, 2012.

7. M. D'Onofrio and K. Rummukainen, "Standard model cross-over on the lattice," *Phys. Rev. D*, vol. 93, no. 2, p. 025003, 2016.

8. T. Konstandin, "Quantum Transport and Electroweak Baryogenesis," *Phys. Usp.*, vol. 56, pp. 747–771, 2013.

9. C. Caprini and D. G. Figueroa, "Cosmological backgrounds of gravitational waves," *Classical and Quantum Gravity*, vol. 35, p. 163001, jul 2018.

10. D. J. Weir, "Gravitational waves from a first-order electroweak phase transition: a brief review," *Philosophical Transactions of the Royal Society A: Mathematical, Physical and Engineering Sciences*, vol. 376, p. 20170126, jan 2018.

11. M. B. Hindmarsh, M. Lüben, J. Lumma, and M. Pauly, "Phase transitions in the early universe," *SciPost Phys. Lect. Notes*, vol. 24, p. 1, 2021.

12. B. A. Berg and T. Neuhaus, "Multicanonical ensemble: A new approach to simulate first-order phase transitions," *Phys. Rev. Lett.*, vol. 68, pp. 9–12, Jan 1992.

13. D. P. Landau and K. Binder, *A Guide to Monte Carlo Simulations in Statistical Physics*. Cambridge University Press, 4 ed., 2014.

14. M. E. J. Newman and G. T. Barkema, *Monte Carlo methods in statistical physics*. Oxford: Clarendon Press, 1999.

15. K. Kajantie, M. Laine, K. Rummukainen, and M. Shaposhnikov, "The electroweak phase transition: a non-perturbative analysis," *Nuclear Physics B*, vol. 466, pp. 189–258, apr 1996.

16. M. Quiros, "Finite temperature field theory and phase transitions," *Proceedings, Summer school in high-energy physics and cosmology: Trieste, Italy*, vol. 1999, pp. 187–259, 1998.

17. S. Weinberg, "Cosmological fluctuations of small wavelength," *The Astrophysical Journal*, vol. 581, pp. 810–816, dec 2002.

18. K. Kajantie, M. Laine, K. Rummukainen, and M. E. Shaposhnikov, "Generic rules for high temperature dimensional reduction and their application to the standard model," *Nucl. Phys.*, vol. B458, pp. 90–136, 1996.

19. K. Rummukainen, M. Tsypin, K. Kajantie, M. Laine, and M. E. Shaposhnikov, "The Universality class of the electroweak theory," *Nucl. Phys.*, vol. B532, pp. 283–314, 1998.

20. G. D. Moore and N. Schlusser, "Full O(a) improvement in electrostatic QCD," *Phys. Rev. D*, vol. 100, no. 3, p. 034510, 2019.

21. K. Kajantie, M. Laine, K. Rummukainen, and M. E. Shaposhnikov, "The Electroweak phase transition: A Nonperturbative analysis," *Nucl. Phys.*, vol. B466, pp. 189–258, 1996.

22. M. Laine and K. Rummukainen, "What's new with the electroweak phase transition?," *Nuclear Physics B - Proceedings Supplements*, vol. 73, pp. 180–185, mar 1999.

23. A. Ekstedt, O. Gould, and J. Löfgren, "Radiative first-order phase transitions to next-to-next-to-leading order," *Physical Review D*, vol. 106, aug 2022.

24. A. Ekstedt, "Convergence of the nucleation rate for first-order phase transitions," *Physical Review D*, vol. 106, nov 2022.

25. K. Kajantie, M. Laine, K. Rummukainen, and M. Shaposhnikov, "3d SU(n) adjoint higgs theory and finite-temperature QCD," *Nuclear Physics B*, vol. 503, pp. 357–384, oct 1997.

26. K. Farakos, K. Kajantie, K. Rummukainen, and M. E. Shaposhnikov, "3-d physics and the electroweak phase transition: A Framework for lattice Monte Carlo analysis," *Nucl. Phys.*, vol. B442, pp. 317–363, 1995.

27. G. D. Moore and N. Turok, "Classical field dynamics of the electroweak phase transition," *Phys. Rev. D*, vol. 55, pp. 6538–6560, 1997.

28. G. D. Moore, "O(a) errors in 3-D SU(N) Higgs theories," *Nucl. Phys.*, vol. B523, pp. 569–593, 1998.

29. K. Binder, "Monte Carlo calculation of the surface tension for two- and three-dimensional lattice-gas models," *Phys. Rev. A*, vol. 25, no. 3, p. 1699, 1982.

30. B. Bunk, "A note on interfaces with periodic boundaries," *International Journal of Modern Physics C*, vol. 3, no. 05, pp. 889–896, 1992.

31. Y. Iwasaki, K. Kanaya, L. Karkkainen, K. Rummukainen, and T. Yoshie, "Interface tension in quenched QCD," *Phys. Rev. D*, vol. 49, pp. 3540–3545, 1994.

32. G. D. Moore and K. Rummukainen, "Electroweak bubble nucleation, nonperturbatively," *Phys. Rev.*, vol. D63, p. 045002, 2001.

33. M. Hindmarsh, S. J. Huber, K. Rummukainen, and D. J. Weir, "Gravitational waves from the sound of a first order phase transition," *Phys. Rev. Lett.*, vol. 112, p. 041301, 2014.

34. M. Hindmarsh, S. J. Huber, K. Rummukainen, and D. J. Weir, "Numerical simulations of acoustically generated gravitational waves at a first order phase transition," *Phys. Rev. D*, vol. 92, no. 12, p. 123009, 2015.

35. M. Hindmarsh, S. J. Huber, K. Rummukainen, and D. J. Weir, "Shape of the acoustic gravitational wave power spectrum from a first order phase transition," *Phys. Rev. D*, vol. 96, no. 10, p. 103520, 2017. [Erratum: Phys.Rev.D 101, 089902 (2020)].

36. D. Bodeker, "On the effective dynamics of soft nonAbelian gauge fields at finite temperature," *Phys. Lett. B*, vol. 426, pp. 351–360, 1998.

37. D. Bodeker, "From hard thermal loops to Langevin dynamics," *Nucl. Phys. B*, vol. 559, pp. 502–538, 1999.

38. D. Bodeker, "Diagrammatic approach to soft nonAbelian dynamics at high temperature," *Nucl. Phys. B*, vol. 566, pp. 402–422, 2000.

39. P. B. Arnold, D. T. Son, and L. G. Yaffe, "Effective dynamics of hot, soft nonAbelian gauge fields. Color conductivity and log(1/alpha) effects," *Phys. Rev. D*, vol. 59, p. 105020, 1999.

40. P. B. Arnold, D. T. Son, and L. G. Yaffe, "Longitudinal subtleties in diffusive Langevin equations for nonAbelian plasmas," *Phys. Rev. D*, vol. 60, p. 025007, 1999.

41. P. B. Arnold and L. G. Yaffe, "High temperature color conductivity at next-to-leading log order," *Phys. Rev. D*, vol. 62, p. 125014, 2000.

42. D. F. Litim and C. Manuel, "Mean field dynamics in nonAbelian plasmas from classical transport theory," *Phys. Rev. Lett.*, vol. 82, pp. 4981–4984, 1999.

43. D. F. Litim and C. Manuel, "Effective transport equations for nonAbelian plasmas," *Nucl. Phys. B*, vol. 562, pp. 237–274, 1999.

44. D. F. Litim and C. Manuel, "Fluctuations from dissipation in a hot nonAbelian plasma," *Phys. Rev. D*, vol. 61, p. 125004, 2000.

45. G. D. Moore, "The Sphaleron rate: Bodeker's leading log," *Nucl. Phys. B*, vol. 568, pp. 367–404, 2000.

46. G. D. Moore, "Sphaleron rate in the symmetric electroweak phase," *Phys. Rev. D*, vol. 62, p. 085011, 2000.

47. O. Gould, S. Güyer, and K. Rummukainen, "First-order electroweak phase transitions: A nonperturbative update," *Physical Review D*, vol. 106, dec 2022.

48. E. Braaten and R. D. Pisarski, "Soft Amplitudes in Hot Gauge Theories: A General Analysis," *Nucl. Phys. B*, vol. 337, pp. 569–634, 1990.

49. J. Frenkel and J. C. Taylor, "High Temperature Limit of Thermal QCD," *Nucl. Phys. B*, vol. 334, pp. 199–216, 1990.

50. J. C. Taylor and S. M. H. Wong, "The Effective Action of Hard Thermal Loops in QCD," *Nucl. Phys. B*, vol. 346, pp. 115–128, 1990.

51. J. Frenkel and J. C. Taylor, "Hard thermal QCD, forward scattering and effective actions," *Nucl. Phys. B*, vol. 374, pp. 156–168, 1992.

52. E. Braaten and R. D. Pisarski, "Simple effective Lagrangian for hard thermal loops," *Phys. Rev. D*, vol. 45, no. 6, p. R1827, 1992.

53. J. P. Blaizot and E. Iancu, "Kinetic equations for long wavelength excitations of the quark - gluon plasma," *Phys. Rev. Lett.*, vol. 70, pp. 3376–3379, 1993.

54. J. P. Blaizot and E. Iancu, "Soft collective excitations in hot gauge theories," *Nucl. Phys. B*, vol. 417, pp. 608–673, 1994.

55. V. P. Nair, "Hard thermal loops, gauged WZNW action and the energy of hot quark - gluon plasma," *Phys. Rev. D*, vol. 48, pp. R3432–R3435, 1993.

56. C. R. Hu and B. Muller, "Classical lattice gauge field with hard thermal loops," *Phys. Lett. B*, vol. 409, pp. 377–381, 1997.

57. G. D. Moore, C.-r. Hu, and B. Muller, "Chern-Simons number diffusion with hard thermal loops," *Phys. Rev. D*, vol. 58, p. 045001, 1998.

58. D. Bodeker, L. D. McLerran, and A. V. Smilga, "Really computing nonperturbative real time correlation functions," *Phys. Rev. D*, vol. 52, pp. 4675–4690, 1995.

59. D. Bodeker, G. D. Moore, and K. Rummukainen, "Chern-Simons number diffusion and hard thermal loops on the lattice," *Phys. Rev. D*, vol. 61, p. 056003, 2000.

60. E. Iancu, "Effective theory for real time dynamics in hot gauge theories," *Phys. Lett. B*, vol. 435, pp. 152–158, 1998.

61. K. Enqvist, J. Ignatius, K. Kajantie, and K. Rummukainen, "Nucleation and bubble growth in a first order cosmological electroweak phase transition," *Phys. Rev. D*, vol. 45, pp. 3415–3428, 1992.

62. G. W. Anderson and L. J. Hall, "The Electroweak phase transition and baryogenesis," *Phys. Rev. D*, vol. 45, pp. 2685–2698, 1992.

63. O. T. Valls and G. F. Mazenko, "Nucleation in a time-dependent ginzburg-landau model: A numerical study," *Phys. Rev. B*, vol. 42, pp. 6614–6622, Oct 1990.

64. M. G. Alford, H. Feldman, and M. Gleiser, "Thermal nucleation of kink - anti-kink pairs," *Phys. Rev. Lett.*, vol. 68, pp. 1645–1648, 1992.

65. M. G. Alford and M. Gleiser, "Metastability in two-dimensions and the effective potential," *Phys. Rev. D*, vol. 48, pp. 2838–2844, 1993.

66. M. G. Alford, H. Feldman, and M. Gleiser, "Thermal activation of metastable decay: Testing nucleation theory," *Phys. Rev. D*, vol. 47, pp. R2168–R2171, 1993.

67. S. Borsanyi, A. Patkos, J. Polonyi, and Z. Szep, "Fate of the classical false vacuum," *Phys. Rev. D*, vol. 62, p. 085013, 2000.

68. G. D. Moore, K. Rummukainen, and A. Tranberg, "Nonperturbative computation of the bubble nucleation rate in the cubic anisotropy model," *JHEP*, vol. 04, p. 017, 2001.

69. J. S. Langer, "Statistical theory of the decay of metastable states," *Annals Phys.*, vol. 54, pp. 258–275, 1969.

70. G. D. Moore, "Measuring the broken phase sphaleron rate nonperturbatively," *Phys. Rev. D*, vol. 59, p. 014503, 1999.

71. G. D. Moore, "A Nonperturbative measurement of the broken phase sphaleron rate," *Phys. Lett. B*, vol. 439, pp. 357–365, 1998.

72. O. Gould, S. Güyer, and K. Rummukainen, "Dataset for 'First-order electroweak phase transitions: a nonperturbative update'," May.

73. O. Gould and J. Hirvonen, "Effective field theory approach to thermal bubble nucleation," *Phys. Rev. D*, vol. 104, no. 9, p. 096015, 2021.

74. A. Ekstedt, "Bubble Nucleation to All Orders," 1 2022.

75. O. Gould, S. Güyer, and S. Rummukainen 2022. https://zenodo.org/record/6539259.

76. M. Biskup, L. Chayes, and R. Kotecký, "On the formation/dissolution of equilibrium droplets," *EPL (Europhysics Letters)*, vol. 60, no. 1, p. 21, 2002.

77. K. Binder, "Theory of the evaporation/condensation transition of equilibrium droplets in finite volumes," *Physica A: Statistical Mechanics and its Applications*, vol. 319, pp. 99–114, 2003.

78. A. Nußbaumer, E. Bittner, T. Neuhaus, and W. Janke, "Monte carlo study of the evaporation/condensation transition of ising droplets," *Europhysics Letters (EPL)*, vol. 75, pp. 716–722, sep 2006.

79. J. Hirvonen, J. Löfgren, M. J. Ramsey-Musolf, P. Schicho, and T. V. I. Tenkanen, "Computing the gauge-invariant bubble nucleation rate in finite temperature effective field theory," 12 2021.

80. J. Löfgren, M. J. Ramsey-Musolf, P. Schicho, and T. V. I. Tenkanen, "Nucleation at finite temperature: a gauge-invariant, perturbative framework," 12 2021.

81. A. Ekstedt, "Higher-order corrections to the bubble-nucleation rate at finite temperature," *Eur. Phys. J. C*, vol. 82, no. 2, p. 173, 2022.

82. A. Ekstedt, "Convergence of the nucleation rate for first-order phase transitions," 5 2022.

83. J. Langer, "Metastable states," *Physica*, vol. 73, no. 1, pp. 61–72, 1974.

84. A. H. Guth and E. J. Weinberg, "Cosmological Consequences of a First Order Phase Transition in the SU(5) Grand Unified Model," *Phys. Rev. D*, vol. 23, p. 876, 1981.

85. O. Gould, J. Kozaczuk, L. Niemi, M. J. Ramsey-Musolf, T. V. I. Tenkanen, and D. J. Weir, "Nonperturbative analysis of the gravitational waves from a first-order electroweak phase transition," *Phys. Rev. D*, vol. 100, no. 11, p. 115024, 2019.

86. M. J. Ramsey-Musolf, "The electroweak phase transition: a collider target," *JHEP*, vol. 09, p. 179, 2020.

87. C. Caprini *et al.*, "Detecting gravitational waves from cosmological phase transitions with LISA: an update," *JCAP*, vol. 03, p. 024, 2020.

88. M. Laine and K. Rummukainen, "The MSSM electroweak phase transition on the lattice," *Nucl. Phys. B*, vol. 535, pp. 423–457, 1998.

89. M. Laine and K. Rummukainen, "Higgs sector CP violation at the electroweak phase transition," *Nucl. Phys. B*, vol. 545, pp. 141–182, 1999.

90. M. Laine, G. Nardini, and K. Rummukainen, "Lattice study of an electroweak phase transition at $m_h \backsimeq 126$ GeV," *JCAP*, vol. 01, p. 011, 2013.

91. K. Kainulainen, V. Keus, L. Niemi, K. Rummukainen, T. V. I. Tenkanen, and V. Vaskonen, "On the validity of perturbative studies of the electroweak phase transition in the Two Higgs Doublet model," *JHEP*, vol. 06, p. 075, 2019.

92. L. Niemi, M. J. Ramsey-Musolf, T. V. I. Tenkanen, and D. J. Weir, "Thermodynamics of a Two-Step Electroweak Phase Transition," *Phys. Rev. Lett.*, vol. 126, no. 17, p. 171802, 2021.

93. O. Gould, "Real scalar phase transitions: a nonperturbative analysis," *JHEP*, vol. 04, p. 057, 2021.

94. G. Cossu, L. Del Debbio, A. Juttner, B. Kitching-Morley, J. K. L. Lee, A. Portelli, H. B. Rocha, and K. Skenderis, "Nonperturbative Infrared Finiteness in a Superrenormalizable Scalar Quantum Field Theory," *Phys. Rev. Lett.*, vol. 126, no. 22, p. 221601, 2021.

95. G. Galati and M. Serone, "Cancellation of IR divergences in 3d Abelian gauge theories," *JHEP*, vol. 02, p. 123, 2022.

96. W. Buchmuller, Z. Fodor, and A. Hebecker, "Gauge invariant treatment of the electroweak phase transition," *Phys. Lett. B*, vol. 331, pp. 131–136, 1994.

97. M. C. A. York and G. D. Moore, "2PI resummation in 3D SU(N) Higgs theory," *JHEP*, vol. 10, p. 105, 2014.

98. A. Ekstedt, O. Gould, and J. Löfgren, "Radiative first-order phase transitions to next-to-next-to-leading order," *Physical Review D*, vol. 106, aug 2022.

99. J. Elias-Miró and E. Hardy, "Exploring Hamiltonian Truncation in $\mathbf{d} = \mathbf{2} + \mathbf{1}$," *Phys. Rev. D*, vol. 102, no. 6, p. 065001, 2020.

100. G. Sberveglieri, M. Serone, and G. Spada, "Self-Dualities and Renormalization Dependence of the Phase Diagram in 3d $O(N)$ Vector Models," *JHEP*, vol. 02, p. 098, 2021.

101. P. B. Arnold, S. R. Sharpe, L. G. Yaffe, and Y. Zhang, "Weakly first order phase transitions: The Epsilon expansion versus numerical simulations in the cubic anisotropy model," *Phys. Rev. Lett.*, vol. 78, pp. 2062–2065, 1997.

102. N. Tetradis, "Comparison of renormalization group and lattice studies of the electroweak phase transition," *Phys. Lett. B*, vol. 409, pp. 355–362, 1997.

103. A. D. Linde, "Infrared Problem in Thermodynamics of the Yang-Mills Gas," *Phys. Lett. B*, vol. 96, pp. 289–292, 1980.

104. K. Kajantie, M. Karjalainen, M. Laine, and J. Peisa, "Three-dimensional U(1) gauge + Higgs theory as an effective theory for finite temperature phase transitions," *Nucl. Phys. B*, vol. 520, pp. 345–381, 1998.

105. K. Kajantie, M. Karjalainen, M. Laine, and J. Peisa, "Masses and phase structure in the Ginzburg-Landau model," *Phys. Rev. B*, vol. 57, pp. 3011–3016, 1998.

106. B. A. Berg and T. Neuhaus, "Multicanonical ensemble: A New approach to simulate first order phase transitions," *Phys. Rev. Lett.*, vol. 68, pp. 9–12, 1992.

107. K. Farakos, K. Kajantie, K. Rummukainen, and M. E. Shaposhnikov, "3-D physics and the electroweak phase transition: Perturbation theory," *Nucl. Phys.*, vol. B425, pp. 67–109, 1994.

108. M. Laine, "Gauge dependence of the high temperature two loop effective potential for the Higgs field," *Phys. Rev. D*, vol. 51, pp. 4525–4532, 1995.

109. K. Kajantie, M. Laine, K. Rummukainen, and M. E. Shaposhnikov, "3-D SU(N) + adjoint Higgs theory and finite temperature QCD," *Nucl. Phys. B*, vol. 503, pp. 357–384, 1997.

110. P. B. Arnold and O. Espinosa, "The Effective potential and first order phase transitions: Beyond leading-order," *Phys. Rev.*, vol. D47, p. 3546, 1993. [Erratum: Phys. Rev.D50,6662(1994)].

111. A. Ekstedt and J. Löfgren, "A Critical Look at the Electroweak Phase Transition," *JHEP*, vol. 12, p. 136, 2020.

112. J. Hirvonen, "Intuitive method for constructing effective field theories," 5 2022.

13. APPENDIX

13.1. Continuum Extrapolations

In this appendix, we gather a representative collection of figures that illustrate our extrapolations across a continuum based on lattice data acquired from finite lattices; **Figure 13.1**, **Figure 13.2**, **Figure 13.4**, **Figure 13.3** and **Figure 13.5**. As discussed in Secs. 4. 5. 6. 9., the relationship between volume and lattice spacing varies depending on the specific observable.

In **Figure 13.3** the extrapolation towards the limit approaching infinity for the surface tension at a specific value of $x = 0.075$. Conversely, the upper segment illustrates an extrapolation towards the limit of a considerably large volume to examine the change in the

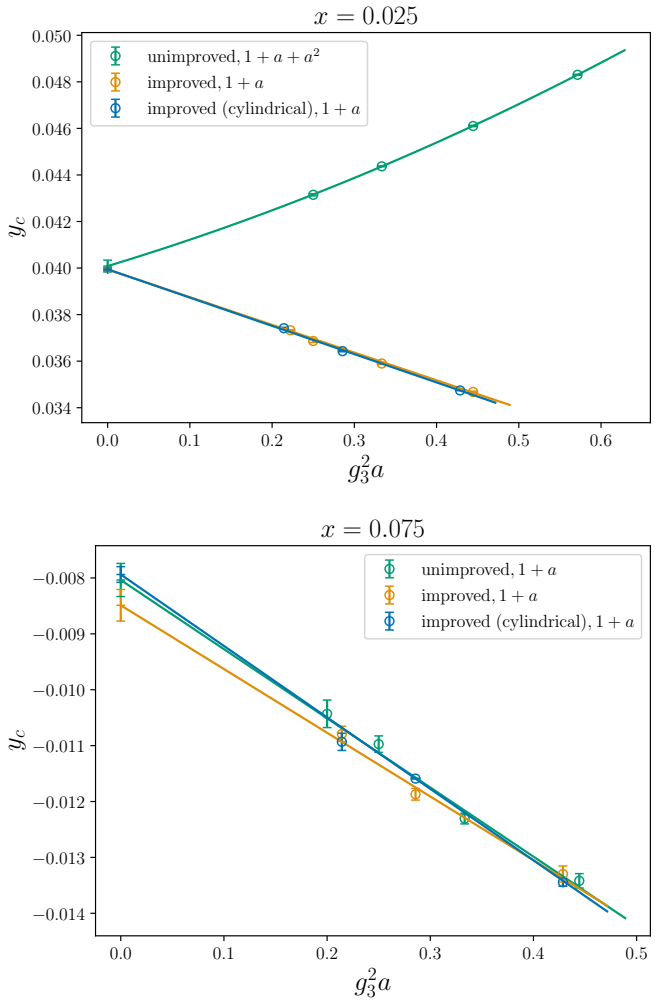


Figure 13.1 The critical mass y_c for two different values of x.

squared Higgs condensate. In this particular situation, corrections related to volume are considerably reduced, allowing for a simple fitting process with a constant value utilizing only the most significant volumes.

In **Figure 13.4**, we apply an extrapolation to the limit of infinite volume for T_c corresponding to $x = 0.025$ and for the surface tension associated with $x = 0.075$. When estimating the critical temperature at $x = 0.025$, volume corrections have a negligible effect. As a result, we can approximate a constant value by fitting the data obtained from the largest volumes. However, when examining the surface tension at $x = 0.075$, we take into account the impact of capillary waves. To achieve, we subtract their contributions from the extrapolated surface tension value using Equation (6.3).

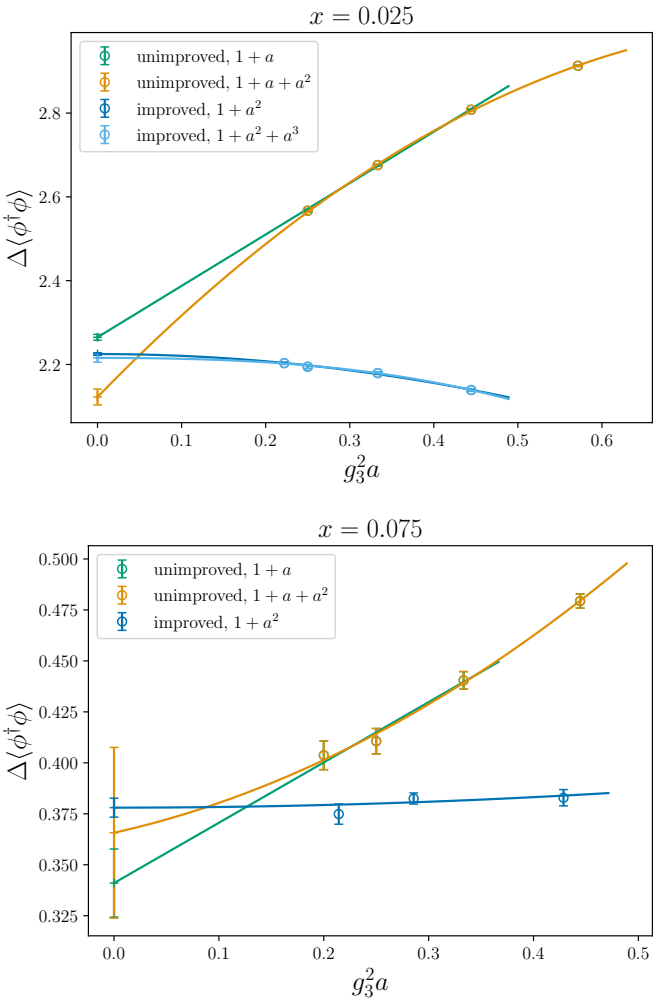


Figure 13.2 The Higgs quadratic condensate for two different values of x.

For quantities that rely exclusively on bulk properties in uniform phases, such as y_c, $\Delta\langle\phi^\dagger\phi\rangle_c$, and $\Delta\langle(\phi^\dagger\phi)^2\rangle_c$, their dependence on volume diminishes exponentially in significantly large volumes.Similarly, when the lattice accommodates a relatively small portion occupied by the bubble, the bubble nucleation rate also showcases an exponential reduction in volume dependence. This decrease is attributed to the presence of periodic boundaries, which prevent interactions among the bubbles. In these cases, we perform a fitting procedure by considering a constant value that best matches the outcomes derived from the largest lattices, ensuring their agreement falls within the specified margin of error. We can subtract the analytically known leading dependence from the lattice spacing of the surface tension, enabling us to fit the remaining dependence. In the absence of $O(a)$

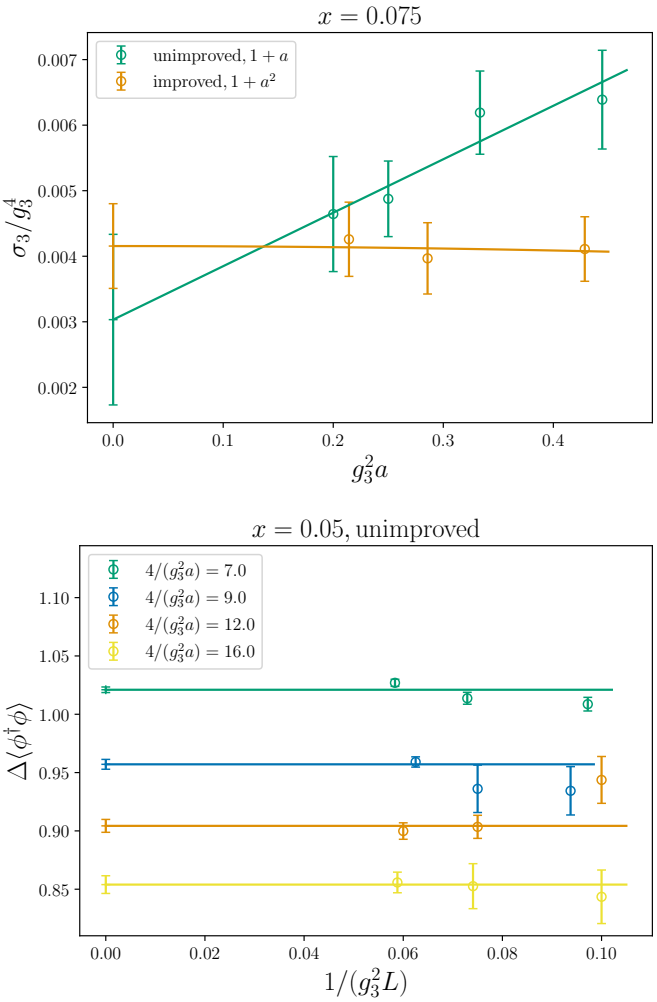


Figure 13.3 Extrapolations for surface tension at specific value of $x = 0.025$ and $x = 0.075$

improvement, the physical quantities we consider are subject to $O(a)$ corrections due to the finite lattice spacing. To account for these corrections, we perform polynomial fits and choose the lowest degree polynomial that yields a reduced chi-square value $\chi^2/\text{d.o.f.} \sim 1$. Typically, we use either a quadratic polynomial $1 + a + a^2$ or a linear polynomial $1 + a$.

However, with $O(a)$ improvement, the linear dependence on the lattice spacing is cancelled for all quantities except y_c. Hence, when implementing $O(a)$ enhancement, we exclude the linear component from the polynomial approximations. The advantages of $O(a)$ improvements are notably pronounced in the case of condensates and surface tension, as it aids in mitigating and managing lattice spacing artifacts.

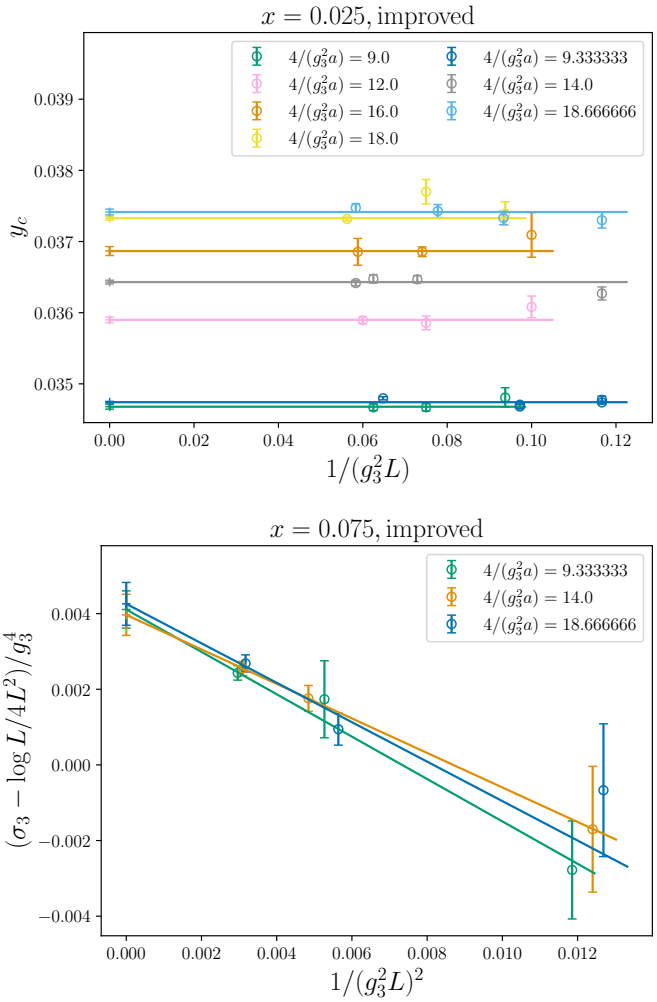


Figure 13.4 Lattice Monte Carlo Simulation results for Surface Tension

13.2. Perturbative Results

Here are perturbative outcomes regarding the beta functions associated with the couplings [107]:

$$\beta_y = \frac{1}{(4\pi)^2}\left(-\frac{51}{16} - 9x + 12x^2\right), \tag{13.1}$$

$$\beta_x = \beta_{g_3^2} = 0. \tag{13.2}$$

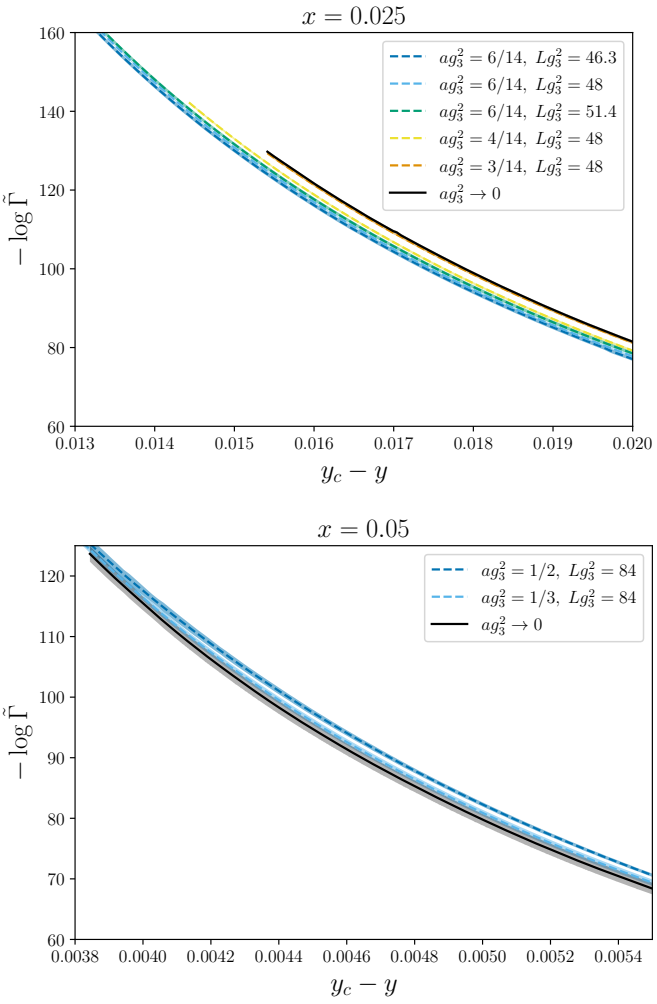


Figure 13.5 The nucleation rate is extrapolated to the continuum limit for two different values of x.

These beta functions are exact in the theory, thanks to its superrenormalizability. At tree-level in the 3D EFT, symmetry-breaking phase transitions occur at $m_3^2 = 0$ and are second order. HNevertheless, alterations in the transition sequence can arise due to loop corrections. In the case of a phase transition of the first order, the critical temperature takes place when m_3^2 is greater than zero. It is noteworthy that the utilization of a comprehensive loop expansion in the analysis of the transition may result in infrared divergences and incidental presence of imaginary components at $O(\hbar^2)$. [108], highlighting the limitations of employing the loop expansion in this particular scenario. The presence of these infrared divergences highlights the need for nonperturbative methods to properly describe the phase transition and its order in the 3D EFT. For sufficiently small x, it is possible

to construct a perturbative expansion in x for the 3D SU(2) Higgs theory [32, 104, 109]. This expansion entails the inclusion of specific one-loop terms within the LO approximation, resulting in the resummation of the loop expansion. The expansion that emerges is strongly connected to the coupling expansion, specifically when the 4D couplings adhere to the condition $\lambda \sim g^3$ [110, 111]. Recent works have further developed and formalized this expansion, extending it to NNLO [82, 98]. These advancements provide a more accurate description of the physics of the 3D SU(2) Higgs theory and allow for a better understanding of the phase transition behavior. The EFT approach offers a reliable technique for perturbatively calculating the nucleation rate in thermal bubble nucleation scenarios. [73]. This method entails the creation of an effective action, known as the effective action at the nucleation scale S_{nucl}, through the process of integrating out the modes that are relatively heavier in terms of their parameters. This integration can be performed directly in the path integral formulation [112].

At low values of x in SU(2) Higgs theory, the gauge fields possess the potential to attain a considerable mass relative to the Higgs field within the bubble. Consequently, it becomes necessary to integrate them out to derive an effective representation. However, in the symmetric phase, the gauge fields possess lower mass and assume the role of scale-shifters [73]. In the case of LO and NLO, the integration of gauge fields leads to localized terms in the effective action. However, as we move to higher orders of perturbation theory, these terms exhibit nonlocal attributes.

At LO, the nucleation scale effective action S^{LO}nucl for the SU(2) Higgs theory is given by the following expression:

$$S_{\text{nucl}}^{\text{LO}} = \int d^3x \left[\frac{1}{2}(\partial_i \phi)^2 + \frac{1}{2} m_3^2 \phi^2 - \frac{g_3^3 |\phi|^3}{4(4\pi)} + \frac{1}{4}\lambda_3 \phi^4 \right].$$

Here, ϕ represents a background field with real values. When analyzing the critical bubble, it is assumed that the mass does not deviate significantly from the critical mass, the action demonstrates a reliance on the parameter x at a magnitude of approximately

$O(x^{-3/2})$. The expressions that encompass the NLO adjustments to the effective action of nucleation scale, denoted as $S^{\mathrm{NLO}}\mathrm{nucl}$, are as follows:

$$S_{\mathrm{nucl}}^{\mathrm{NLO}} = \int d^3x \left[\frac{1}{2} \left(-\frac{11 g_3}{4(4\pi)|\phi|} \right) (\partial_i \phi)^2 + \frac{g_3^4 \phi^2}{(4\pi)^2} \left(\frac{51}{32} \log \left(\frac{\mu_3}{g_3 |\phi|} \right) + \frac{33}{64} - \frac{63}{32} \log \left(\frac{3}{2} \right) \right) \right].$$

When examined with regards to the crucial bubble, these NLO adjustments exhibit a dependence on the parameter x at a scale of $O(x^{-1/2})$. The nucleation scale effective action and its NLO corrections have been discussed in several references, including Refs. [32, 73, 79–81]. Corrections to $S^{\mathrm{LO}}\mathrm{nucl} + S^{\mathrm{NLO}}\mathrm{nucl}$ arise at $O(x^0)$ due to nucleation scale or lighter modes fluctuating in the background of the critical bubble. These corrections become significant when the mass is not significantly smaller than the critical mass. The specific nature of these alterations is contingent upon the characteristics of the critical bubble and impacts the statistical prefactor associated with the nucleation rate. The theory's statistical prefactor calculation has been executed in Refs. [81, 82].

Moreover, within the same order $O(x^0)$, adjustments to the nucleation rate arise from the dynamic prefactor, which accounts for the real-time expansion of the critical bubble. These corrections have been extensively studied in the literature, including works by Langer [69], Gould et al. [73], and Ekstedt et al. [74]. However, in the perturbative analysis presented in the current work, the computation of these corrections has not been carried out. Indeed, the utilization of the nucleation scale effective action allows for the computation of the equilibrium properties associated with the phase transition. This relationship arises from the fact that the dominant contributions to the change in free energy ΔF originate from the heaviest modes, which are integrated out to obtain the nucleation scale effective action. As a result, at LO and NLO, one can approximate ΔF as $\Delta F \approx T S_{\mathrm{nucl}}$, where T is the temperature and S_{nucl} is the nucleation scale effective action. This connection between ΔF and S_{nucl} is not accidental, highlighting the importance of the nucleation scale effective action in capturing the equilibrium properties of the phase

transition. The perturbative outcomes for equilibrium properties are as follows:

$$y_{\rm c} = \frac{1-\frac{51}{2}x\log\tilde{\mu_3}}{2(8\pi)^2 x}, \tag{13.3}$$

$$\Delta\langle\phi^\dagger\phi\rangle_{\rm c} = \frac{1+\frac{51}{2}x}{2(8\pi x)^2}, \tag{13.4}$$

$$\Delta\langle(\phi^\dagger\phi)^2\rangle_{\rm c} = \frac{1+51x}{4(8\pi x)^4}, \tag{13.5}$$

$$\sigma_3 = \frac{1+\left(\frac{51\pi^2}{4}-\frac{339}{4}\right)x}{6\sqrt{2}(8\pi)^3 x^{5/2}}. \tag{13.6}$$

where $\tilde{\mu}_3 \equiv e^{-\frac{11}{34}+\frac{42}{34}\log\frac{3}{2}}(8\pi x\mu_3) \approx 1.19(8\pi x\mu_3)$. The expressions provided are precise up to $O(x^{3/2})$ in the numerators, reflecting a rigorous expansion in the parameter x to maintain gauge invariance order by order [79, 80]. The μ_3 dependence of $y_{\rm c}$ guarantees the renormalization group invariance of $y_{\rm c}-y$ at this particular order, as indicated in Eq. (13.1). This careful treatment ensures the consistency and validity of the calculations.

13.3. Lattice Volumes

The **Table 13.1** provides a compilation of lattice volumes used in the calculation of equilibrium thermodynamics, while the reference [75] contains the corresponding outcomes for each lattice.

Both cubic volumes and long asymmetrical cylindrical volumes have been employed in the simulations. While equilibrium quantities can be determined accurately using cubic lattices, the autocorrelation times increase significantly on larger lattices due to the barriers hindering the transition between phases. To address this issue, simulations on cylindrical lattices were conducted, where the order parameter was constrained to reside between the two phases. This approach enables the determination of the critical mass, y_c, in large volumes while maintaining short autocorrelation times.

x	ag_3^2	volumes$/a^3$
0.0152473	0.5455087*	16^3, 24^3, 32^3, $16^2 \times 80$
		$24^2 \times 120$, $32^2 \times 160$
	0.3636364*	24^3, 32^3, 48^3, $24^2 \times 120$
		$32^2 \times 160$, $48^2 \times 240$
	0.2727273*	32^3, 48^3, 64^3, $32^2 \times 160$
		$48^2 \times 240$, $64^2 \times 320$
	0.2181818*	40^3, 60^3, 80^3, $40^2 \times 300$
		$60^2 \times 400$, $80^2 \times 600$
0.025	0.5714286	18^3, 24^3, 30^3
	0.4444444	24^3, 30^3, 36^3
	0.4444444*	24^3, 30^3, 36^3
	0.4285714*	$20^2 \times 100$, $20^2 \times 140$
		$24^2 \times 120$, $24^2 \times 144$
		$36^2 \times 360$
	0.3333333	30^3, 40^3, 50^3
	0.3333333*	30^3, 40^3, 50^3
	0.2857143*	$30^2 \times 180$, $48^2 \times 288$
		$56^2 \times 336$, $60^2 \times 360$
	0.25	40^3, 54^3, 68^3
	0.25*	40^3, 54^3, 68^3
	0.2222222*	48^3, 60^3, 80^3
	0.2142857*	$40^2 \times 240$, $50^2 \times 300$
		$60^2 \times 360$, $80^2 \times 480$
0.036	0.5714286	18^3, 24^3, 30^3
	0.4444444	24^3, 30^3, 36^3
	0.3333333	30^3, 40^3, 50^3
	0.25	40^3, 54^3, 68^3
0.05	0.5714286	18^3, 24^3, 30^3
	0.5*	18^3, 24^3, 30^3, 36^3, 42^3
	0.4444444	24^3, 30^3, 36^3
	0.3333333	30^3, 40^3, 50^3
	0.3333333*	30^3, 36^3, 48^3, 54^3, 60^3
	0.25	40^3, 54^3, 68^3
	0.25*	32^3, 40^3, 48^3, 64^3, 72^3
0.075	0.4444444	24^3, 30^3, 36^3
	0.4285714*	20^3, 30^3, 40^3, $20^2 \times 120$
		$30^2 \times 180$, $40^2 \times 240$
	0.3333333	30^3, 40^3, 50^3
	0.2857143*	30^3, 48^3, 60^3, $30^2 \times 180$
		$40^2 \times 240$, $50^2 \times 300$
	0.25	40^3, 54^3, 68^3
	0.2142857*	40^3, 60^3, 80^3, $40^2 \times 240$
		$50^2 \times 300$, $60^2 \times 360$
	0.2	50^3, 68^3, 84^3

Table 13.1 Equilibrium Thermodynamics and * for $O(a)$